THEORETICAL STUDIES OF STRUCTURES AND MECHANISMS IN ORGANOMETALLIC AND BIOINORGANIC CHEMISTRY: HECK REACTION WITH PALLADIUM PHOSPHINES, ACTIVE SITES OF SUPEROXIDE REDUCTASE AND CYTOCHROME P450 MONOOXYGENASE, AND TETRAIRON HEXATHIOLATE HYDROGENASE MODEL

A Dissertation

by

PANIDA SURAWATANAWONG

Submitted to the Office of Graduate Studies of
Texas A&M University
in partial fulfillment of the requirements for the degree of

DOCTOR OF PHILOSOPHY

May 2009

Major Subject: Chemistry

THEORETICAL STUDIES OF STRUCTURES AND MECHANISMS IN ORGANOMETALLIC AND BIOINORGANIC CHEMISTRY: HECK REACTION WITH PALLADIUM PHOSPHINES, ACTIVE SITES OF SUPEROXIDE REDUCTASE AND CYTOCHROME P450 MONOOXYGENASE, AND TETRAIRON HEXATHIOLATE HYDROGENASE MODEL

A Dissertation

by

PANIDA SURAWATANAWONG

Submitted to the Office of Graduate Studies of
Texas A&M University
in partial fulfillment of the requirements for the degree of

DOCTOR OF PHILOSOPHY

Approved by:

Chair of Committee,	Michael B. Hall
Committee Members,	Robert R. Lucchese
	Yi-Qin Gao
	Perla Balbuena
Head of Department,	David H. Russell

May 2009

Major Subject: Chemistry

ABSTRACT

Theoretical Studies of Structures and Mechanisms in Organometallic and
Bioinorganic Chemistry: Heck Reaction with Palladium Phosphines,
Active Sites of Superoxide Reductase and Cytochrome P450 Monooxygenase,
and Tetrairon Hexathiolate Hydrogenase Model. (May 2009)
Panida Surawatanawong, B.S., Mahidol University
Chair of Advisory Committee: Dr. Michael B. Hall

The electronic structures and reaction mechanisms of transition-metal complexes can be calculated accurately by density functional theory (DFT) in cooperation with the continuum solvation model. The palladium catalyzed Heck reaction, iron-model complexes for cytochrome P450 and superoxide reductase (SOR), and tetrairon hexathiolate hydrogenase model were investigated.

The DFT calculations on the catalytic Heck reaction (between phenyl-bromide and ethylene to form the styrene product), catalyzed by palladium diphosphine indicate a four-step mechanism: oxidative addition of C_6H_5Br, migratory insertion of C_6H_5 to C_2H_4, β-hydride transfer/olefin elimination of styrene product, and catalyst regeneration by removal of HBr. For the oxidative addition, the rate-determining step, the reaction through monophosphinopalladium complex is more favorable than that through either the diphosphinopalladium or ethylene-bound monophosphinopalladium. In further study, for a steric phosphine, P^tBu_3, the oxidative-addition barrier is lower on

monopalladium monophosphine than dipalladium diphosphine whereas for a small phosphine, PMe_3, the oxidative addition proceeds more easily via dipalladium diphosphine. Of the phosphine-free palladium complexes examined: free-Pd, $PdBr^-$, and $Pd(\eta^2\text{-}C_2H_4)$, the olefin-coordinated intermediate has the lowest barrier for the oxidative-addition.

P450 and SOR have the same first-coordination-sphere, $Fe[N_4S]$, at their active sites but proceed through different reaction paths. The different ground spin states of the intermediate $Fe^{III}(OOH)(SCH_3)(L)$ model {L = porphyrin for P450 and four imidazoles for SOR} produce geometric and electronic structures that assist i) the protonation on distal oxygen for P450, which leads to O-O bond cleavage and formation of $(Fe^{IV}=O)(SCH_3)(L) + H_2O$, and ii) the protonation on proximal oxygen for SOR, which leads to $(Fe^{III}\text{-}HOOH)(SCH_3)(L)$ formation before the Fe-O bond cleavage and H_2O_2 production. The hydrogen bonding from explicit waters also stabilizes $Fe^{III}\text{-}HOOH$ over $Fe^{IV}=O + H_2O$ products in SOR.

The electrochemical hydrogen production by $Fe_4[MeC(CH_2S)_3]_2(CO)_8$ (**1**) with 2,6-dimethylpyridinium ($LutH^+$) were studied by the DFT calculations of proton-transfer free energies relative to $LutH^+$ and reduction potentials (vs. Fc/Fc^+) of possible intermediates. In hydrogen production by **1**, the second, more highly reductive, applied potential (-1.58 V) has the advantage over the first applied potential (-1.22 V) in that the more highly reduced intermediates can more easily add protons to produce H_2.

DEDICATION

To my parents, Jirasak and Chomchuen.

ACKNOWLEDGEMENTS

I would like to thank Dr. Michael B. Hall, my advisor, for the opportunities to learn and to do research under his guidance and support throughout my graduate study. I also would like to thank all my committee members, Dr. Robert Lucchese, Dr. Yi-Qin Gao, Dr. Perla Balbuena, and Dr. Bart Childs for their advice. Thanks also to all of the members in Dr. Hall's research group: Yubo Fan, Ben Vastine, Hong Wu, Xinzheng Yang, Chad Beddie, Charles Edwin Webster, Jesse Tye, Christine Thomas, and Lisa Perez for their advice and discussion. Special thanks go to Yubo Fan for all his help from the very beginning of my graduate research, Ben Vastine for his help in my research writing and presentation during the time of my study, and Lisa Perez for her help in the use of computer software. Thanks also go to Aleksander Wojcik for his support and discussion. I also would like to acknowledge DPST scholarship from Thailand, which provides part of the funding for my study through undergraduate and graduate schools.

TABLE OF CONTENTS

LIST OF FIGURES

LIST OF TABLES

CHAPTER I

INTRODUCTION

Organometallic compounds, as the name implied, contain organic ligands and metal center(s).[1,2] The metal center, especially a transition metal with d orbitals, can form bonds with carbon in various ways, not only simple σ- and π-bonds as in organic compounds, but also σ- and π-dative bonds. The metal center can also support ligand association/dissociation, electron transfer, reaction among ligands, and molecular rearrangement of ligands. Therefore, organometallic compounds become increasingly important for catalytic reactions in organic synthesis. Among these, palladium complexes are some of the most powerful catalysts to form a carbon-carbon bond because it can offer a short and selective synthetic route.[3] The palladium catalysts have numerous applications in the synthesis of building blocks for agrochemical and pharmaceutical products.[4] Here, the palladium catalyzed Heck reaction is chosen to study in this dissertation.

In biological processes, bioinorganic compounds, particularly enzymes, are found to perform catalytic reactions with a good selectivity and productivity, inspiring the synthesis of biomimic catalysts with the goal to reproduce the activity of these enzymes.[5,6] Iron is the fourth most abundant element in the Earth's crust,[7] and its

---

This dissertation follows the style of *Journal of the American Chemical Society*.

principle oxidation states, Fe(II) and Fe(III), can easily undergo acid-base and electron transfer reactions at physicological conditions. In biological systems, an iron center can cover a wide range of redox potentials, which derives from the influence of the geometry of iron coordination and ligands. Therefore, a variety of iron-containing proteins are found in living organisms and have numerous important functions, such as oxygen carriers, oxygen activators, and electron transfer proteins.[6,7] The iron-containing proteins can be classified based on the coordination chemistry of the iron as non-heme iron, heme iron, and iron-sulfur proteins. The study in this dissertation focuses on the models of the enzymes selected from these three classes of iron proteins: superoxide reductase (non-heme iron enzyme), cytochrome P450 monooxygenase (heme iron enzyme), and hydrogenase (iron-sulfur enzyme).

The studies of the reaction mechanisms for organometallic and bioinorganic compounds play an important role in the design of ligand structures and metal coordination to improve the performance of the catalysts. Since these catalytic compounds contain organic ligands and transition metals, a large number of electrons are involved in the calculation, especially in system with several metal centers. Due to the computational improvements and the developed techniques in quantum mechanical calculations, i.e., density functional theory, effective core potentials, and continuum solvation model, computational chemistry can assist in determining the mechanisms of catalytic reactions of organometallic and bioinorganic compounds.[8] The theories related to the computation of transition metal complexes are developed in Chapter II.

The research in this dissertation is composed of two main parts. The first part is the study of the reaction mechanisms for palladium catalyzed Heck cross-coupling reaction. The complete reaction mechanism of the Heck reaction using palladium phosphines is developed in Chapter III and the alternative mechanisms for the Heck reaction through dipalladium and “ligand-free” palladium intermediates are developed in Chapter IV. The second part is the study of iron enzyme models. The factors affecting the products formed by cytochrome P450 and superoxide reductase (SOR) are investigated in Chapter V while the study of the hydrogen production by $Fe_4[MeC(CH_2S)_3]_2(CO)_8$ a model for hydrogenase activity is developed in Chapter VI.

1.1 Palladium catalyzed Heck reaction

Palladium catalysis is of major importance for organic synthesis because of its wide use in cross-coupling reactions to form new chemical bonds.[3,9] One of the early examples of a cross-coupling reaction is the Heck reaction,[10,11] in which C-C bond formation occurs between an aryl halide and an olefin by a palladium catalyst in the presence of base (Scheme 1.1).

Scheme 1.1 Heck Reaction.

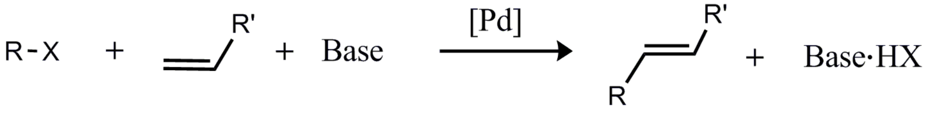

The catalytic cycle involves oxidative addition of aryl halide to the palladium complex, then olefin binding to the palladium center, migratory insertion of the aryl group to the olefin to form a new C-C bond, β-hydride transfer/olefin elimination to release the product, and proton abstraction by the base from palladium to recover the catalyst.[12,13]

The early catalytic systems for the Heck coupling used triphenylphosphine as the ligand.[10] These systems required high temperatures that produced significant ligand decomposition with P-C bond cleavage being observed.[14,15] Another problem is that the catalysts have less activity with aryl chloride.[12,13] The stronger C-Cl bond in comparison to C-I and C-Br bonds, makes the oxidative addition step, which is the rate limiting step in these systems, more difficult. The fact that aryl chlorides tend to be cheaper and more widely available generated much interest in synthesizing alternative palladium catalysts by using different bases and reaction conditions to improve the yield for aryl chlorides at moderate temperatures.[16-20] Although the N, C, and S donor ligands have been examined recently as potential ligands for the Heck reaction, the P donor ligands are still the most widely use. A better understanding in the reaction mechanism of palladium catalysts with phosphine ligand can guide the design of catalysts with a better performance.

In the first study in Chapter III, the reaction mechanism for the complete catalytic cycle of the Heck reaction catalyzed by diphosphinopalladium complexes, $Pd(PR_3)_2$ {R = H, Me, Ph}, was examined, in which phenyl bromide and ethylene in the presence of NEt_3 base are used to form the styrene product. The pathways in the oxidative addition of phenyl bromide to palladium complexes with diphosphine, monophosphine and/or olefin as alternative ligands are investigated. In the migratory insertion, β-hydride transfer/olefin elimination, and catalyst recovery, two possible pathways were explored: (1) the neutral path with bromide bound to Pd and (2) the cationic path with prior bromide ion dissociation.

The fact that some dipalladium intermediates can be isolated[21,22] and a "ligand-free" palladium system has proved recently to function well for the Heck reaction[23-29] leads to the second study. In comparison to monopalladium monophosphine, $Pd(PR_3)$ {R = Me and ^{t}Bu}, the alternative pathways for the Heck reaction via dipalladium diphosphine, $Pd_2(PR_3)_2$, and "substrate-bound" palladium intermediates: free Pd, $PdBr^-$, and $Pd(\eta^2\text{-}C_2H_4)$, are presented in Chapter IV.

1.2 Iron enzyme models

In many anaerobic organisms, superoxide reductase (SOR) is a non-heme iron enzyme functioning as superoxide scavenger.[30,31] The iron active site of SOR consists of four equatorial histidines, one axial cysteine, and the sixth coordinate occupied by glutamate in the resting state but opened for the substrate binding in the active state.[32] The iron active site of SOR binds superoxide, catalyzes one-electron reduction and releases hydrogen peroxide (i.e. $O_2^- + 2H^+ + e^- \rightarrow H_2O_2$).[33]

Cytochrome P450 monooxygenase is a heme iron enzyme for biosynthesis of steroids, detoxification of xenobiotics, and metabolism of drugs.[34] The iron active site of P450 has a porphyrin at the equatorial, a cysteine at the axial, and the sixth coordinate opened for substrate binding.[35] The iron active site of P450 binds O_2, catalyzes two-electron reduction and double protonation of O_2 to cleave the O-O bond yielding a high valent iron-oxo complex and one equivalent of H_2O (Fe^{IV}=O + H_2O); this iron-oxo complex catalyzes the stereospecific alkane hydroxylation reaction.[36,37]

Interestingly, cytochrome P450 and superoxide reductase have the same first atom coordination shell, $Fe[N_4S]$, at their active sites and have a similar hydroperoxo state, Fe^{III}-OOH, in their cycle but ultimately lead to different outcome for the oxygen atoms. The purpose of the third study in Chapter V is to examine the factors leading to the different reaction pathways between these two somewhat similar iron active site enzymes. The structural parameters and electronic structures of low, intermediate, and high spin states for the ferric hydroperoxo model complex, the common intermediates from both enzyme models, and ferric hydrogen peroxide and oxo-ferryl model complexes, their products, are studied. The effect of the active site locations in the enzymes is also investigated by including explicit water molecules to replicate the solvent-exposed position of the active site in SOR.

Finally, the fourth study is on a tetra-iron complex as a functional model of di-iron hydrogenase enzyme. Di-iron hydrogenases generally catalyze proton reduction to produce molecular hydrogen.[38-40] The enzymes active site, named as the H-cluster, consists of a di-iron [2Fe] cluster bridged to a [4Fe-4S] cluster by cysteine ligands from the protein backbone (Scheme 1.2a).[41,42] The design of biomimic catalyst to simulate the function of hydrogenase and to study the hydrogen production mechanism is especially relevant[43-49] because stable hydrogenase-like systems could be an alternative catalyst for the hydrogen production apart from the rare and expensive platinum electrode.

Scheme 1.2 Structures of (a) di-iron hydrogenase active site, (b) $[Fe(CO)_3]_2(S(CH_2)_3S)$, and (c) $Fe_4(MeC(CH_2S)_3)_2(CO)_8$.

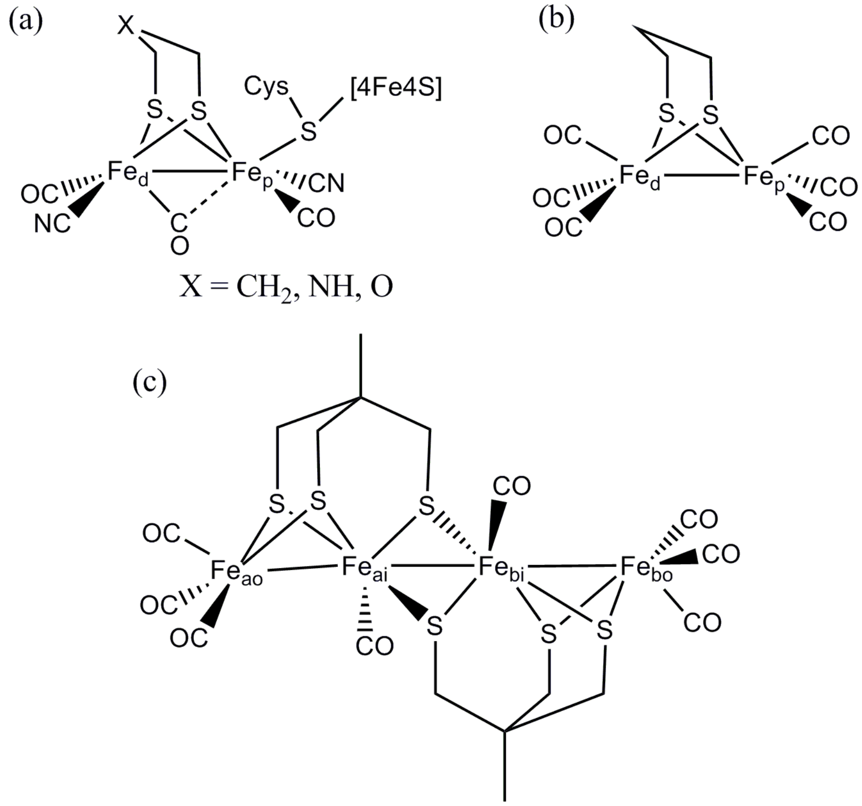

The $Fe_4[MeC(CH_2S)_3]_2(CO)_8$ (Scheme 1.2c),[50] a recent synthetic model functioning like a hydrogenase, produces hydrogen at a significantly faster rate than $[Fe(CO)_3]_2(S(CH_2)_3S)$ (Scheme 1.2b), the classical model for di-iron hydrogenase.[51] Chapter VI describes the plausible pathways for the hydrogen production on $Fe_4[MeC(CH_2S)_3]_2(CO)_8$ from the calculation of reduction potentials and proton addition free energies of possible intermediates in comparison to the applied reduction potentials and the acidity of 2,6-dimethylpyridinium ($LutH^+$), the acid used in the experiments.

CHAPTER II

THEORETICAL METHODS

The chemical reactions are directly related to electronic motion, which cannot be described correctly by classical mechanics. Therefore, quantum mechanics is necessary for the calculation of electronic structures that involves bond forming and bond breaking processes. In quantum mechanics, the physical observables can be calculated by the application of appropriate operators to the molecular wave function. The molecular wave function is obtained by solving Schrödinger equation (eq 2.1), which its time independent form is usually sufficient for chemical reactions.[52]

$$\mathbf{H_{tot}}\Psi = E_{tot}\Psi \tag{2.1}$$

The Hamiltonian operator, $\mathbf{H_{tot}}$, is the summation of the operators for the kinetic, $\mathbf{T}$, and potential, $\mathbf{V}$, energies of electrons and nuclei.

$$\mathbf{H_{tot} = T_n + T_e + V_{ne} + V_{ee} + V_{nn}} \tag{2.2}$$

Based on the Born-Oppenheimer approximation, which is an approximate separation of the motion of the heavier (slow) nuclei and lighter (fast) electrons, one can consider the electrons in a molecule moving in the field of fixed nuclei. Therefore, the electronic Hamiltonian, $\mathbf{H_{elec}}$, can be separated from $\mathbf{H_{tot}}$.

$$\mathbf{H_{elec} = T_e + V_{ne} + V_{ee}} \tag{2.3}$$

$$\mathbf{H_{elec}}\Phi_{elec} = E_{elec}\Phi_{elec} \tag{2.4}$$

Solution to the electronic Schrödinger equation in eq 2.4 is the electronic wave function, Φ_{elec}, which depends on the electronic coordinates, r_i, and parametrically on the nuclear position, such that a different Φ_{elec} function is solved for each different arrangements of nuclei (R_A). The summation of E_{elec} and V_{nn} is the potential for nuclear motion.

$$\mathbf{H_{nucl}} = \mathbf{T_n} + \mathbf{V_{nn}} + E_{elec}(\{R_A\}) \tag{2.5}$$

The solution to the nuclear Schrödinger equation in eq 2.6 is the nuclear wave function, Φ_{nucl}.

$$\mathbf{H_{nucl}}\Phi_{nucl} = E_{nucl}\Phi_{nucl} \tag{2.6}$$

$$\Psi = \Phi_{elec}(\{r_i\},\{R_A\})\Phi_{nucl}(\{R_A\}) \tag{2.7}$$

The total wave function, Ψ, is obtained as a product of the electronic and nuclear wave functions. Solving for the electronic wave function is the main task to obtain the electronic structures of molecules. Unless specified otherwise, the Hamiltonian, **H**, found later in the text will refer to the electronic Hamiltonian.

For a single electron, the wave function to describe its spatial distribution is a spatial orbital $\psi_i(r)$. To completely describe an electron, the orthonormal spin functions are included, which are spin up, $\alpha(\omega)$, and spin down, $\beta(\omega)$, functions. Then, a wave function for an electron is defined as spin orbital $\chi(x)$.

$$\chi(x) = \psi(r)\alpha(\omega) \text{ or } \psi(r)\beta(\omega) \tag{2.8}$$

The spin orbitals are usually assumed to form an orthonormal set.

$$\int \chi_i(x)\chi_j(x)dx = \langle \chi_i | \chi_j \rangle = \delta_{ij} \tag{2.9}$$

2.1 Hartree product wave function

Assuming that the electrons in the system are noninteracting, resulting in a Hamiltonian that is a summation of the operator **$\mathbf{h_i}$** (eq 2.10), describing kinetic energy and potential energy of an electron i in the field of the nuclei of Z_a charge.

$$\mathbf{H_{nonint}} = \sum_{i}^{N} \mathbf{h_i} \tag{2.10}$$

$$\mathbf{h}_i = -\frac{1}{2}\nabla_i^2 - \sum_a \frac{Z_a}{|R_a - r_i|} \tag{2.11}$$

The set of eigenfuntions for the operator **$\mathbf{h_i}$** is the set of spin orbitals.

$$\mathbf{h_i}\chi_i(x) = \varepsilon_i\chi_i(x) \tag{2.12}$$

Then, the eigenfunction for the noninteracting electron Hamiltonian is the Hartree product wave function, Φ^{HP}, which is a product of spin orbitals, and the eigenvalue is the summation of the spin orbital energies.

$$\mathbf{H_{nonint}}\Phi^{HP} = E_{nonint}\Phi^{HP} \tag{2.13}$$

$$\Phi^{HP}(x_1, x_2, \ldots, x_N) = \chi_i(x_1)\chi_j(x_2)\ldots\chi_k(x_N) \tag{2.14}$$

$$E_{nonint} = \varepsilon_i + \varepsilon_j + \ldots + \varepsilon_k \tag{2.15}$$

2.2 Antisymmetric wave function

According to the Pauli principle, the many-electron wave function also must be antisymmetric with respect to the interchange of any two electron coordinates. The Hartree product of spin orbitals does not satisfy this antisymmetric principle. On the other hand a many-electron wave function with antisymmetric properties can be obtained by forming a *Slater determinant* from the spin orbitals.

$$\Phi(\mathrm{x}_1, \mathrm{x}_2, \ldots, \mathrm{x}_\mathrm{N}) = (\mathrm{N}!)^{-1/2} \begin{vmatrix} \chi_i(\mathrm{x}_1) & \chi_j(\mathrm{x}_1) & \cdots & \chi_k(\mathrm{x}_1) \\ \chi_i(\mathrm{x}_2) & \chi_j(\mathrm{x}_2) & \cdots & \chi_k(\mathrm{x}_2) \\ \vdots & \vdots & \ddots & \vdots \\ \chi_i(\mathrm{x}_N) & \chi_j(\mathrm{x}_N) & \cdots & \chi_k(\mathrm{x}_N) \end{vmatrix} \tag{2.16}$$

The rows of Slater determinant are labeled by electrons and the columns are labeled by spin orbitals, whereas the factor $(\mathrm{N}!)^{-1/2}$ is a normalization factor. The short-hand notation for a normalized Slater determinant is shown in eq 2.17.

$$\Phi(\mathrm{x}_1, \mathrm{x}_2, \ \ldots\ , \mathrm{x}_\mathrm{N}) \ = \ |\chi_\mathrm{i}(\mathrm{x}_1)\chi_\mathrm{j}(\mathrm{x}_2)\ldots\chi_\mathrm{k}(\mathrm{x}_\mathrm{N})\rangle \tag{2.17}$$

Interchanging the coordinates of two electrons corresponds to interchanging the two rows of the Slater determinant, which changes the sign of the determinant (eq 2.18). Having two electrons occupying the same spin orbital corresponds to having two columns of the determinant equal, which makes the determinant zero.

$$|\ldots.\chi_\mathrm{m}\ \cdots\ \chi_\mathrm{n}\ \ldots\rangle = -|\ldots.\chi_\mathrm{n}\ \cdots\ \chi_\mathrm{m}\ \ldots\rangle \tag{2.18}$$

To evaluate the energy of a single Slater determinant, the Slater determinant is rewritten as a sum of permutations over the diagonal of the determinant (eq 2.19), in which the diagonal product is denoted as Π and the **A** operator is the antisymmetrizing operator as shown in eq 2.20.[53]

$$\Phi = \mathbf{A}[\chi_1(\mathrm{x}_1)\chi_2(\mathrm{x}_1)\ldots\chi_\mathrm{N}(\mathrm{x}_\mathrm{N})] = \mathbf{A}\Pi \tag{2.19}$$

$$\mathbf{A} = (N!)^{-1/2}\sum_{p=0}^{N-1}(-1)^p\mathbf{P} = (\mathrm{N}!)^{-1/2}[\mathbf{1} - \sum_{ij}\mathbf{P}_{ij} + \sum_{ijk}\mathbf{P}_{ijk} - \ldots] \tag{2.20}$$

The **1** is an identity operator; **P** is a permutator operator, in which $\mathbf{P_{ij}}$ generates all possible permutations of two-electron coordinates, $\mathbf{P_{ijk}}$ generates all possible permutations of three-electron coordinates, and so on. The **A** operator was proved to commute with Hamiltonian operator and **A** operating twice gives the same as **A** operating once, multiplying by the $(N!)^{1/2}$.

$$\mathbf{AH} = \mathbf{HA} \tag{2.21}$$

$$\mathbf{AA} = (N!)^{1/2}\mathbf{A} \tag{2.22}$$

The Hamiltonian operator is composed of one-electron operator, $\mathbf{h_i}$, (eq 2.11) and two-electron operator, $\mathbf{g_{ij}}$**,** describing the electron-electron repulsion.

$$\mathbf{g}_{\mathrm{ij}} = \frac{1}{\left|r_i - r_j\right|} \tag{2.23}$$

$$\mathbf{H} = \sum_{i=1}^{N}\mathbf{h}_{\mathrm{i}} + \sum_{i=1}^{N}\sum_{j>i}^{N}\mathbf{g}_{\mathrm{ij}} \tag{2.24}$$

From eq 2.19, the energy can be written by including permutation operator.

$$\mathrm{E} = \left\langle \Phi \middle| \mathbf{H} \middle| \Phi \right\rangle = \left\langle \mathbf{A}\Pi \middle| \mathbf{H} \middle| \mathbf{A}\Pi \right\rangle = \sum_{p} (-1)^{p} \left\langle \Pi \middle| \mathbf{H} \middle| \mathbf{P}\Pi \right\rangle \tag{2.25}$$

Since all the spin orbitals are orthonormal, only the identity operator can give a non-zero contribution for the one-electron operator (eq 2.26) and only the identity and the $\mathbf{P}_{\mathrm{ij}}$ operators can give a non-zero contribution for the two-electron operator. Then the Coulomb ($\mathbf{J}_{\mathrm{i}}$) and Exchange ($\mathbf{K}_{\mathrm{i}}$) operators are introduced (eq 2.27 and 2.28).

$$\left\langle \Pi \middle| \mathbf{h}_1 \middle| \Pi \right\rangle = \left\langle \chi_1(1) \middle| \mathbf{h}_1 \middle| \chi_1(1) \right\rangle \tag{2.26}$$

$$\left\langle \Pi \middle| \mathbf{g}_{12} \middle| \Pi \right\rangle = \left\langle \chi_1(1)\chi_2(2) \middle| \mathbf{g}_{12} \middle| \chi_1(1)\chi_2(2) \right\rangle = \left\langle \chi_2(2) \middle| \mathbf{J}_1 \middle| \chi_2(2) \right\rangle \tag{2.27}$$

$$\langle \Pi | \mathbf{g}_{12} | \mathbf{P}_{12}\Pi \rangle = \langle \chi_1(1)\chi_2(2) | \mathbf{g}_{12} | \chi_2(1)\chi_1(2) \rangle = \langle \chi_2(2) | \mathbf{K}_1 | \chi_2(2) \rangle \quad (2.28)$$

Now the energy can be expressed in terms of Coulomb and Exchange operators as in eq 2.29. A Coulomb term is derived from an electron repulsion between two charge distributions, $|\chi_1(1)|^2$ and $|\chi_2(2)|^2$, whereas an Exchange term arises from the antisymmetric properties of the wave function.

$$\mathrm{E} = \sum_i^N \langle \chi_i | \mathbf{h}_i | \chi_i \rangle + \frac{1}{2}\sum_{ij}^N (\langle \chi_j | \mathbf{J}_i | \chi_j \rangle - \langle \chi_j | \mathbf{K}_i | \chi_j \rangle) \quad (2.29)$$

$$\mathbf{J}_i | \chi_j(2) \rangle = \langle \chi_i(1) | \mathbf{g}_{12} | \chi_i(1) \rangle | \chi_j(2) \rangle \quad (2.30)$$

$$\mathbf{K}_i | \chi_j(2) \rangle = \langle \chi_i(1) | \mathbf{g}_{12} | \chi_j(1) \rangle | \chi_i(2) \rangle \quad (2.31)$$

Antisymmetrizing a Hartree product wave function to obtain a Slater determinant introduces the electron correlation from the Exchange term (this is usually called "Fermi correlation"), in which the motion of two electrons with parallel spins is correlated but the motion of two electrons with opposite spins is still uncorrelated.

2.3 Hartree-Fock approximation

Hartree-Fock (HF) approximation is an approach to solve an electronic Schrödinger equation for many-electron problems for the case of a single determinant. From the variational principle, an approximate wave function has an energy which is above or equal to the exact energy.

$$\mathrm{E}_{\mathrm{exact}} \le \langle \Phi | \mathbf{H} | \Phi \rangle \quad (2.32)$$

By minimizing E with respect to the choice of spin orbitals, one can determine the set of spin orbitals. Derived from the variation of the energy in eq 2.29, the Fock operator, $\mathbf{f}_i$ is obtained as an effective one-electron operator (eq 2.33) and the Hartree-Fock equation can be written as eq 2.34.

$$\mathbf{f}_i = \mathbf{h}_i + \sum_j^N (\mathbf{J}_j - \mathbf{K}_j) \tag{2.33}$$

$$\mathbf{f}_i \chi_i = \varepsilon_i \chi_i \tag{2.34}$$

The Hartree-Fock approximation replaces a many-electron problem by a one-electron problem with average electron-electron repulsion. Since the second term in eq 2.33 depends on the spin orbital χ_j, solving the Hartree-Fock equation must be an iterative procedure, which is called the self-consistent-field (SCF) method. Note that the Fock operator is derived from the variation of the energy and the total electronic energy is not a sum of these Fock orbital energies, ε_i, but instead, it is written as eq 2.35.

$$\mathrm{E} = \sum_i^N \varepsilon_i - \frac{1}{2}\sum_{ij}^N (J_{ij} - K_{ij})\,; \tag{2.35}$$

$$\varepsilon_i = \langle \chi_i | \mathbf{f}_i | \chi_i \rangle; \quad J_{ij} = \langle \chi_j | \mathbf{J}_i | \chi_j \rangle; \quad K_{ij} = \langle \chi_j | \mathbf{K}_i | \chi_j \rangle$$

2.4 Basis set approximation

To solve for the spin orbital in the HF equation, the spin orbital can be expanded in terms of a known finite set of spatial basis functions (φ_α).

$$\chi_i = \sum_{\alpha}^{M} c_{\alpha i} \varphi_\alpha \tag{2.36}$$

$$\mathbf{f}_i \sum_{\alpha}^{M} c_{\alpha i} \varphi_\alpha = \varepsilon_i \sum_{\alpha}^{M} c_{\alpha i} \varphi_\alpha \tag{2.37}$$

By substituting a set of spatial basis functions $\{\varphi_\alpha\}$ into the HF equation, multiplying from the left by a basis function and integrating, a matrix equation is obtained, called *Roothaan-Hall* equation (eq 2.38).

$$\mathbf{FC} = \mathbf{SC}\varepsilon \tag{2.38}$$

$$\mathrm{F}_{\alpha\beta} = \left\langle \varphi_\alpha \middle| \mathbf{f}_i \middle| \varphi_\beta \right\rangle \tag{2.39}$$

$$\mathrm{S}_{\alpha\beta} = \left\langle \varphi_\alpha \middle| \varphi_\beta \right\rangle \tag{2.40}$$

The Fock matrix, **F** with $F_{\alpha\beta}$ elements, is the matrix representation of the Fock operator with the set of basis function $\{\varphi_\alpha\}$. The overlap matrix, **S** with $S_{\alpha\beta}$ elements, arises from the fact that the basis functions are not orthogonal to each other although assumed to be normalized and linearly independent. **C** is a square matrix of the expansion coefficients $c_{\alpha i}$.

If the basis functions are orthonormal, the **S** matrix will become the unit matrix and Roothaan-Hall equation will become a simple matrix eigenvalue equation. By diagonalizing **F**, one could find the eigenvectors **C** and eigenvalues ε. For non-orthomormal basis functions, a simple transformation will produce an equivalent result. Solving the matrix equation (eq 2.38) yields a set of orthonormal Hartree-Fock spin orbitals $\{\chi_i\}$ (when $c_{\alpha i}$ is known) with orbital energies $\{\varepsilon_i\}$. The N spin orbitals with lowest energies for N electrons are the occupied spin orbitals. The Hartree-Fock ground state wave function is the Slater determinant formed from these occupied spin orbitals.

The electronic energy of the HF wave function in eq 2.29 can be rewritten in term of integral over basis functions and density matrix elements, $D_{\alpha\beta}$.

$$\begin{aligned}\mathrm{E} = \sum_{i}^{N}\sum_{\alpha\beta}^{M} \mathrm{c}_{\alpha i}\mathrm{c}_{\beta i}\left\langle \varphi_\alpha \middle| \mathbf{h}_i \middle| \varphi_\beta \right\rangle + \frac{1}{2}\sum_{ij}^{N}\sum_{\alpha\beta\gamma\delta}^{M} \mathrm{c}_{\alpha i}\mathrm{c}_{\gamma j}\mathrm{c}_{\beta i}\mathrm{c}_{\delta j}(\left\langle \varphi_\alpha\varphi_\gamma \middle| \mathbf{g}_{ij} \middle| \varphi_\beta\varphi_\delta \right\rangle \\ -\left\langle \varphi_\alpha\varphi_\gamma \middle| \mathbf{g}_{ij} \middle| \varphi_\delta\varphi_\beta \right\rangle)\end{aligned} \tag{2.41}$$

$$\mathrm{E} = \sum_{\alpha\beta}^{M} \mathrm{D}_{\alpha\beta}\left\langle \varphi_\alpha \middle| \mathbf{h}_i \middle| \varphi_\beta \right\rangle + \frac{1}{2}\sum_{\alpha\beta\gamma\delta}^{M} \mathrm{D}_{\alpha\beta}\mathrm{D}_{\gamma\delta}(\left\langle \varphi_\alpha\varphi_\gamma \middle| \mathbf{g}_{ij} \middle| \varphi_\beta\varphi_\delta \right\rangle - \left\langle \varphi_\alpha\varphi_\gamma \middle| \mathbf{g}_{ij} \middle| \varphi_\delta\varphi_\beta \right\rangle) \tag{2.42}$$

$$\mathrm{D}_{\alpha\beta} = \sum_{i}^{N} \mathrm{c}_{\alpha i}\mathrm{c}_{\beta i} \tag{2.43}$$

Larger basis sets will lower the electronic energy eventually to reach Hartree-Fock limit. Adding the nuclear-nuclear repulsion energy, V_{nn}, to the electronic energy yields the total energy as a function of a set of nuclear coordinates. The potential energy surface for the nuclear motion can be constructed from the calculation of the total energy at different set of nuclear coordinates.

2.5 Mulliken population analysis

In the population analysis that is based on basis functions, the electron density $\rho_i(r)$ from a single spin orbital containing one electron is given by eq 2.44.

$$\rho_i(r) = \chi_i^2(r) = \sum_{\alpha\beta}^{M} \mathrm{c}_{\alpha i} c_{\beta i}\varphi_\alpha\varphi_\beta \tag{2.44}$$

The total number of electrons, N, can be derived from integrating the electron density and summing over all occupied orbitals, which is rewritten as a sum over the product of the density and the overlap matrix elements.

$$N = \sum_{i}^{N} \int \chi_i^2(r)dr = \sum_{i}^{N} \sum_{\alpha\beta}^{M} \mathrm{c}_{\alpha i} c_{\beta i} \int \varphi_\alpha \varphi_\beta dr = \sum_{\alpha\beta}^{M} D_{\alpha\beta} S_{\alpha\beta} \tag{2.45}$$

The diagonal element $D_{\alpha\alpha}S_{\alpha\alpha}$ is the number of electrons in the atomic orbital (AO) α, and an off-diagonal element $D_{\alpha\beta}S_{\alpha\beta}$ is half the number of electrons shared by AOs α and β. The number of electrons on atom A can be determined from the summation of the contributions from all AOs located on atom A. The *Mulliken population analysis*[54] divides the contribution involving basis functions on different atoms equally between two atoms. The Mulliken electron population on atom A is defined as eq 2.46 and the gross charge on atom A is defined as eq 2.47, where Z_A is the nuclear charge of atom A.

$$\rho_A = \sum_{\alpha \in A}^{M} \sum_{\beta}^{M} \mathrm{D}_{\alpha\beta} S_{\alpha\beta} \tag{2.46}$$

$$Q_A = Z_A - \rho_A \tag{2.47}$$

2.6 Basis functions

The basis function that is suitable for the calculation of the electronic structure of molecules should represent the atomic orbital character, in which the function goes toward zero as nuclear-electron distance is large and has a large finite slope as the nuclear-electron distance approaches zero. Slater type orbital (STO)[55] in eq 2.48 and Gaussian type orbital (GTO)[56] in eq 2.49 are in commonly used.

$$\phi_{\mathrm{STO}}(r,\theta,\gamma) = NY_{l,m}(\theta,\gamma)r^{n-1}e^{-\zeta r} \tag{2.48}$$

$$\phi_{\mathrm{GTO}}(r,\theta,\gamma) = NY_{l,m}(\theta,\gamma)r^{(2n-2-l)}e^{-\zeta r^2} \tag{2.49}$$

Slater type orbital is close to the atomic orbital in that the function has a cusp at zero nuclear-electron distance. Although the simple STO does not have radial nodes, the linear combination of STOs can introduce the radial nodes. The disadvantage of STOs is that three- and four-center two-electron integrals cannot be calculated analytically.

Gaussian type orbital is mainly different from STO in that the exponential part of GTO depends on r^2. This causes a zero slope at the nucleus position and the function decreases too rapidly at far distances from the nucleus. Although a larger number of GTOs is needed to represent atomic orbital compared to STOs, GTOs are more convenient for the calculation because one can find an analytical solution for four-center two-electron integrals of GTOs.

The smallest number of functions possible is a *minimum basis set* with only enough functions for all the electrons, for example, just one s-function for hydrogen and helium and two s-functions and one set of p-functions for the first row in the periodic table. However, doubling the number of basis functions can improve the basis sets, especially the basis functions to describe valence electrons, because the chemical bond is formed by the electrons of this type. The basis set with double the number of basis functions for valence electrons is called *valence double zeta* (VDZ) basis. Larger basis sets containing three times or more of the minimum basis set are called triple zeta, quadruple zeta, and so on. In most cases the higher angular momentum functions called *polarization functions* are added to make a better description of chemical bond; for example, the p-orbital can introduce a polarization to the s-orbital for a bound hydrogen atom. Many properties depend on the wave function tail, far from the nucleus; to describe molecules with loosely bound electrons, such as anions, the basis functions with small exponents called *diffuse functions* are needed.

Although the GTO's shape has some features that do not represent the atomic orbital as well as STOs, the combination of several GTOs can replicate an approximate STO. The fixed linear combination of primitive GTOs (PGTOs) is called the *contracted GTO* (CGTO). For example, 6-31G Pople-style basis set is a split valence double zeta basis set, where each core orbital is a CGTO with six PGTOs and each valence orbital is split into two CGTOs, the inner one with three PGTOs and the outer one with one PGTO.[57] The 6-31+G(d) is also a split valence double zeta basis set like 6-31G with the additional set of diffuse sp-function and a single d-type polarization function on heavy atoms.

2.7 Effective core potential

Most chemical reactions involve the valence electron's interaction whereas the core electrons, which are more strongly bound to the nuclei, are chemically inert. Therefore, for the systems involving the atoms that contain a large number of core electrons, from the third row or higher in the periodic table, the *effective core potential* (ECP)[58] is introduced as a one-electron operator to replace two-electron Coulomb and

Exchange operators that arise from the interactions between core electrons and valence electrons in the valence-only Hartree-Fock equation.[59] Here, only the non-relativistic case is discussed, but the ECP used for heavier atoms are relativistic and produce relativistically shape valence orbitals. The Hartree-Fock equation for a valence orbital, χ_l, with angular momentum l (eq 2.50), where V_{core} and V_{val} are the Coulomb and Exchange potentials from the core electrons and other valence electrons, respectively, can be replaced by the equation that contains a pseudo orbital, $\chi_l^{'}$, and effective core potential, V_l^{eff} (eq 2.51),[60] where Z_{eff} is the effective nuclear charge shielded by the core electrons, $V_{val}^{'}$ is the potential from the valence electrons evaluated from the pseudo orbitals, and the pseudo orbital has the same orbital energy as the valence orbital ($\varepsilon_l^{'} = \varepsilon_l$).

$$\left(-\frac{1}{2}\nabla^2 - \frac{Z}{r} + \frac{l(l+1)}{2r^2} + V_{val} + V_{core}\right)\chi_l = \varepsilon_l \chi_l \qquad (2.50)$$

$$\left(-\frac{1}{2}\nabla^2 - \frac{Z_{eff}}{r} + \frac{l(l+1)}{2r^2} + V_{val}^{'} + V_l^{eff}\right)\chi_l^{'} = \varepsilon_l^{'} \chi_l^{'} \qquad (2.51)$$

The pseudo orbital in eq 2.51 is chosen to be smooth and nodeless at the core region to reduce the number of basis functions to construct the orbital while its outer part is still resemble to the valence orbitals in eq 2.50. With these properties, the pseudo orbital can be expressed in eq 2.52[61] where r_m is chosen near the outermost maximum point of $\chi_l(r)$ and coefficients c_i are determined from matching the $\chi_l^{'}(r)$ to $\chi_l(r)$ including their first three derivatives at r_m with the condition that $\chi_l^{'}(r)$ is normalized.

$$\chi_l^{'}(r) = \begin{cases} \sum_{i=0}^{4} c_i r^i & \text{for } r \le r_m \\ \chi_l(r) & \text{for } r \ge r_m \end{cases} \tag{2.52}$$

Then, for the calculation convenience, the pseudo orbital is fitted into Gaussian type orbitals (eq 2.53).[62]

$$\chi_l^{'} \sim \sum_i C_{li} r^l e^{-\alpha_{li} r^2} \tag{2.53}$$

From the pseudo orbitals, the effective core potential for each angular momentum l can be generated numerically by inverting the eq 2.51.

$$V_l^{eff} = \varepsilon_l^{'} + \frac{Z_{eff}}{r} - \frac{l(l+1)}{2r^2} + \frac{\left(\frac{1}{2}\nabla^2 - V_{val}^{'}\right)\chi_l^{'}}{\chi_l^{'}} \tag{2.54}$$

Note that the $\chi_l^{'}(r)$ has the same orbital energy as $\chi_l(r)$ and $V_{val}^{'}$ is determined by the pseudo orbitals. Normally the numerical potential for each angular momentum l is also fitted into Gaussian functions.

$$V_l^{eff} \sim \sum_k A_{lk} e^{-\zeta_{lk} r^2} \tag{2.55}$$

Finally, the total effective core potential is the summation in eq 2.56 for l = 0, 1, …, L where L is one greater than the highest l of the core orbitals.

$$V^{eff} = V_L^{eff} + \sum_{l=0}^{L} (V_l^{eff} - V_L^{eff}) |l\rangle\langle l| \tag{2.56}$$

This procedure to obtain pseudo orbitals and effective core potentials is called shape-consistent method. The alternative way is energy-adjusted method, in which the $\chi_l^{'}(r)$ has different orbital energy from the corresponding $\chi_l(r)$. The parameters A_{lk}

and ζ_{lk} in to evaluate the effective core potential in eq 2.55 are determined by minimizing the energy difference between $\varepsilon_l^{'}$ and ε_l.

Using effective core potentials and the pseudo orbitals for the valence orbitals, the interaction of valence electrons and the core electrons is taken into account with no need to calculate the core orbitals, leading to a lower cost of computation than performing all-electron calculations. The popular effective core potentials and pseudo orbitals are Hay and Wadt[62] (at Los Alamos National Laboratory - LANL) and Stuttgart–Dresden[63] (SDD) effective core potentials.

2.8 The electron correlation

In the Hartree-Fock approximation, each electron experiences an average potential from nuclei and other electrons; the probability to find electron one and electron two of different spin at any given point in space are independent. Although the electron correlation (Fermi type) for the electrons of like spin is included in HF, the electrons of opposite spin are uncorrelated. Therefore, the HF energy is always larger than the true energy due to the lack of this electron correlation. The difference between the true energy and the HF energy is the correlation energy (this type of correlation is often referred to Coulomb correlation). There are several approaches to improve the HF theory by including the electron correlation, such as configuration interaction, coupled cluster method, perturbation theory, and density functional theory. In this dissertation, density functional theory will be discussed and used in the calculation.

2.9 Density functional theory

Derived from the wave function Φ, the electron density ρ(r) is a probability density of finding any of the N electrons within the volume element *dr* while the other N-1 electrons have arbitrary positions.

$$\rho(r_1) = \int \left|\Phi(r_2, r_3, ..., r_N)\right|^2 dr_2 dr_3 ... dr_N \tag{2.57}$$

Hohenberg and Kohn[64] proved that the energy is a unique functional of the electron density. Then the ground state electronic energy can be determined from the electron density, which is the basis of Density Functional Theory (DFT).[65] The advantage of the electron density based method over wave function based method is distinguished by having fewer variables; the electron density with three spatial coordinates compares to the N-electron wave function with 3N spatial coordinates. The goal of DFT methods is to design a functional connecting the electron density with the energy E[ρ]. The energy functional could be divided into three parts, kinetic energy of electrons, T[ρ], nuclear-electron interaction, $E_{ne}[\rho]$, and electron-electron interaction, $E_{ee}[\rho]$.

$$E[\rho] = T[\rho] + E_{ne}[\rho] + E_{ee}[\rho] \tag{2.58}$$

The electron-electron interaction is composed of Coulomb, J[ρ], and Exchange, K[ρ], parts. From all terms, only $E_{ne}[\rho]$ and J[ρ] can be derived from their classical terms as eq 2.59 and eq 2.60, respectively.

$$\mathrm{E_{ne}}[\rho] = \sum_A \int \frac{Z_A \rho(r)}{|R_A - r|} dr \tag{2.59}$$

$$\mathrm{J}[\rho] = \frac{1}{2} \int\int \frac{\rho(r)\rho(r')}{|r - r'|} dr dr' \tag{2.60}$$

To obtain the kinetic energy part, Kohn and Sham[66] introduced the non-interacting reference system. Then, the Hamiltonian does not contain electron-electron interaction. Like the Hartree-Fock method, the ground state wave function corresponds to a Slater determinant constructed of the spin orbitals called Kohn-Sham orbitals (ϕ) that are the eigenfunctions of Kohn-Sham operator (f^{KS}), where $V_S(r)$ is the effective potential.

$$\mathrm{f}^{\mathrm{KS}} = -\frac{1}{2} \nabla^2 + V_S(r) \tag{2.61}$$

To connect this non-interacting system with the real system, the effective potential is chosen such that the electron density from non-interacting system, $\rho_{\mathrm{S}}(r)$, is equal to the one in real system, $\rho(r)$ ($\rho_{\mathrm{S}}(r) = \sum_i^N |\phi_i(r)|^2 = \rho(r)$). Now, the major part of the exact kinetic energy can be calculated accurately for the non-interacting electrons, $\mathrm{T_S}$.

$$\mathrm{T_S} = \sum_i^N \langle \phi_i | -\frac{1}{2} \nabla^2 | \phi_i \rangle \tag{2.62}$$

The energy functional in eq 2.58 can be rewritten with the known functionals (the first three terms in eq 2.63) and the unknown exchange-correlation term, $\mathrm{E_{xc}}[\rho]$.

$$\mathrm{E}[\rho] = \mathrm{T_S}[\rho] + \mathrm{E_{ne}}[\rho] + \mathrm{J}[\rho] + \mathrm{E_{xc}}[\rho] \tag{2.63}$$

$$\mathrm{E_{xc}}[\rho] = (\mathrm{T}[\rho] - \mathrm{T_S}[\rho]) + (\mathrm{E_{ee}}[\rho] - \mathrm{J}[\rho]) \tag{2.64}$$

The first term in eq 2.64 is the correction term for the kinetic energy, which is considered as the kinetic correlation energy whereas the second term contains exchange and potential correlation energy. The different DFT methods have different choices of the functional forms of the unknown exchange-correlation term. If the exact $E_{xc}[\rho]$ was known, DFT would provide the exact total energy, including electron correlation. The $E_{xc}[\rho]$ is often split into exchange and correlation contributions, in which the kinetic energy correlation is somewhat hidden.

$$E_{xc}[\rho] = E_x[\rho] + E_c[\rho] \tag{2.65}$$

The *local density approximation* (LDA) is derived from the model of a uniform electron gas, in which the electron density is a constant value everywhere. Here, the E_{xc} can be written in the simple form.

$$E_{xc}^{LDA}[\rho] = \int \rho(r)\varepsilon_{xc}(\rho(r))dr \tag{2.66}$$

$$\varepsilon_{xc}(\rho) = \varepsilon_x(\rho) + \varepsilon_c(\rho) \tag{2.67}$$

The Slater exchange[67] and the correlation functional by Vosko, Wilk, and Nusair (VWN)[68] are widely used for ε_x and ε_c functionals, respectively. For the unrestricted calculation, the LDA is extended to *local spin-density approximation* (LSD).

$$E_{xc}^{LSD}[\rho_\alpha, \rho_\beta] = \int \rho(r)\varepsilon_{xc}(\rho_\alpha(r), \rho_\beta(r))dr \tag{2.68}$$

For the LDA, the uniform electron gas is assumed because it is the only system that the accurate forms of the exchange and correlation energy functional are known. However, the electron density in the real chemical system is not constant everywhere; the performance of the LDA is quite poor, especially for the properties like bond energies.

To take into account of the inhomogeneity of the electron density in the real system, the gradient of the electron density can be included in the functionals which then called the *generalized gradient approximation* (GGA).

$$\mathrm{E}_{xc}^{GGA}[\rho,\nabla\rho]=\mathrm{E}_{x}^{GGA}+\mathrm{E}_{c}^{GGA} \tag{2.69}$$

A commonly used exchange functional of this type were developed by Becke 1988 (B)[69] whereas the popular correlation functionals are Perdew 1986 (P86),[70] Perdew and Wang 1991 (PW91),[71] and Lee, Yang, and Parr 1998 (LYP),[72] in which the currently used E_{xc}^{GGA} from the combination of the exchange and the correlation contributions are BLYP, BP86, and BPW91 functionals. There are also some GGA functionals that the exchange and correlation functionals are developed for use together such as Perdew, Burke, and Ernzerhof (PBE),[73] and Tao, Perdew, Staroverov, and Scuseria (TPSS),[74] which are also widely used in the electronic structure calculation.

Since the exchange energy of a Slater determinant can be obtained from Hartree-Fock calculation exactly, the combination of a certain amount of the exact exchange energy from Hartree-Fock and the exchange-correlation functional in DFT is expected to improve the functional models, leading to *hybrid functionals*. In 1993, Becke[75] introduced the combination of the exact exchange with the LSD and GGA functionals weighed by three empirical parameters (B3).

$$\mathrm{E}_{xc}^{B3}=(1-a)\mathrm{E}_{x}^{LSD}+a\mathrm{E}_{x}^{exact}+b\mathrm{E}_{x}^{B}+\mathrm{E}_{c}^{LSD}+c\mathrm{E}_{c}^{PW91} \tag{2.70}$$

Later Stephen et al. modified the B3 functional to form a B3LYP[76] functional as shown in eq 2.71, in which the three parameters are still the same as in the B3 functional. Currently, B3LYP is the most popular functional in the electronic structure calculation.

$$E_{xc}^{B3LYP} = (1-a)E_{x}^{LSD} + aE_{x}^{exact} + bE_{x}^{B} + cE_{c}^{LYP} + (1-c)E_{c}^{VWN} \tag{2.71}$$

There are also parameter-free hybrid functionals such as PBE0,[77] in which 25% of the "exact" exchange is used instead of the empirical parameter.

$$E_{xc}^{PBE0} = E_{xc}^{PBE} + 0.25(E_{xc}^{exact} + E_{xc}^{PBE}) \tag{2.72}$$

Density functional theory can explain the chemical system more accurately than Hartree-Fock theory with much less cost of calculation than other electron correlation methods. Therefore, DFT is suitable for the calculation of molecules of moderate size containing transition metal(s).

2.10 Geometry optimization

Searching for a set of nuclear coordinates, for which the total energy is a minimum on the potential energy surface, can lead to a stable structure of the molecule that could be an intermediate for the reaction of interest. Calculating all set of nuclear positions on the potential energy surface to find a minimum structure would be computationally intensive and is usually unnecessary. Minimization algorithms are normally used to locate the minimum energy structures. Most of the minimization algorithms that are used in the quantum mechanical calculation are based on the derivative of the energies with respect to the atomic coordinates because the derivatives can give information about the shape of the energy surface. The first and the second derivatives of the energy (gradient, **g**, and Hessian, **H**, respectively) provide the direction toward the minimum. Commonly used minimization algorithms:[78] steepest descent, conjugate gradient, and Newton-Raphson methods are discussed here.

For the *steepest descent* method, each step follows the negative gradient direction, $\mathbf{s_k}$ (eq 2.73). To locate the minimum point, one can perform a line search or take an arbitrary step size in the negative gradient direction.

$$\mathbf{s_k} = -\frac{\mathbf{g_k}}{|\mathbf{g_k}|} \tag{2.73}$$

In the line search, each point is calculated along the line (in the first negative gradient direction) until three points is found with the middle point has lower energy than the two outer points. Then more points in between the middle point and the two outer points need to be calculated; one may fit a function to these points to find the minimum along the line. Once the minimum along the first line is found, then another line search is performed for the next direction that is orthogonal to the first direction, in which $\mathbf{g_k} \bullet \mathbf{g_{k+1}} = 0$. On the other hand in the arbitrary step size approach, one can take the arbitrary step size, λ_k, from point k ($\mathbf{x_k}$) in the negative gradient direction (eq 2.74). Then calculate the gradient for the next point ($\mathbf{x_{k+1}}$) and repeat the process until the minimum is reached.

$$\mathbf{x_{k+1}} = \mathbf{x_k} + \lambda_k \mathbf{s_k} \tag{2.74}$$

The steepest descent is robust at points far from the minimum; however, the path oscillates and converges very slowly near the minimum.

In the *conjugate gradient* method, each step follows the direction that is conjugated to the previous direction (eq 2.75), where the γ_k can be varied, the γ_k shown here is developed by Polak-Ribiere.[79] The line search and the arbitrary step approaches are also applied to locate the minimum point.

$$\mathbf{s_k} = -\mathbf{g_k} + \gamma_k \mathbf{s_{k-1}} \tag{2.75}$$

$$\gamma_k = \frac{(\mathbf{g_k} - \mathbf{g_{k-1}}) \bullet \mathbf{g_k}}{\mathbf{g_{k-1}} \bullet \mathbf{g_{k-1}}} \tag{2.76}$$

Unlike the steepest descent, in which the direction for the next step is orthogonal to the current direction, the conjugate gradient method is expected to give the path that converges faster.

In the *Newton-Raphson* method, the energy function is approximated to the second-order in Taylor series expansion (eq 2.77).

$$f(\mathbf{x}) = f(\mathbf{x_k}) + (\mathbf{x}\text{-}\mathbf{x_k})\mathbf{g}(\mathbf{x_k}) + (\mathbf{x}\text{-}\mathbf{x_k})^2\mathbf{H}(\mathbf{x_k})/2 \tag{2.77}$$

$$f'(\mathbf{x}) = \mathbf{g}(\mathbf{x_k}) + (\mathbf{x}\text{-}\mathbf{x_k})\mathbf{H}(\mathbf{x_k}) \tag{2.78}$$

At the minimum, the first derivative of the energy, f'(**x**), is zero. If the energy function is a quadratic function, one can find a minimum point in one step using eq 2.79.

$$\mathbf{x_{k+1}} = \mathbf{x_k} - \frac{\mathbf{g_k}}{\mathbf{H_k}} \tag{2.79}$$

However, the real energy function is of higher order than second-order. Therefore, the Newton-Raphson method will take a certain number of steps, in which the inverse Hessian is required for each step. Although the path in Newton-Raphson method can converge very quickly near the minimum point, where the energy function is close to the quadratic function, the calculation of the exact Hessian and its inverse for each point is computational demanding. In practice, the Hessian at the current point is approximated by updating from the gradients and the Hessian at the previous point. The Newton-Raphson method with this approximated Hessian is called *pseudo-Newton Raphson* method, which is the most commonly used in the geometry optimization for the electronic structure calculation.

2.11 The partition function

The partition function is used for the calculation of macroscopic properties from the molecular properties as will be shown below. A molecular partition function, q, is a sum of exponential terms involving all quantum energy states as shown in eq 2.80, where E_i is an energy level, g_i is the degeneracy of each energy level, k_B is the Boltzmann's constant and T is the temperature.

$$q = \sum_i g_i e^{-E_i/k_B T} \tag{2.80}$$

The molecular partition function is associated with the internal motion of a molecule, i.e. the product of partition functions associated with electronic, vibrational, rotational, and translational motions.

$$q = q_{elec} q_{vib} q_{rot} q_{trans} \tag{2.81}$$

The electronic partition function, q_{elec}, involves the electronic energies of the ground state and excited states solving from the electronic Schrodinger equation. However, normally the energy difference between ground state and excited states is much larger than $k_B T$ at the room temperature. When the ground state energy is set to zero, the electronic partition function is simplified to the degeneracy of the ground state, g_0.

$$q_{elec} = g_0 \tag{2.82}$$

A Harmonic oscillator is a common approximate model for the molecular vibrations. By the summation of all exponential terms involving the energy levels of each harmonic vibrational mode, in which the first vibrational energy is set to zero, the vibrational partition function for the vibrational mode *i*, $q_{\mathrm{vib,i}}$, for a polyatomic molecule is obtained as a close form in eq 2.83. The vibrational partition function for all vibrational modes is the product of all $q_{\mathrm{vib,i}}$ term (eq 2.84). Therefore, one needs to calculate vibrational frequencies, ν_i, to obtain the vibrational partition function. Note that for the transition state, there are only 3N-7 vibrational modes because one of the 3N-6 vibrational modes is transformed into translation mode along the reaction coordinate.

$$q_{vib,i} = \frac{1}{1 - e^{(-h\nu_i / k_B T)}} \tag{2.83}$$

$$q_{vib} = \prod_{i=1}^{3N-6(7)} \frac{1}{1 - e^{(-h\nu_i / k_B T)}} \tag{2.84}$$

The rotational energy levels are usually calculated by solving the Schrodinger equation for the rigid-rotor model. Since the energy spacing usually is much smaller than $k_B T$, the summation of the exponential terms can be replaced by the integral; then, the rotational partition function, q_{rot}, is obtained as eq 2.85, where σ is the symmetry index and I_i is the moment of inertia. Here, only the atomic mass and their positions (related to the moment of inertia) are needed to calculate rotational partition function.

$$q_{rot} = \frac{\pi^{1/2}}{\sigma} \left(\frac{8\pi^2 k_B T}{h^2} \right)^{3/2} (I_A I_B I_C)^{1/2} \tag{2.85}$$

The translation energy levels are calculated by solving the Schrodinger equation for the particle-in-a-box model. The translation energy levels are also very close to each other; thus the summation in the translational partition function, q_{trans}, can be replaced by the integral and the q_{trans} can be written as eq 2.86. Only the total molecular mass, *M*, is needed to calculate the translational partition function. Note that the translational partition function is volume (*V*) dependent.

$$q_{trans} = \left(\frac{2\pi M k_B T}{h^2} \right)^{3/2} V \tag{2.86}$$

The partition function for N distinguishable molecules, Q_{dis}, and N indistinguishable molecules, Q_{ind}, can be derived from the molecular partition function as shown in eq 2.87 and eq 2.88, respectively.

$$Q_{dis} = q^N \tag{2.87}$$

$$Q_{ind} = q^N/N! \tag{2.88}$$

The thermodynamic quantities of N molecules are related to the partition function as shown below, where the internal energy, enthalpy, and Gibbs free energy are the relative energies with respect to the electronic energy including zero-point energy and the ideal-gas approximation is used.

Internal energy: $$U = k_B T^2 \left(\frac{\partial \ln Q}{\partial T} \right)_V \tag{2.89}$$

Enthalpy: $$H = U + pV = k_B T^2 \left(\frac{\partial \ln Q}{\partial T} \right)_V + N k_B T \tag{2.90}$$

Entropy: $$S = k_B T \left(\frac{\partial \ln Q}{\partial T} \right)_V + k_B \ln Q \tag{2.91}$$

Gibbs free energy: $G = H - TS = Nk_BT - k_BT\ln Q$ (2.92)

2.12 Transition state theory

An elementary reaction is a reaction in which the products are formed directly from the reactants. Most reactions of interest consist of a series of elementary reactions together that can be constructed as the reaction mechanism. The activation energy of a given reaction can determine the possibility of the reaction mechanisms. In the experiment, one can measure rate constant (k) of the reaction, which is temperature (T) dependent, and find the activation energy (E_a) and Arrhenius factor (*A*) through the Arrhenius[80] equation (eq 2.93). Typically, the activation energy can be obtained by plotting ln k vs. 1/T; the slope gives $-E_a/R$ and the intercept is ln *A* (eq 2.94).

$$k(T) = Ae^{(-E_a/RT)} \tag{2.93}$$

$$\ln k = -\frac{E_a}{RT} + \ln A \tag{2.94}$$

This empirical solution to the observation is usually interpreted as E_a being the energy barrier for the reaction and *A* being a frequency factor.

Transition state theory (TST)[53,81] assumes that a reaction proceed from one energy minimum, the reactant, to another, the product, along the reaction path through the transition state (TS) without recrossing to reform the reactant and the transition state is in equilibrium with the reactant. Transition state theory is a semi-classical theory because the motion along the reaction coordinate is considered in a classical way but other motions in the perpendicular direction are quantized.

Based on transition state theory, the rate constant of the reaction A + B → C can be calculated from eq 2.95, where $Q^{\ddagger}$ is the partition function for all 3N-1 degrees of freedom (except for the motion along the reaction path) in the transition state, Q_A and Q_B are the partition functions for all degrees of freedom in the reactants, and E_0 is the energy difference between the transition state and the reactant at their zero-point energies.

$$k = \frac{k_B T}{h} \frac{Q^{\ddagger}}{Q_A Q_B} e^{(-E_0/k_B T)} \tag{2.95}$$

Eq 2.95 can be written as eq 2.96 where $K^{\ddagger}$ is the equilibrium constant for the transition state formation. This equilibrium constant is related to the free energy of activation through the van't Hoff relation (eq 2.98).

$$k = \frac{k_B T}{h} K^{\ddagger} \tag{2.96}$$

$$K^{\ddagger} = \frac{Q^{\ddagger}}{Q_A Q_B} e^{(-E_0/k_B T)} \tag{2.97}$$

$$\Delta G^{\ddagger} = -RT \ln K^{\ddagger} \tag{2.98}$$

Note that the Arrhenius equation in eq 2.93 is related to eq 2.95 through thermodynamic terms as will be shown. From the van't Hoff relation, eq 2.96 can be rewritten as eq 2.99 and 2.100. Then, we take the logarithm of *k* in 2.100 to compare eq 2.102 with eq 2.94.

$$k = \frac{k_B T}{h} e^{-\Delta G^{\ddagger}/RT} \tag{2.99}$$

$$k = \frac{k_B T}{h} e^{-\Delta H^{\ddagger}/RT} e^{\Delta S^{\ddagger}/R} \tag{2.100}$$

$$\Delta G^{\ddagger} = \Delta H^{\ddagger} - T\Delta S^{\ddagger} \tag{2.101}$$

$$\ln k = (\ln \frac{k_B T}{h}) - \frac{\Delta H^{\ddagger}}{RT} + \frac{\Delta S^{\ddagger}}{R} \tag{2.102}$$

By taking the derivative of ln k with respective to the temperature (T) from both eq 2.94 and eq 2.102 to obtain eq 2.103 and 2.104, respectively, the activation energy and Arrhenius factor are represented in term of $\Delta H^{\ddagger}$ and $\Delta S^{\ddagger}$, respectively.

$$\frac{d\ln k}{dT} = \frac{E_a}{RT^2} \tag{2.103}$$

$$\frac{d\ln k}{dT} = \frac{1}{T} + \frac{\Delta H^{\ddagger}}{RT^2} \tag{2.104}$$

$$E_a = \mathrm{RT} + \Delta H^{\ddagger} \tag{2.105}$$

$$A = \frac{k_B T}{h} e^{(1+\Delta S^{\ddagger}/R)} \tag{2.106}$$

Therefore, the activation energy determined from the experiment can be related to the $\Delta H^{\ddagger}$ and $\Delta S^{\ddagger}$ calculated from the partition functions of the transition state and the reactants.

2.13 Continuum solvation model

Most of the chemical reactions take place in solution. In order to achieve high accuracy in the calculation of chemical and physical properties of the reactions, it is important to consider the solvent-effects in the theoretical models.[82] Thus far the calculation methods described above consider the molecules only in gas phase while the solvent effect is also important, especially for charged molecules that have high energies in gas phase but can be stabilized in polar solvents. To represent the real solution, a large number of explicit solvent molecules needs to be included in the calculation of the solute, which is computationally expensive, particularly, for the high level quantum mechanical calculations. Therefore, continuum solvation models, which consider the solvent effects implicitly, are used in this dissertation for the calculation of the solvation free energy.

The solvation free energy is the change in the free energy to transfer molecule A in the gas phase into the condensed phase. The solvation free energy is composed of electrostatic and non-electrostatic contributions.

$$\Delta G_{solv} = \Delta G_{elec} + \Delta G_{non\text{-}elec} \tag{2.107}$$

When the solute from the gas phase is transferred to the solvent phase, the cavity of the solute size and shape is created in a medium. To create the cavity shape that reproduces the molecular shape, one can use a surface of constant electron density (isodensity surface) or construct the interlocking atomic spheres with the van der Waals radii. The *united atom* (UA) topology, in which the hydrogen spheres are included in the heavy atom sphere that they are bonded to, is also commonly used.

For the electrostatic contribution, once the solute molecule is placed into the continuum solvent, the charge distribution of the molecule induces the change of the electrostatic potential creating the electric field in the dielectric continuum medium, which in turn induces the change on the charge distribution of the solute. The charge distribution on the surface of the cavity, $\sigma(\mathbf{r}_s)$, can be represented in terms of the dielectric constant of the continuum medium, ε, and the gradient of the total electrostatic potential, ∇V_{tot}, perpendicular to the cavity surface (eq 2.108).[83]

$$\sigma(\mathbf{r_s}) = \frac{\varepsilon - 1}{4\pi\varepsilon}\nabla V_{tot}(\mathbf{r_s}) \tag{2.108}$$

The total electrostatic potential is the summation of the electrostatic potential from the charge distribution of solute (V_m) and the electrostatic potential from the polarized surface charge distribution of solute by dielectric medium (V_σ). The polarization potential V_σ can be calculated from the surface charge distribution $\sigma(\mathbf{r_s})$ as shown in eq 2.110, where **r** is the position vector and $\mathbf{r_s}$ is the position vector on the cavity surface.

$$V_{tot} = V_m + V_\sigma \tag{2.109}$$

$$V_\sigma(\mathbf{r}) = \int \frac{\sigma(\mathbf{r_s})}{|\mathbf{r} - \mathbf{r_s}|} d\mathbf{r_s} \tag{2.110}$$

A Hamiltonian of the solute in a continuum solvent is the summation of the gas phase Hamiltonian, $\mathbf{H^0}$, and the polarization potential V_σ.

$$\mathbf{H} = \mathbf{H^0} + \frac{V_\sigma}{2} \tag{2.111}$$

Since the wave function in the solution phase has different shape from the wave function in the gas phase, the distortion energy (the first two terms in eq 2.112) needs to be included in the calculation of the electrostatic contribution to the solvation free energy, ΔG_{elec}.

$$\Delta G_{elec} = \left\langle \Psi^{(sol)} \middle| \mathbf{H^0} \middle| \Psi^{(sol)} \right\rangle - \left\langle \Psi^{(gas)} \middle| \mathbf{H^0} \middle| \Psi^{(gas)} \right\rangle + \frac{1}{2}\left\langle \Psi^{(sol)} \middle| V_\sigma \middle| \Psi^{(sol)} \right\rangle \tag{2.112}$$

The polarization potential V_σ depends on the surface charge distribution, which is calculated from the wave function; therefore, the self-consistent reaction field (SCRF) formalism is used to solve for the HF (or Kohn-Sham) equation in the solution.

In practice, the analytical solution for the polarization potential V_σ can be found only for the cavity in a simple shape. For the molecular shape, the numerical method is required. In *polarizable continuum model* (PCM),[84] the cavity surface for the solute molecule is divided into small surface elements such that the $\sigma_i(\mathbf{r}_\mathrm{s})$ is approximated to be constant on each surface element i. Then, the polarization potential V_σ can be calculated from a set of point charges, q_i, which is derived from the product of $\sigma_i(\mathbf{r}_\mathrm{s})$ and the corresponding surface area A_i.

$$V_\sigma(\mathbf{r}) = \sum_i \frac{\sigma_i(\mathbf{r}_\mathrm{s})A_i}{|\mathbf{r}-\mathbf{r}_\mathrm{s}|} = \sum_i \frac{q_i}{|\mathbf{r}-\mathbf{r}_\mathrm{s}|} \tag{2.113}$$

In PCM, the solute is embedded in the continuum medium of constant dielectric ε as explained above. The different approach from the original PCM is the *conductor-like screening model* (COSMO),[85] in which the solute is embedded in the conductor medium ($\varepsilon = \infty$) instead of the dielectric medium. In the conductor medium, the total electrostatic potential at the surface is zero (eq 2.114).

$$V_{tot}(\mathbf{r}_\mathrm{s}) = V_m(\mathbf{r}_\mathrm{s}) + V_\sigma(\mathbf{r}_\mathrm{s}) = 0 \tag{2.114}$$

Therefore, the surface charge distribution in the conductor medium, $\sigma^*(\mathbf{r}_\mathrm{s})$, can be determined from $V_m(\mathbf{r}_\mathrm{s})$ instead of the gradient in eq 2.108, which is the advantage of this model. Note that the surface charge distribution, $\sigma^*(\mathbf{r}_\mathrm{s})$, need to be scaled back to the surface charge distribution in the proper ε dielectric medium, $\sigma(\mathbf{r}_s)$, through eq 2.115 where t is approximated to equal 0.5 in COSMO.

$$\sigma(\mathbf{r}_s) = \left(\frac{\varepsilon - 1}{\varepsilon + t}\right)\sigma^*(\mathbf{r}_s) \tag{2.115}$$

Modified from the original PCM by using the same idea of the conductor medium with parameter $t = 0$ to scale the surface charge distribution, CPCM[86] (conductor-like polarizable continuum model) is commonly used for the solvation calculation. For the high dielectric medium, such as water, the error from the surface charge scaling is considerably small.

Non-electrostatic contributions are derived from the cavitation, dispersion, and repulsion terms.

$$\Delta G_{\text{non-elec}} = \Delta G_{\text{cav}} + \Delta G_{\text{dis-rep}} \tag{2.116}$$

The cavitation free energy is the work to create a vacuum of the solute size and shape against the solvent pressure. The action also causes the reorganizing of the solvents around the solute, specially the solvent molecules at the first solvation shell. Thus, the cavitation free energy depends directly on the cavity surface area. To simplify the problem, the liquid atoms or molecules are approximated as hard spheres. The *scaled particle theory* connects between the hard spheres and the real liquids by using the radii that are modified to satisfy the experimental properties. For a hard sphere solute using solvent-excluded cavity, i.e. the cavity radius is $R = R_M + R_S$, where R_M is the solute radius and R_S is the solvent radius, the cavitation free energy can be calculated through the R_M/R_S ratio and the auxiliary function y (eq 2.118) as shown in eq 2.117, simplified from the expression by Pierotti,[87] where N_A is the Avogadro's number and V_s is the molar volume of the solvent.

$$\Delta G_{cav}^{sphere} = RT\left\{-\ln(1-y)+\frac{3y}{1-y}\left(\frac{R_M}{R_S}\right)+\left[\frac{3y}{1-y}+\frac{9}{2}\left(\frac{y}{1-y}\right)^2\right]\left(\frac{R_M}{R_S}\right)^2\right\} \quad (2.117)$$

$$y=\frac{\pi}{6}(2R_S)^3\left(\frac{N_A}{V_s}\right) \quad (2.118)$$

For the solute in the molecular shape, Claverie[88] suggested the calculation of the cavitation free energy by the summation of the cavitation free energy of each atomic sphere in the solute weighed by the area of each atom that is exposed to the solvent (S_k).

$$\Delta G_{cav} = \sum_{k=1}^{N}\frac{S_k}{4\pi R_k^2}\Delta G_{cav}^{sphere} \quad (2.119)$$

The dispersion and repulsion energies cause by the quantum mechanical effect related to the electron correlation in the solute-solvent interactions. The average dispersion-repulsion energy can be expressed as the sum of the atom-atom pair interaction between atom *m* of solute and atom *s* of solvent, $U(\mathbf{r_{ms}})$, weighed by the distribution function, $g(\mathbf{r_{ms}})$ (eq 2.120).

$$\left\langle E_{dis-rep}\right\rangle = \sum_{m\in M}\sum_{s\in S}\int U(\mathbf{r_{ms}})g(\mathbf{r_{ms}})dr_{ms} \quad (2.120)$$

The $U(\mathbf{r_{ms}})$ derives from dispersion and repulsion interaction (eq 2.121), where the coefficients $d_{ms}^{(k)}$, c_{ms}, and γ_{ms} in $U_{dis}(\mathbf{r_{ms}})$ and $U_{rep}(\mathbf{r_{ms}})$ terms are empirical parameters.

$$U(\mathbf{r_{ms}}) = U_{dis}(\mathbf{r_{ms}})+U_{rep}(\mathbf{r_{ms}}) \quad (2.121)$$

$$U_{dis}(\mathbf{r_{ms}}) = -\sum_{k=6,8,10} d_{ms}^{(k)}r_{ms}^{-k} \quad (2.122)$$

$$U_{rep}(\mathbf{r_{ms}}) = c_{ms}e^{-\gamma_{ms}r_{ms}} \tag{2.123}$$

In PCM, the dispersion and repulsion free energies are approximated from the average dispersion-repulsion energy, in which the $U_{dis}(\mathbf{r_{ms}})$ and $U_{rep}(\mathbf{r_{ms}})$ terms are also truncated; $\Delta G_{dis\text{-}rep}$ is expressed in the terms of cavity surface area and the auxiliary functions A_{ms}^{dis} and A_{ms}^{rep}, where ρ_s is the density of the solvent, N_s is the number of atom of type s in solvent molecule, $\mathbf{n_k}$ is a normal vector at the surface area a_k, and $d_{ms}^{(6)}$ and ϑ_{ms} are empirical parameters.

$$\Delta G_{dis\text{-}rep} = \rho_s \sum_k \sum_{s \in S} N_s \sum_{m \in M} a_k (A_{ms}^{dis} + A_{ms}^{rep}) \bullet \mathbf{n_k} \tag{2.124}$$

$$A_{ms}^{disp} = -\frac{1}{3}\frac{d_{ms}^{(6)}}{r_{ms}^{6}}\mathbf{r_{ms}} \tag{2.125}$$

$$A_{ms}^{rep} = \frac{1}{9}\frac{\vartheta_{ms}}{r_{ms}^{12}}\mathbf{r_{ms}} \tag{2.126}$$

Finally, the total solvation free energy is obtained from the combination of all electrostatic and non-electrostatic contributions. Note that other components related to the solvation process such as the hydrogen bonding which is derived from the short range interaction are not included in the continuum solvation models.

The solvation free energy obtained from the procedure presented above is normally in the standard state at 1 mol/L (1 M) whereas the gas phase free energy is calculated at 1 atm. The gas phase free energy of the reaction at 1 atm (ΔG^{o}) can be converted to the gas phase free energy at 1 M ($\Delta G^{o'}$) through eq 2.127,

$$\Delta G^{o'} = \Delta G^{o} + RT\ln(\frac{n^{o'}}{n^{o}}) \tag{2.127}$$

where n^{o} and $n^{o'}$ are the reaction quotients, which are the ratio of concentrations that appear in the equilibrium constant, at 1 atm and at 1 M, respectively. The molar volume of a perfect gas is 22.47 L mol^{-1} at room temperature (298.15 K) and 1 atm for ideal gas. In the reaction of A + B → C, the reaction quotient n is [C]/[A][B]. Assuming A, B, and C are ideal gases, their concentration at 1 atm are 1/22.47 M. The eq 2.127 can be written as eq 2.128.

$$\Delta G^{o'} = \Delta G^{o} + RT\ln\left(\frac{\frac{1}{1\cdot 1}}{\frac{24.47\cdot 24.47}{24.47}}\right) \tag{2.128}$$

$$\Delta G^{o'} = \Delta G^{o} - RT\ln(24.47) = \Delta G^{o} - 1.89 \qquad \text{(in kcal/mol)} \tag{2.129}$$

At room temperature, the gas phase free energy of the bimolecular reaction to form a single product at 1 M (in kcal/mol) can be calculated from the gas phase free energy at 1 atm through the factor in eq 2.129.

CHAPTER III

DENSITY FUNCTIONAL STUDY OF THE COMPLETE PATHWAY FOR THE HECK REACTION WITH PALLADIUM DIPHOSPHINES*

3.1 Introduction

The Heck reaction, one of the most utilized cross-coupling reactions, is the palladium-catalyzed arylation of the olefin with an organic halide under basic conditions (Scheme 1.1). Since its independent discovery in the early 1970s by Heck[10] and Misoroki,[11] the Heck reaction has been widely used as a tool for organic synthesis because of its importance in the direct attachment of olefinic groups to aromatic rings.[12,89-96] Numerous review articles on various aspects of the Heck and other cross-coupling reactions with palladium catalysts have been published.[12,13,16-18,20,96-102] Many types of ligands have been explored for the palladium catalysts in the Heck reaction, e.g., phosphine,[10,103-108] carbene,[109,110] amine[111] and thiolate.[112] Even a "ligand-free" system has been shown to function well.[24,25] Among these different ligands, the phosphines; especially, the monodentate ones are still the most widely used.[89-95]

The traditional mechanism[13,102] for the reaction is well known (Scheme 3.1). The oxidative addition of organic halide (RX) to the palladium(0) catalyst (Pd^0L_2) generates

---

*Reproduced with permission from Surawatanawong, P.; Fan, Y.; Hall, M. B. *J. Organomet. Chem.* **2008**, *693*, 1552-1563.

a cis-RPd^{II}XL$_2$ complex. Then, the olefin coordinates to Pd and inserts into the Pd-R bond by a migratory insertion mechanism. A new substituted alkene is produced and released by β-hydride transfer/olefin-elimination. Finally, a base removes HX to regenerate the active Pd complex.

Scheme 3.1 Traditional Heck reaction mechanism.
("PdL" could be any of the four species that are shown above.)

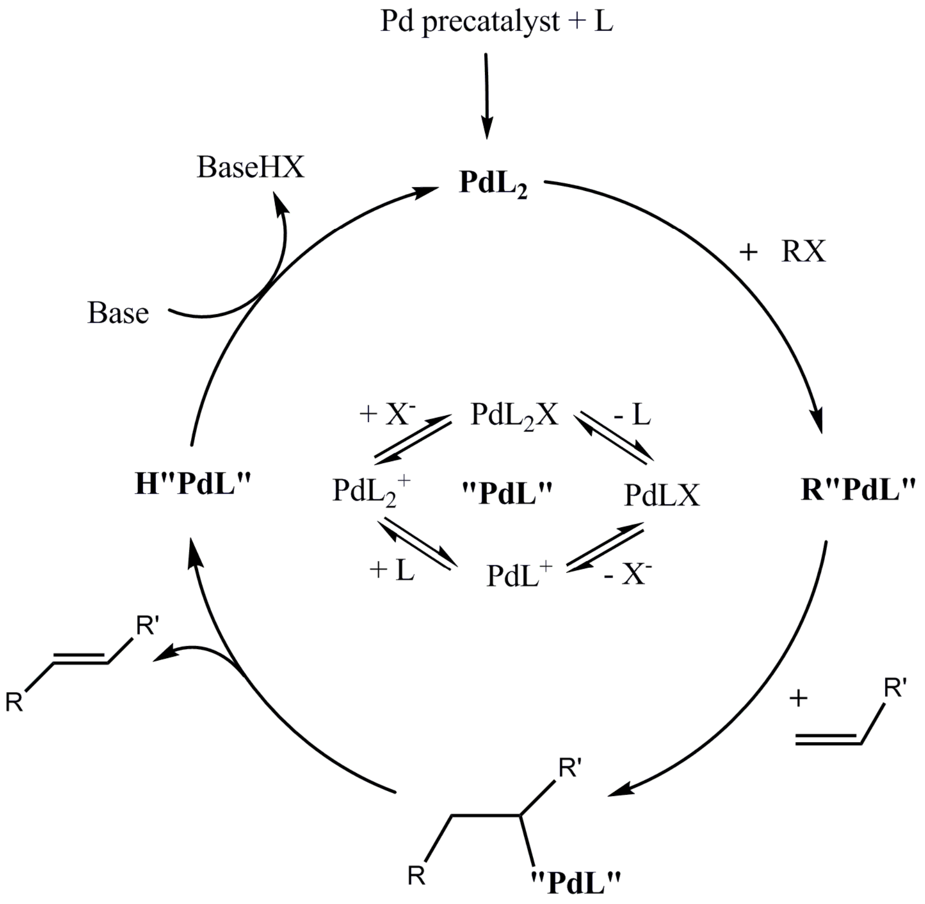

The oxidative addition is considered as a key step of the reaction cycle.[113] For monodentate phosphine ligands, the palladium diphosphines were believed to be the active species, with which the aryl halides undergo oxidative addition.[102,114,115] Recently, there has been more evidence for palladium monophosphines as the active catalysts.[18,100] In a study of Suzuki coupling, Littke et al. showed that 1:1 and 1:1.5 ratios of Pd:P gave higher catalytic activity than the 1:2 ratio.[116] Furthermore, Hartwig and coworkers isolated a series of T-shaped three-coordinated palladium compounds $[Pd(Ph)(X)(PR_3)]$,[21,117] which confirmed the existence of intermediate monophosphine palladium species. Another concern at this step of the reaction is that the olefin can also bind to the palladium catalyst. By forming a π-complex before the oxidative addition of aryl halides, high olefin concentrations can slow down the reaction due to the competition between the olefin and the ryl halide for the vacant site in the active palladium species.[118,119]

After the oxidative addition, the reaction proceeds through the migratory insertion and β-hydride transfer/olefin-elimination steps. From kinetic study, the associative mechanism of olefin insertion via a five-coordinate intermediate is unlikely.[120-122] In the dissociative mechanism there are two possible pathways:[102] (i) a neutral pathway via the dissociation of one phosphine ligand and, (ii) a cationic pathway via the dissociation of the halide ligand. With phenyl halides as substrates and phosphines as ligands, the dissociation of phosphine is more likely because of the weaker Pd-P bond relative to the Pd-X bond.[123] It is important to point out that the reaction can switch from one pathway to the other when the reaction conditions change.[124]

Key steps in the mechanism for Pd-mediated cross-coupling reactions, including the Heck reaction, have been studied by theory,[123,125,126] especially the oxidative addition of aryl halides to palladium complexes. In early studies, only oxidative additions to palladium diphosphines were considered[127-129] until Ahlquist et al. concluded that monophosphines were important as the major contribution to the reaction barriers arises from phosphine dissociation.[130,131] The insertion and elimination steps for the Heck reaction have also been studied. Roesch and coworkers found that the cationic pathway is preferred for carbene ligands because of the stronger Pd-C bond relative to the Pd-halide bond.[125] Assuming the neutral pathway, Guo and coworkers studied the full catalytic cycle of the Heck coupling by comparing palladium to nickel complexes with PH_3 as model ligands and vinyl halides as substrates.[123] Sundermann et al. studied the Pd(II)/Pd(IV) mechanism by the oxidative addition of phenyl iodide to palladium(II) bidentate phosphine complexes leading to octahedral Pd(IV) complexes.[126] Although the overall free energy barriers in the oxidative addition step for Pd(II)/Pd(IV) is significantly larger than that for Pd(0)/Pd(II), they concluded that olefin binding and iodide dissociation result in more difficult oxidative addition via Pd(0)/Pd(II) than Pd(II)/Pd(IV).

Although sterically hindered ligands are used in the reaction, the catalytic cycle of the Heck reaction were computed using over-simplified or truncated ligands and substrates, such as small phosphine ligands (PH_3 or PMe_3) and vinyl halides (instead of aryl halides). For experimentally used phosphines, only the oxidative addition step has been studied.[130,131] Moreover, the Heck reaction cycle actually involves several possible pathways; previous calculations covered some of these aspects but not all of them. To the best of our knowledge, complexities such as solvent effects, the size of PR_3 ligands and competing pathways, in the catalytic cycle of the Heck reaction has not been studied theoretically. Here, we calculated the pathways in the oxidative addition of phenyl bromide to palladium complexes with diphosphine, monophosphine and/or olefin as alternative ligands. In the migratory insertion, β-hydride transfer/olefin elimination, and catalyst recovery, both neutral and cationic pathways were calculated. The experimental phosphine ligands (PPh_3) were used and compared with the model phosphine ligands (PH_3 and PMe_3) throughout the reaction.

3.2 Computational details

All calculations were performed with the Gaussian03 program package.[132] The density functional, PBE,[73] was used for geometry optimization with modified LANL2DZ+f basis set for Pd, LANL2DZdp for P and Br atoms with effective core potentials (ECP),[133-135] 6-31++G(d',p')[136-138] for C and H atoms except for those on the phosphine's phenyl rings, where we use 6-31G(d).[136-138] Geometry and frequency calculations were performed with the PBE functional because the density fitting procedure increases the speed of these calculations. Previous work[139] has shown that the B3LYP energies are similar to CCSD(T) for CH_4 oxidative addition to Pd. Our own test calculations showed less than 1 kcal/mol between B3LYP//PBE and all B3LYP calculations. Therefore, single point energies were recalculated with the B3LYP functional[140,141] using the same basis set. All structures were fully optimized with default convergence criteria, and frequency calculations were calculated to ensure that there are no imaginary frequencies for minima and only one imaginary frequency for transition states. Zero point energies and thermodynamic functions were calculated at 298.15 K and 1 atm. The B3LYP solvation energies were calculated on the geometries from PBE gas-phase optimizations by using CPCM[86,142] method with UAKS atomic radii and solvation parameters corresponding to DMSO (ε = 46.7). By using B3LYP//PBE/6-31G(d) method with CPCM model and UAKS atomic radii, test calculation of the solvation free energy of CH_3NH_3 and N-methylacetamide, in which the experimental solvation energies are available,[143] gave an error of less than 1 kcal/mol. The standard states were corrected to 1 mol/L. The free energies and enthalpies shown in all figures and tables are relative to $Pd(PR_3)_2$ + PhBr + C_2H_4 + NEt_3.

3.3 Results and discussion

The results for the reaction pathway for $Pd(PR_3)_2$ catalyst with phenyl bromide and ethylene by density-functional theory combined with continuum solvation model are presented below beginning with an energy comparison for three possible pathways of the oxidative addition, and then the migratory insertion of the ethylene, the β-hydride transfer/olefin elimination of the product styrene, and the abstraction of proton by the NEt_3 base. The B3LYP relative enthalpies, gas-phase free energies and free energies with solvent correction of all involving species are represented. Unless specified otherwise, the free energies throughout the article refers to the B3LYP free energies with solvent correction. The relative free energies of the corresponding structures for different phosphine ligands were compared throughout.

3.3.1 The oxidative addition

In early studies of the Heck reaction, the phenyl bromide was believed to undergo oxidative addition on palladium diphosphine $Pd(PR_3)_2$ (eq 3.1).[102,114,115] Later, some workers found that ethylene can also coordinate to $Pd(PR_3)_2$ quite easily;[118,119] therefore, we also examined the oxidative addition of phenyl bromide on $Pd(PR_3)(\eta^2\text{-}C_2H_4)$ (eq 3.2). Recently, more evidence has accumulated that phosphine dissociation from $Pd(PR_3)_2$ occurs before the oxidative addition[18,100] (eq 3.3). We will discuss each of these pathways in this section.

$$Pd(PR_3)_2 + PhBr \rightarrow Pd(PR_3)_2(Br)(Ph) \qquad (3.1)$$

$$Pd(PR_3)(\eta^2\text{-}C_2H_4) + PhBr \rightarrow Pd(PR_3)(\eta^2\text{-}C_2H_4)(Br)(Ph) \qquad (3.2)$$

$$Pd(PR_3) + PhBr \rightarrow Pd(PR_3)(Br)(Ph) \qquad (3.3)$$

3.3.1.1 The oxidative addition to palladium diphosphine

First, we consider phenyl bromide undergoing oxidative addition directly to the palladium diphosphine. The optimized geometry of $Pd(PR_3)_2$ **1** is nearly linear.[144] The Pd-P bond lengths are 2.29, 2.31, and 2.32 Å for R = H, Me, and Ph (Figure 3.1), respectively; the bond lengths increase slightly with the size of ligands. A π-complex, **17**, of the aryl halide with the palladium catalyst is believed to form before the oxidative addition.[123,145] The Pd-C(11) bonds are slightly shorter than Pd-C(18) bonds because the bromide, an electron-withdrawing group, is attached to C(11). The formation of **17** increases the free energy by 16.52, 25.91, and 27.79 kcal/mol for R = H, Me, and Ph (Table 3.1), respectively. The entropy disfavors this associative reaction and the relative gas-phase enthalpies (Table 3.1) are also positive.

The free energies of the transition states for the oxidative addition, **2-TS**, are 25.00, 33.46, and 35.77 kcal/mol for R = H, Me, and Ph. The higher free energies correspond to larger P-Pd-P angles of 110.9°, 119.4°, and 127.1° for R = H, Me, and Ph, respectively, and larger dihedral angles [C(11)-Br(10)-Pd(1)-P(2)] of 66.4°, 69.1°, and 85.0°. The most sterically hindered phosphines are the most deformed from square

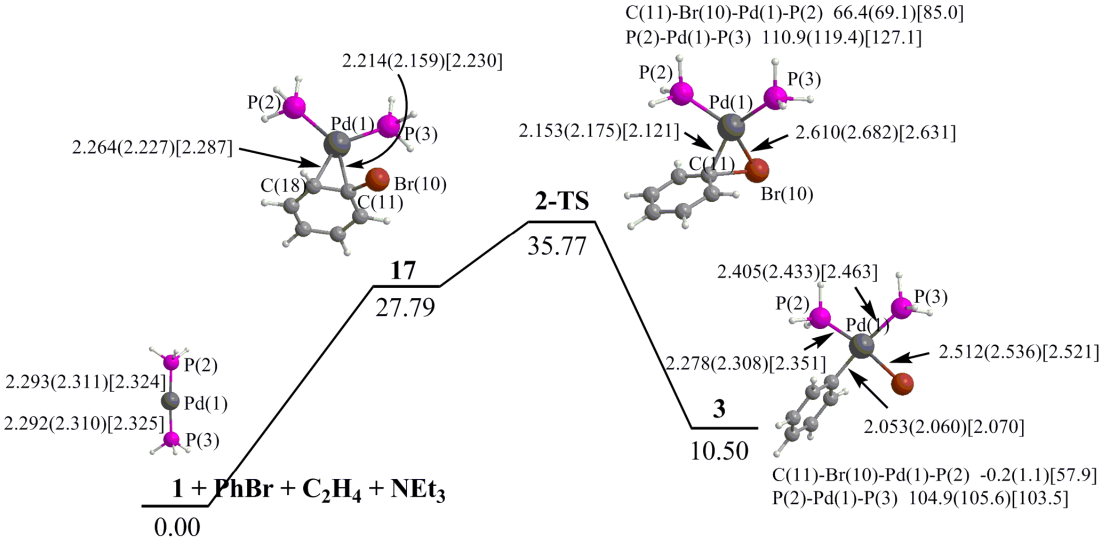

Figure 3.1 Free energy profiles for the oxidative addition to palladium diphosphine. The relative free energies in DMSO solution for PPh_3 are given in kcal/mol. Calculated bond distances and angles for PH_3, PMe_3 (in parentheses), and PPh_3 (in brackets) are given in Å and deg. To simplify the figure, only the structures for PH_3 are shown.

Table 3.1 The B3LYP relative enthalpies, gas phase free energies, and free energies with solvent correction of palladium complexes in the oxidative addition.

	ΔH (1 atm)			ΔG_{gas} (1 atm)			ΔG_{Total} (1 M)		
	PH_3	**PMe_3**	**PPh_3**	**PH_3**	**PMe_3**	**PPh_3**	**PH_3**	**PMe_3**	**PPh_3**
1	0.00	0.00	0.00	0.00	0.00	0.00	0.00	0.00	0.00
17	5.78	8.60	5.52	16.30	22.10	17.90	16.52	25.91	27.79
2-TS	13.95	16.64	15.36	25.00	29.38	27.81	25.00	33.46	35.77
3	-13.11	-16.97	-5.30	-1.45	-4.59	8.57	-5.62	-8.09	10.50
29	-10.05	-6.93	-7.75	0.42	5.18	3.10	-2.22	4.53	5.22
19	1.94	7.39	7.49	2.96	6.82	4.13	2.56	2.32	-2.40
20	6.19	13.13	11.08	18.44	25.82	20.56	17.57	22.55	18.49
21-TS	16.60	23.05	21.26	29.20	35.57	32.07	28.01	32.93	29.48
22	-0.50	2.41	5.26	12.07	14.37	15.36	7.81	6.82	7.31
6	25.15	29.85	31.53	16.94	20.29	18.87	18.63	17.37	13.07
18	11.76	17.23	16.12	11.04	17.31	15.34	12.99	16.15	12.89
7-TS	18.51	23.43	22.24	20.09	24.46	22.72	22.37	23.39	20.99
8	1.50	1.72	2.17	2.55	2.22	1.82	1.21	-3.55	-3.91

planar. Strikingly, the free energy difference between the transition states **2-TS** and the π-complexes **17** is ~8 kcal/mol for all phosphine ligands. In the study by Toro-Labbe and coworkers, following the reaction force as a function of reaction coordinate, the structure reordering from reactant to transition state takes place in the early stage of structural change.[146] The difference in the free energy of **2-TS** for different phosphine ligands depends mainly on the energetic cost of distorting the linear structures.

The products from the oxidative addition are $Pd(PR_3)_2(Ph)(Br)$ **3** with two cis phosphines. The Pd-P(3) bond trans to the phenyl is ~0.12 Å longer than the Pd-P(2) bond trans to the bromide due to the strong trans effect of the phenyl. The Pd-Br and Pd-C(11) are ~0.10 Å shorter than those in **2-TS** as these bonds are fully formed in **3**. The steric effect from ligands appears more strongly in **3** than **2-TS**: (i) the σ-bound phenyl ring of **3** is nearly perpendicular to the palladium coordination plane for PH_3 and PMe_3 with dihedral C(18)-C(11)-Pd(1)-Br(10) angles of 89.8° and 87.3°, respectively, but the phenyl ring tilts to make a dihedral angle of 68.9° for PPh_3; and (ii) the cis-complexes **3** are square-planar structures for PH_3 and PMe_3 with dihedral C(11)-Br(10)-Pd(1)-P(2) angles of -0.2° and 1.1°, respectively, but for PPh_3 the square-planar structure is significantly distorted with a dihedral angle of 57.9°. Correspondingly, the relative free energies of **3** are -5.62, -8.09, and 10.50 kcal/mol for R = H, Me, and Ph, respectively.

3.3.1.2 The oxidative addition to ethylene-coordinated palladium monophosphine

In the reaction system, a π-complex of palladium diphosphine can be formed not only with phenyl bromide but also ethylene. Ethylene actually binds more strongly than phenyl bromide. The Pd-C bonds in $Pd(PR_3)_2(\eta^2\text{-}C_2H_4)$ **29** are shorter than the ones in **17** (Figure 3.1 and 3.2) and the free energies of **29** are significantly lower than **17** (Table 3.1). Amatore et al. suggested that the olefin coordination at this step decreases the reaction rate through the equilibrium **1** + $C_2H_4 \rightleftharpoons$ **29**, which reduces the concentration of **1**.[119] However, what if the π-complex of palladium diphosphine with the olefin proceeds to the oxidative addition with the phenyl bromide? How high is this free energy barrier?

Prior to oxidative addition, the dissociation of one phosphine from complex **29** creates $Pd(PR_3)(\eta^2\text{-}C_2H_4)$ **19** with a free energy increase for PH_3 but decreases for PMe_3

and PPh_3 (Table 3.1). Complex **19** is similar to **1** in that the palladium center coordinates to two ligands but with the ethylene replacing one phosphine ligand; the π-donor and π*-acceptor in the ethylene play the same role in stabilizing Pd as the lone-pair donor and σ*-acceptor in the phosphine. Again, a phenyl bromide π-complex, $Pd(PR_3)(\eta^2\text{-}C_2H_4)(\eta^2\text{-}PhBr)$ **20**, precedes the oxidative addition (Figure 3.2). For PH_3 and PMe_3 ligands, both π-complexes **20** and **17** are comparable in free energies while for PPh_3 ligands, complex **20** is 9.3 kcal/mol lower in free energy than **17** (Table 3.1, Figure 3.1 and 3.2). The same situation applies to the comparison of the free energies between the oxidative addition transition-states **21-TS** and **2-TS**. The results show that the replacement of one phosphine ligand by the ethylene is favorable for the oxidative addition of palladium complexes with the sterically-hindered ligands such as PPh_3.

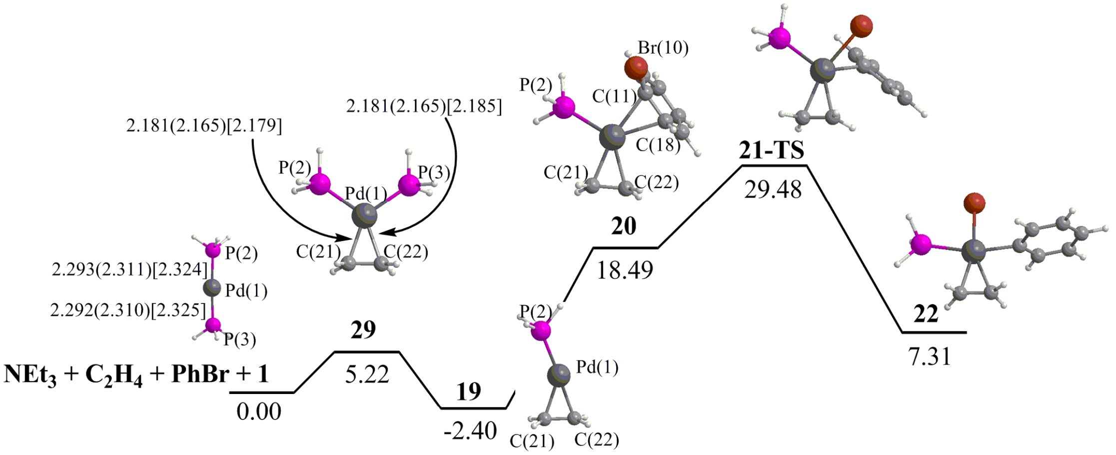

Figure 3.2 Free energy profiles for the oxidative addition to ethylene-coordinated palladium monophosphine. The relative free energies in DMSO solution for PPh_3 are given in kcal/mol. Calculated bond distances for PH_3, PMe_3 (in parentheses), and PPh_3 (in brackets) are given in Å.

3.3.1.3 The oxidative addition to palladium monophosphine

Monoligated palladium species have been proposed to be important intermediates in the catalytic cycle.[18,100] The isolation of three-coordinate palladium compounds, [Pd(PR_3)(Ph)(X)], with T-shaped geometries support the possibility of this pathway.[21,117] Thus, we examined phosphine dissociation from palladium diphosphine prior to the oxidative addition of the phenyl bromide. The Pd-P(2) bond in $PdPR_3$ **6** is 0.1 Å shorter than the one in $Pd(PR_3)_2$ (Figure 3.3); the shortened bond compensates, in part, for the loss of one metal-ligand bond. Importantly, the solvation contributes to this dissociation because both PR_3 and $Pd(PR_3)$ are polar molecules, while $Pd(PR_3)_2$ is not; with solvent correction, the relative free energies are less than the relative gas phase free energies by

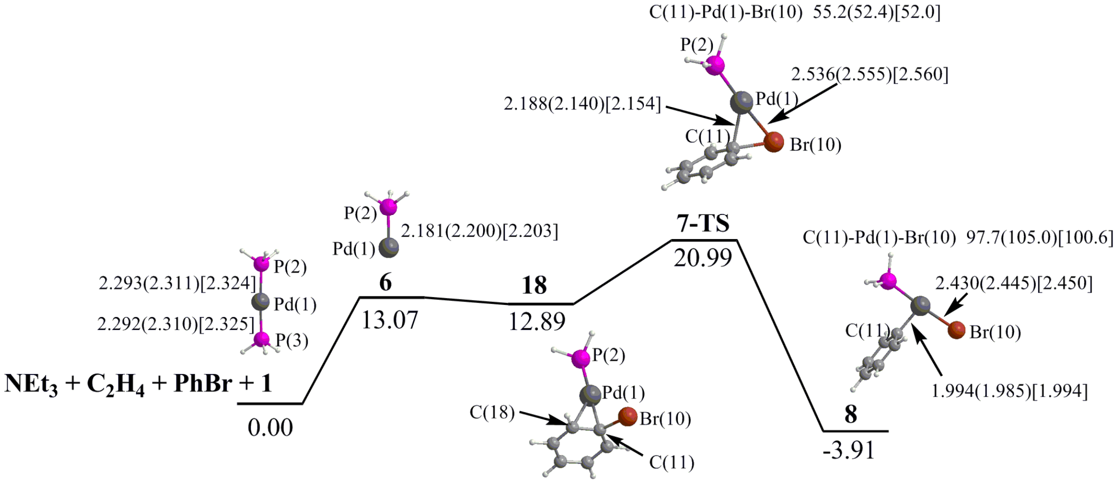

Figure 3.3 Free energy profiles for the oxidative addition to palladium monophosphine. The relative free energies in DMSO solution for PPh_3 are given in kcal/mol. Calculated bond distances and angles for PH_3, PMe_3 (in parentheses), and PPh_3 (in brackets) are given in Å and deg.

2.92 and 5.80 kcal/mol for PMe_3 and PPh_3. The calculations predict that more sterically-hindered ligands dissociate more easily; the dissociation free energies are 18.63, 17.37, and 13.07 kcal/mol for PH_3, PMe_3, and PPh_3, respectively (Figure 3.3 and Table 3.1). Ahlquist et al. reported that $Pd(PPh_3)(DMF)$ is more stable than $Pd(PPh_3)$ by -4.54 kcal/mol in the gas phase.[131] In strongly coordinating solvents, the monophosphine palladium, $PdPR_3$, species could bind to DMSO and form some $Pd(PR_3)(DMSO)$ in equilibrium with $PdPR_3$.

The monophosphine π-bound complexes of phenyl bromide, $Pd(PR_3)(\eta^2\text{-}PhBr)$ **18**, are formed with lower free energies than the more crowded π-bound complexes **17** and **20** (Table 3.1). Likewise, for the oxidative addition of phenyl bromide via transition state **7-TS**, the free energies of activation are lower than those of **2-TS** and **21-TS** for the corresponding phosphine ligands. Interestingly, the free energies of the **7-TS** are actually similar for all phosphine ligands; the main difference from different phosphine ligands is in the phosphine dissociation step. The **7-TS** structure has small ~52° C(11)-Pd-Br angles (Figure 3.3) as expected for an early transition state. Following transition state **7-TS** the system rearranges to the T-shaped structure $Pd(PR_3)(Ph)(Br)$ **8**, where the C(11)-Pd-Br angle ranges from 98^o to 105^o and the Pd-Br and Pd-C(11) bonds are shorter (Figure 3.3) than the ones in **7-TS**; the relative free energies of **8** are 1.21, -3.55, and -3.91 kcal/mol for PH_3, PMe_3, and PPh_3, respectively. These latter structures (**8**) are similar to those observed[21,117] and in both **7-TS** and **8** the bromide and the phosphine are trans to each other and phenyl group is trans to the empty site because the latter has the largest trans influence.

3.3.1.4 The probable oxidative addition pathway

The three pathways described above actually intersect as all three are connected by phosphine and ethylene association and dissociation (Scheme 3.2). The rate determining barrier for the oxidative addition is lowest on the monophosphine **7-TS**. Although the ethylene can form π-coordinated palladium diphosphine effortlessly, the oxidative addition to palladium with ethylene attached is unlikely due to the high barrier. However, the ethylene-coordinating palladium complex $Pd(PR_3)_2(\eta^2\text{-}C_2H_4)$ **29** can lose one phosphine (leading to **19**) and later lose ethylene to become palladium monophosphine **6** which can proceed to the oxidative addition through **7-TS** (Scheme 3.2). Similarly, when the phenyl bromide forms a π-complex with palladium diphosphine (leading to **17**), one phosphine can dissociate to generate $Pd(PR_3)(\eta^2\text{-}PhBr)$

Scheme 3.2 The equilibrium species prior to the oxidative addition (L = phosphine).

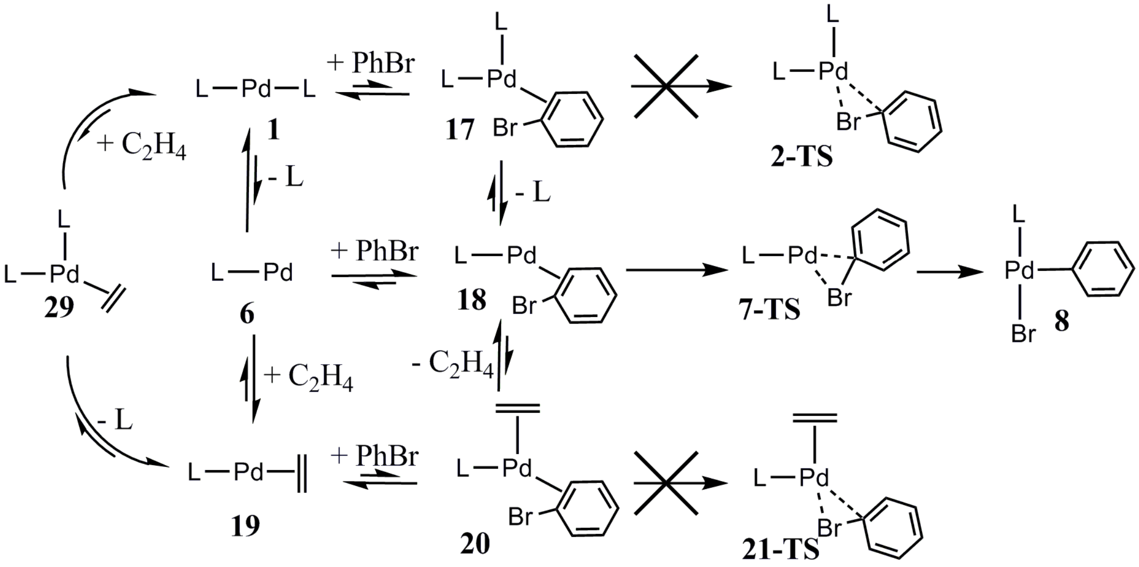

18, which can proceed to the oxidative addition through **7-TS**. According to our calculation, all of the possible pathways lead to palladium monophosphine as the active species that breaks the Ph-X bond in the oxidative addition step.

3.3.2 The migratory insertion, *β*-hydride transfer/olefin elimination, and catalyst recovery

For the remaining reaction steps: the migratory insertion of ethylene, the β-hydride transfer/olefin-elimination of the product styrene and the abstraction of proton by the base NEt_3, we examined two possible pathways: (i) neutral pathway — the olefin binds to a three-coordinated neutral species with one phosphine, one bromide, and one phenyl ligand (eq 3.4); and (ii) cationic pathway — the olefin binds to three-coordinate cationic (1+) species with two phosphines and one phenyl ligand (eq 3.5). We will compare and discuss both pathways for each step of the reaction.

$$Pd(PR_3)(Br)(Ph) + C_2H_4 \rightarrow Pd(PR_3)(Br)(Ph)(\eta^2\text{-}C_2H_4) \qquad (3.4)$$

$$[Pd(PR_3)_2(Ph)]^+ + C_2H_4 \rightarrow [Pd(PR_3)_2(Ph)(\eta^2\text{-}C_2H_4)]^+ \qquad (3.5)$$

3.3.2.1 The migratory insertion

In the neutral pathway, $Pd(PR_3)(Ph)(Br)$ (**8**) with the phenyl trans to the vacant site rearranges to **8b** with the bromide trans to the vacant site (Figure 3.4a). The free energy increases for **8b** because the phenyl with the high trans influence moves trans to phosphine, which weakens the Pd-P bond; the Pd-P in **8b** is longer by ~0.14 Å relative

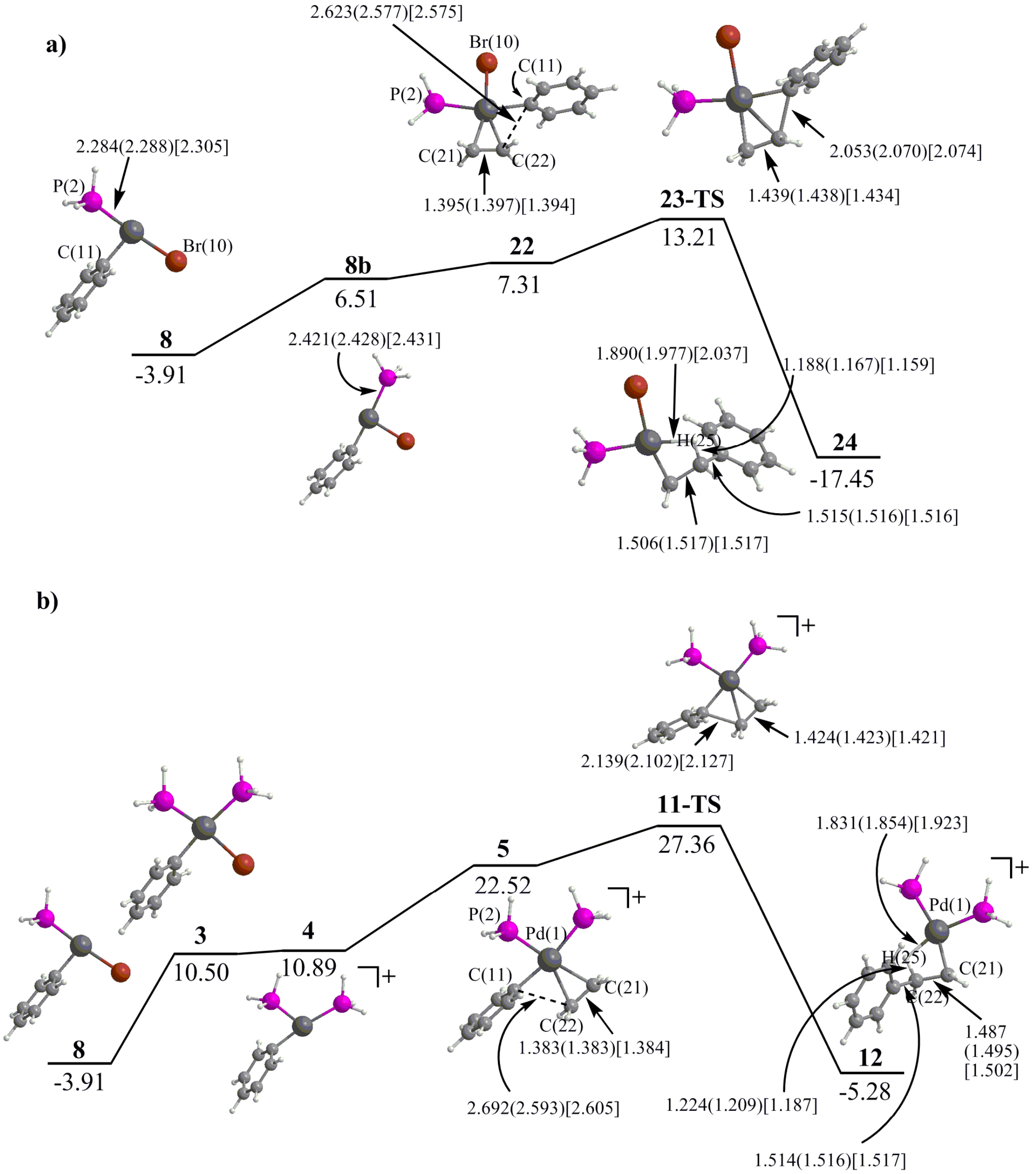

Figure 3.4 Free energy profiles for the migratory insertion in: (a) the neutral pathway and (b) the cationic pathway. The relative free energies in DMSO solution for PPh_3 are given in kcal/mol. Calculated bond distances for PH_3, PMe_3 (in parentheses), and PPh_3 (in brackets) are given in Å.

Table 3.2 The B3LYP relative enthalpies, gas phase free energies, and free energies with solvent correction of palladium complexes in the migratory insertion, β-H transfer/olefin elimination and catalyst recovery.

	ΔH (1 atm)			ΔG_{gas} (1 atm)			ΔG_{Total} (1 M)		
	PH_3	**PMe_3**	**PPh_3**	**PH_3**	**PMe_3**	**PPh_3**	**PH_3**	**PMe_3**	**PPh_3**
Neutral path									
Migratory insertion									
8	1.50	1.72	2.17	2.55	2.22	1.82	1.21	-3.55	-3.91
8b	10.76	13.08	13.22	10.35	12.42	9.87	10.81	9.64	6.51
22	-0.50	2.41	5.26	12.07	14.37	15.36	7.81	6.82	7.31
23-TS	6.19	7.33	10.32	20.40	20.11	21.94	15.28	12.11	13.21
β-H transfer/olefin elimination									
24	-18.45	-20.39	-18.96	-5.45	-7.73	-9.18	-10.58	-15.51	-17.45
25-TS	-10.99	-9.52	-8.36	2.56	3.87	2.55	-2.44	-3.82	-5.32
26	-14.05	-9.13	-8.05	-1.07	2.69	2.50	-5.06	-4.42	-2.73
Catalyst recovery									
27	-6.64	-7.08	-6.97	-6.91	-7.75	-10.34	-9.94	-15.88	-19.85
28	-22.34	-15.75	-18.80	-8.98	-2.27	-7.88	-15.96	-11.45	-16.00
31	105.24	109.94	111.63	101.62	104.98	103.56	-3.77	-5.02	-9.32
30	80.09	80.09	80.09	84.69	84.69	84.69	-22.39	-22.39	-22.39
Cationic path									
Migratory insertion									
8	1.50	1.72	2.17	2.55	2.22	1.82	1.21	-3.55	-3.91
3	-13.11	-16.97	-5.30	-1.45	-4.59	8.57	-5.62	-8.09	10.50
4	106.86	88.65	82.94	110.59	92.25	87.01	16.10	3.55	10.89
5	94.05	84.40	82.63	109.50	101.66	102.30	11.70	8.71	22.52
11-TS	99.64	88.73	86.39	115.86	107.64	106.91	18.62	14.92	27.36
β-H transfer/olefin elimination									
12	78.14	62.40	55.31	93.17	79.67	72.16	-3.69	-10.31	-5.28
13-TS	81.01	66.76	59.99	96.25	84.55	77.35	-0.08	-5.89	0.06
14	80.82	66.77	59.47	95.41	83.53	77.03	-0.19	-6.19	0.26
Catalyst recovery									
15	100.58	75.82	66.13	101.85	78.00	65.24	2.08	-14.15	-16.63
16	63.84	59.21	46.62	79.57	75.78	62.15	-12.56	-8.65	-12.24
30	80.09	80.09	80.09	84.69	84.69	84.69	-22.39	-22.39	-22.39

to that in **8**. The ethylene then binds to the vacant site of **8b** to form η^2-ethylene complex Pd(PR$_3$)(Ph)(Br)(η^2-C$_2$H$_4$) **22**. The square planar four-coordinated structure of **22** is slightly more stable than the T-shaped three-coordinated structure **8b** for PH$_3$ and PMe$_3$ ligands by ~3 kcal/mol but less stable for PPh$_3$ by 0.8 kcal/mol (Table 3.2). Species **22** lead to transition states **23-TS** with the C(11) from phenyl close to C(22) from ethylene (Figure 3.4a). In **23-TS**, C(11)-C(22) distance is about 0.5 Å shorter and the ethylene bond, C(21)-C(22), is about 0.04 Å longer than those in **22**. The free energy barriers relative to **22** are 7.47, 5.29, and 5.90 kcal/mol for PH$_3$, PMe$_3$, and PPh$_3$, respectively.

When the phenyl ring completes the migration from the metal to the ethylene, the intermediate species (**24**) has an agostic Pd-H(25) bond (Figure 3.4a). Compared with **23-TS**, the C(11)-C(22) bond lengths in **24** are shortened to ~1.51 Å, consistent with a C-C single bond (1.47 Å in free styrene from a PBE calculation in the same basis set). Moreover, the C(22)-C(21) bond distances are lengthened to a single bond at ~1.51 Å. The agostic hydrogen H(25) results in longer C(22)-H(25) bond lengths (1.19, 1.17, and 1.16 Å for PH$_3$, PMe$_3$ and PPh$_3$) and close Pd-H(25) contacts (1.90, 1.98, and 2.04 Å for PH$_3$, PMe$_3$ and PPh$_3$). The formation of the new C-C bond makes the formation of **24** exergonic by -10.58, -15.51, and -17.45 kcal/mol for PH$_3$, PMe$_3$, and PPh$_3$, respectively. In complexes **24** larger ligands (PR$_3$) correlated with the stronger C-H bond and weaker agostic interactions. In the gas phase, reactions involving charged-separation processes are difficult and the corresponding gas-phase enthalpies and free energies of **4** and all other cationic species are very high relative to neutral species (Table 3.2). However, in polar solvent, these charge species are stabilized; thus, solvation (and appropriate solvent correction) is important to compare the free energies between neutral and cationic species.

In the cationic pathway, the phosphine ligand binds to $Pd(PR_3)(Ph)(Br)$ **8** to form $Pd(PR_3)_2(Ph)(Br)$ **3**, then bromide ion dissociates from the palladium center, leading to $[Pd(PR_3)_2(Ph)]^+$ **4**, and the ethylene binds at the vacant site, forming $[Pd(PR_3)_2(Ph)(\eta^2\text{-}C_2H_4)]^+$ **5** (Figure 3.4b). The square-planar four-coordinate structure **5** is more stable than the T-shaped three-coordinate structure **4** by -4.40 kcal/mol for PH_3, but less stable by 5.16 and 11.63 kcal/mol for PMe_3 and PPh_3 (Figure 3.4b and Table 3.2). Then $[Pd(PR_3)_2(Ph)(\eta^2\text{-}C_2H_4)]^+$ **5** leads to the transition state **11-TS**; like **23-TS** in the neutral path, the C(11) from phenyl comes close to the C(22) in the ethylene while the C-C double bond in the ethylene is elongated in the migration process (Figure 3.4b). **11-TS** leads to the intermediate species **12** with an agostic bond interaction, like that in the neutral species **24**. For all phosphine ligands we studied, the free energy profiles of the cationic pathway lie above the neutral pathway for the migratory insertion step.

The cationic pathway is complicated by some additional issues. Experimentally, the trans isomer of $Pd(PR_3)_2(Ph)(Br)$ **3** is more stable than the cis analog.[147] We also calculated trans-$Pd(PR_3)_2(Ph)(Br)$ **3-trans** to be lower in energy than the cis **3** (PH_3 only). $[Pd(PR_3)_2(Ph)]^+$ **4** with two phosphine ligands in the cis position can easily isomerize to **4-trans** which can capture Br^- to form **3-trans** (Figure 3.5). The two trans isomers are lower in free energy by -4.12 and -2.29 kcal/mol than their cis isomers, respectively. However, to proceed to the migratory insertion step the ethylene has to be

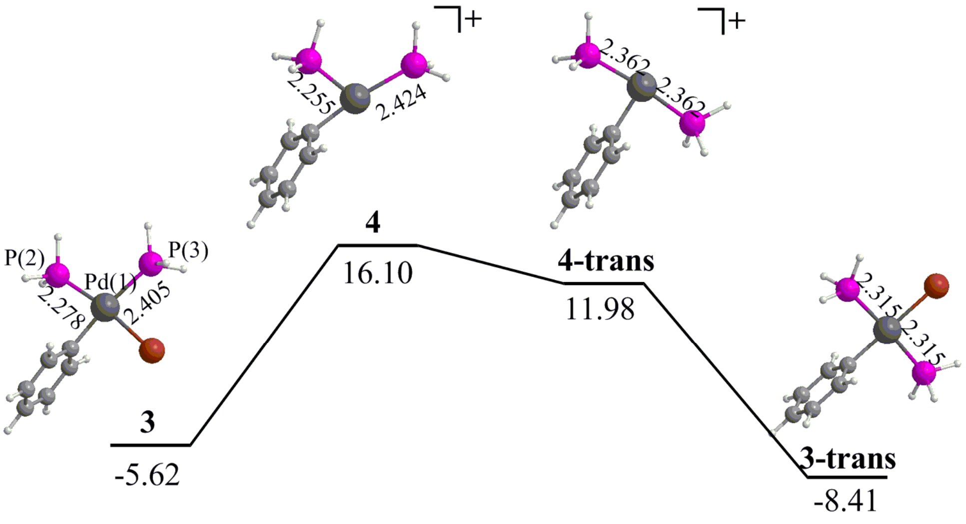

Figure 3.5 Free energy profiles for the cis/trans isomerization. The relative free energies in DMSO solution for PH_3 are given in kcal/mol. Calculated bond distances for PH_3 are given in Å.

cis to the phenyl. Thus, **3** and **4** are important intermediates in the cationic pathway but less stable than the unreactive **3-trans** and **4-trans**.

3.3.2.2 The *β*-Hydride transfer/olefin elimination

From the intermediate species **24**, the agostically bound β-hydrogen H(25) transfers from C(22) to palladium via transition state **25-TS** (Figure 3.6a). In **25-TS**, the Pd-H(25) bond shortens to 1.59 Å, C(22)-H(25) distance increases to 1.8 Å and the C(21)-C(22) bond shortens to 1.43 Å. The free energy barrier is 8.19, 11.69, and 12.13 kcal/mol for PH_3, PMe_3, and PPh_3, respectively (Table 3.2).

The intermediate produced through **25-TS**, $Pd(PR_3)(Br)(H)(C_2H_3Ph)$ **26**, has the C(22)-H(25) bond completely broken. Compared to **24**, the free energies of **26** increase

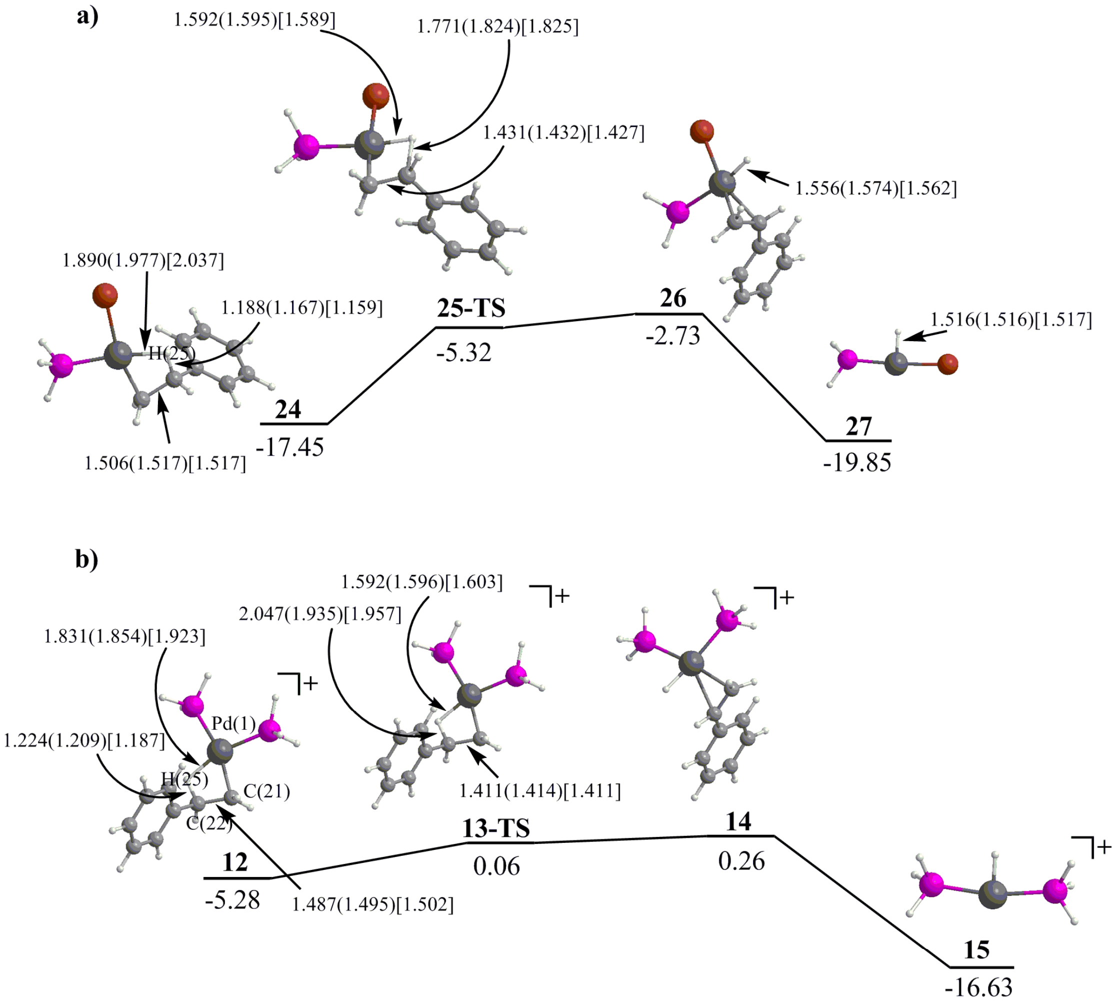

Figure 3.6 Free energy profiles for the β-H transfer/olefin elimination in: (a) the neutral pathway and (b) the cationic pathway. The relative free energies in DMSO solution for PPh_3 are given in kcal/mol. Calculated bond distances for PH_3, PMe_3 (in parentheses), and PPh_3 (in brackets) are given in Å.

by 5.52, 11.09, and 15.16 kcal/mol for PH_3, PMe_3, and PPh_3, respectively. Finally, styrene is released as product, which leaves $Pd(PR_3)(Br)(H)$ **27** in the T-shaped structure with the hydride opposite the empty site. In **27**, the Pd-H bonds are 0.05 Å shorter than those in **26**. The sterically-hindered ligands prefer **27** to **26**, as the free energy changes are -4.88, -11.46, and -17.12 kcal/mol for PH_3, PMe_3, and PPh_3, respectively.

In the cationic pathway, the agostic hydrogen in **12** is transfered from carbon to palladium through transition state **13-TS** (Figure 3.6b). The intermediate formed, $[Pd(PR_3)_2(H)(C_2H_3Ph)]^+$ **14**, then loses styrene leaving $[Pd(PR_3)_2(H)]^+$ **15** in a T-shaped structure with phosphines trans to each other and hydride opposite the empty site. Like styrene loss in the neutral pathway **26 → 27**, the sterically-hindered ligand drives styrene loss **14 → 15** with free energy changes of +2.27, -7.96, and -16.89 kcal/mol for PH_3, PMe_3, and PPh_3, respectively.

3.3.2.3 The recovery of the active catalyst

In order to close the catalytic cycle, a base in the reaction system abstracts the proton from $Pd(PR_3)(Br)(H)$ **27** in the neutral pathway and from $[Pd(PR_3)_2(H)]^+$ **15** in the cationic pathway. Here, we use NEt_3 as the base. As the nitrogen approaches the proton in **27** to form $Pd(PH_3)(Br)$--$(HNEt_3)$ **28**, the Pd-H bond is lengthened by ~0.5 Å (Figure 3.7a) and the N-H bond distance is ~1.1 Å. While the formation of the intermediate **28** relative to **27** is favored for PH_3 by -6.02 kcal/mol, its formation for PMe_3 and PPh_3 is disfavored by 4.43 and 3.85 kcal/mol, respectively (Figure 3.7a and Table 3.2). $HNEt_3^+$ and Br^- are eliminated from the palladium center with the free energies increasing by 12.19, 6.43, and 6.68 kcal/mol for PH_3, PMe_3, and PPh_3, respectively. However, when a phosphine ligand binds to regenerate $Pd(PR_3)_2$ in the end,

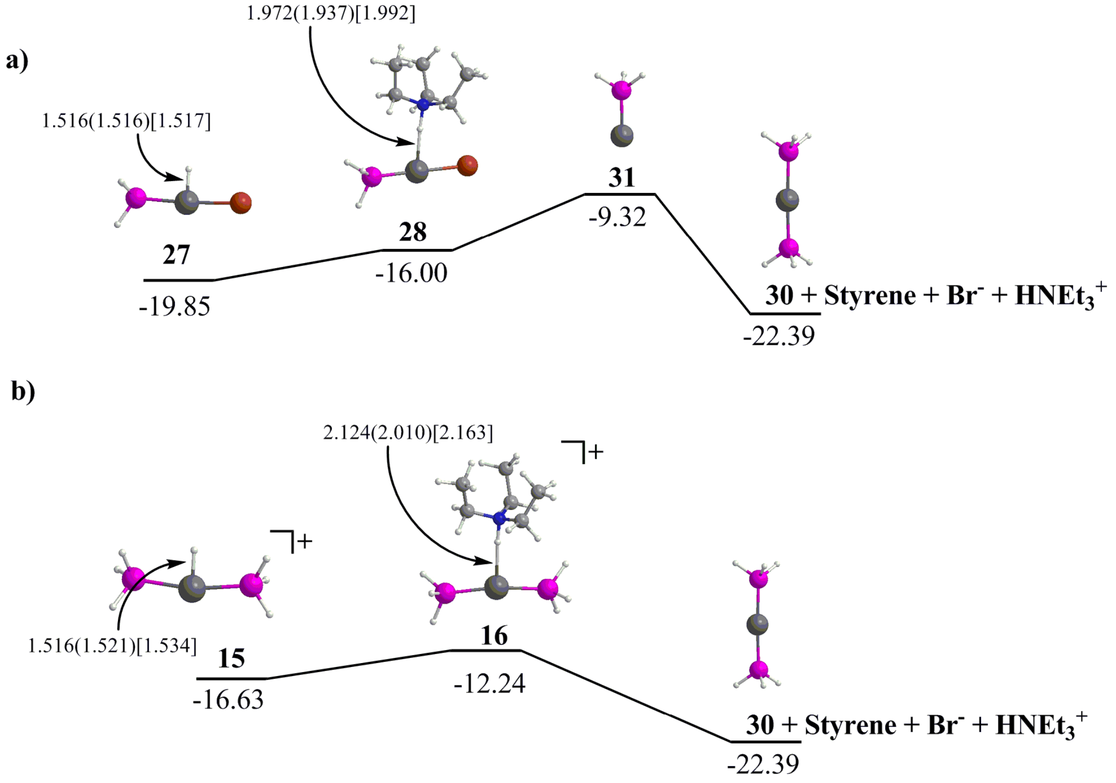

Figure 3.7 Free energy profiles for the catalyst recovery in: (a) the neutral pathway and (b) the cationic pathway. The relative free energies in DMSO solution for PPh_3 are given in kcal/mol. Calculated bond distances for PH_3, PMe_3 (in parentheses), and PPh_3 (in brackets) are given in Å.

the free energy decreases by -18.62, -17.37, and -13.07 kcal/mol for PH_3, PMe_3, and PPh_3, respectively.

As in the neutral pathway, NEt_3 abstracts the proton from $[Pd(PH_3)_2(H)]^+$ **15** in the cationic pathway to form $[Pd(PH_3)_2(H\text{--}NEt_3)]^+$ **16** with free energy changes -14.64, 5.50 and 4.39 kcal/mol for PH_3, PMe_3, and PPh_3, respectively (Figure 3.7b and Table 3.2). Finally, dissociation of $HNEt_3^+$ regenerates $Pd(PR_3)_2$ **1** with free energy decreases of -9.83, -13.74, and -10.15 kcal/mol for PH_3, PMe_3, and PPh_3, respectively.

3.4 Conclusions

By using density funtional theory combined with free energy corrections from a continuum solvation calculation, a cycle summarizing the complete reaction was developed (Scheme 3.3). The highest overall barrier in the catalytic cycle is the oxidative-addition step which is predicted to be the rate-determining step in agreement with experiments. For the oxidative addition to di-ligated palladium, palladium diphosphine and olefin-coordinated palladium monophosphine, the difference in the free energy barrier for different phosphines depends mainly on the energetic cost of distorting the linear structure, whereas for the oxidative addition to palladium monophosphine, the barrier depends mainly on the phosphine dissociation. More sterically-hindered phosphines cause an increasing barrier for the former but a decreasing one for the latter. The solvation contributes mainly to the lower free energy of phosphine dissociation of more sterically-hindered phosphine ligands. Phenyl bromide oxidative addition to palladium monophosphine is the most favorable pathway for all PH_3, PMe_3, and PPh_3 ligands. However, the palladium diphosphine can form π-bound complexes with either ethylene or phenyl bromide before losing one phosphine, or the ethylene, before undergoing the phenyl bromide oxidative addition (Scheme 3.3). For the remaining reaction steps: the migratory insertion, β-H transfer/olefin elimination, and catalyst recovery, the phosphine dissociation leads to neutral pathway and the bromide dissociation leads to cationic pathway. The charged-separation process in the cationic pathway causes very high corresponding gas-phase enthalpies and free energies

Scheme 3.3 Neutral mechanism of the Heck Reaction for palladium with monophosphine ligands (L).

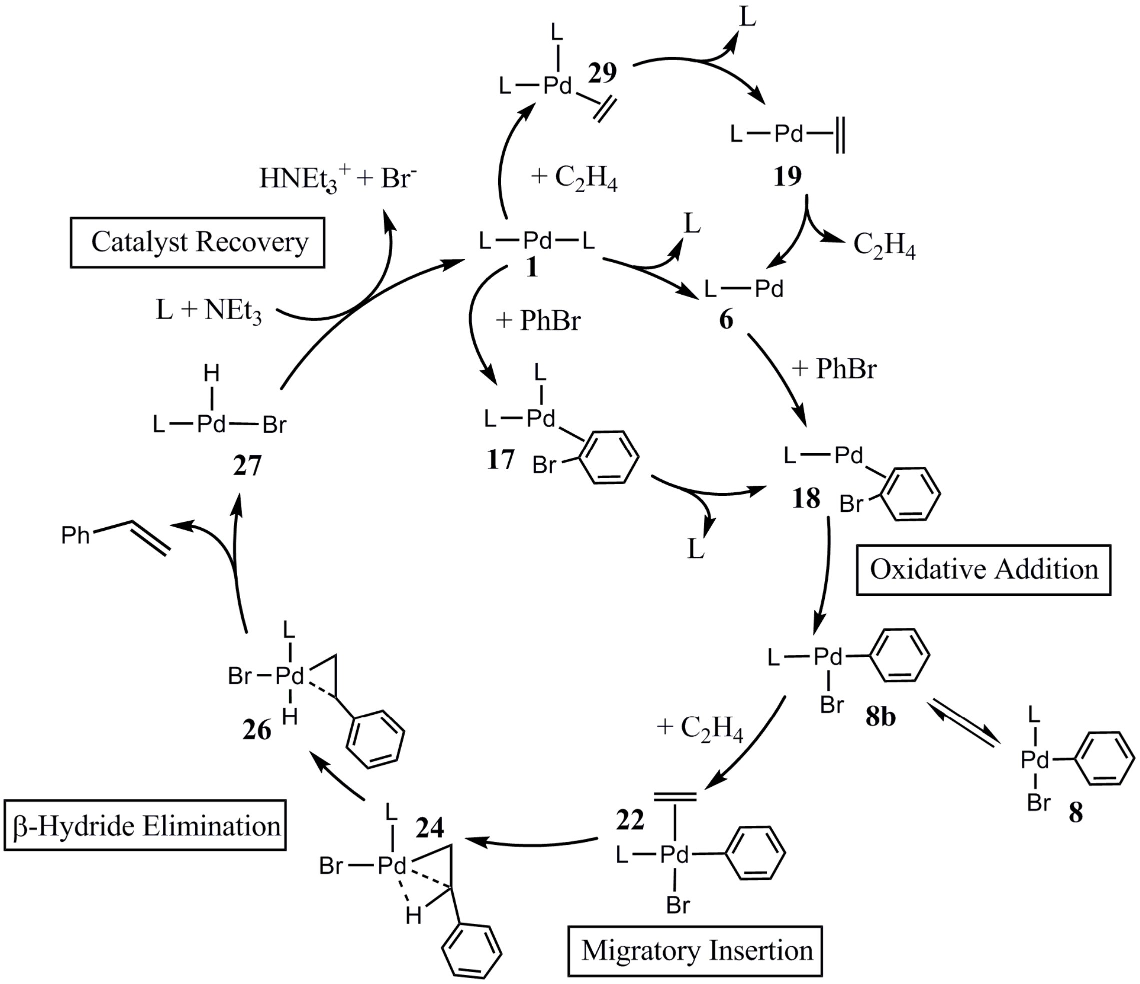

of all cationic species relative to neutral species; thus, incorporating solvent effect is very important to compare the free energies between neutral and cationic species. Even after these salvation corrections, the neutral pathway is found to lie below the cationic pathway, especially, for the sterically hindered phosphine ligand. The steric hindrance of phosphine ligands affects the free energy barrier particularly in the phosphine dissociation and the stability of four-coordinate structures.

The complexity of the Heck reaction can derive from the fact that there is more than one accessible pathway and different reaction conditions and ligand sets leading the overall reaction to proceed by different paths. Our conclusions apply primarily to palladium monodentate-phosphine complexes. Issues related to the palladium nanoparticles and "ligand free" palladium as intermediates[23-26] in the Heck reaction cycle will be examined in a future study.

CHAPTER IV

THEORETICAL STUDY OF ALTERNATIVE PATHWAYS FOR THE HECK REACTION THROUGH DIPALLADIUM AND "LIGAND-FREE" PALLADIUM INTERMEDIATES*

4.1 Introduction

The Heck reaction is the palladium catalyzed arylation reaction of an aryl halide and olefin to form a new C-C bond under basic conditions. A number of ligands, especially, phosphine ligands, have been developed to stabilize the palladium catalysts. Recently, a "ligand-free" palladium system has attracted considerable attention.[23-29] Reetz[28] and de Vries[26,28] proposed that the Pd nanoparticles observed in the ligand-free system are the reservoir for the active Pd(0) catalyst for the Heck reaction. The key success of these systems is to stabilize the palladium collioids to prevent the agglomeration and precipitation of palladium black, which terminates the reaction. Without phosphine ligands, additives such as tetraalkylammonium halides are used to decelerate palladium black formation[24] and to stabilize the Pd colloid,[148] which slowly releases the molecular palladium active species. Increasing substrate to catalyst ratio was also shown to enhance the turnover frequency and to prevent palladium black

---

*Reproduced with permission from Surawatanawong, P.; Hall, M. B. *Organometallics*, **2008**, *27*, 6222–6232. Copyright 2008 American Chemical Society.

formation because additional substrate shifts the equilibrium from palladium nanoparticles to catalytically active palladium molecules.[12,25,149]

During the course of the reaction under the "ligand-free" conditions studied by de Vries and co-workers, dipalladium intermediates with bridging iodides were detected and isolated.[26] Furthermore, several other studies have shown that dipalladium complexes can be catalysts in cross-coupling reactions. Hartwig and co-workers used $Pd_2(\mu\text{-}Br)_2(P^tBu_3)_2$ as the catalyst for Suzuki couplings and amination reactions.[21] In their comparison of two catalysts: (1) $Pd[P(o\text{-}Tol)_3]_2$, the monopalladium complex, and (2) $[Pd(P(o\text{-}Tol)_3)(Ar)(Br)]_2$ (Ar =Aryl), the dipalladium intermediate from the aryl halide oxidative addition, Herrmann and co-workers found that both mono- and dipalladium species gave similar results as the catalysts for the Heck reaction.[22]

A number of theoretical studies on the Heck reaction mechanism, particularly the oxidative-addition step, have been reported.[123,125,127-131,150,151] Close attention has been paid to mechanisms involving palladium stabilized by phosphine or carbene ligands. Recently, we examined competitive pathways involving the palladium phosphine complexes as catalysts in the Heck reaction and found that the monophosphinopalladium complex is the most favorable in comparison to diphosphinopalladium and ethylene-bound monophosphinopalladium for the oxidative addition of phenyl bromide, the rate determining step in our study.[152] Recent experimental results on "ligand-free" palladium systems and on dipalladium complexes increased our interest in alternative mechanism, as the palladium monophosphine that we studied can form the dipalladium, $Pd_2(PR_3)_2$, which could be an active catalyst in an alternative Heck reaction mechanism.

Furthermore, under "ligand-free" condition, substrate-bound palladium complexes could play a role as the active species. A recent theoretical study by Ahlquist et al. suggested that alkynes can serve as ligands for the oxidative-addition step in the hydroarylation reaction under phosphine-free conditions.[153,154] Likewise, the olefin substrate might serve as a ligand in the "ligand-free" Heck reaction. Here, we report computational investigations of alternative pathways for the Heck reaction via dipalladium, $Pd_2(PR_3)_2$, and substrate-bound palladium intermediates: free Pd, $PdBr^-$, and $Pd(\eta^2\text{-}C_2H_4)$, in comparison to mono-nuclear palladium phosphine, $Pd(PR_3)$. These density functional theory (DFT) computations which include both thermal and solvent corrections should help elucidate the relative importance of alternative pathways for the Heck reactions.

4.2 Computational details

All calculations were performed with Gaussian03 program packages.[132] The density functional, PBE[73], was used for geometry optimization with modified LANL2DZ+f basis set for Pd, LANL2DZdp for P and Br atoms with effective core potentials (ECP)[133-135], and 6-31++G(d',p')[136-138] for C, N, and H atoms except for those on the tertiary butyl, where we use 6-31G(d).[136-138] Geometry and frequency calculations were performed with the PBE functional because the density fitting procedure available in pure functionals increases the speed of these calculations. Previous work[139] has shown that the B3LYP energies are similar to CCSD(T) energies for CH_4 oxidative addition to Pd. Our own test calculations showed less than 1 kcal/mol between B3LYP//PBE and all B3LYP calculations for the oxidative addition of phenyl bromide to $Pd(PH_3)_2$ and $Pd(PH_3)$. Therefore, single point energies were recalculated with the B3LYP functional[140,141] using the same basis set. All structures were fully optimized with default convergence criteria, and frequencies were calculated to ensure that there are no imaginary frequencies for minima and only one imaginary frequency for transition states. Zero point energies and thermodynamic functions were calculated at 298.15 K and 1 atm. The solvation energies were calculated on the geometries from PBE gas-phase optimizations by using CPCM[86,142] method with UAKS atomic radii and solvation parameters corresponding to DMSO ($\varepsilon = 46.7$). With the CPCM method and UAKS atomic radii, test calculation of the solvation free energy of CH_3NH_3 and N-methylacetamide, for which the experimental[143] solvation energies are available, gave an error of less than 1 kcal/mol. The standard states were corrected to 1 mol/L. The energies and structural parameters of some models related to palladium monophosphine with the PMe_3 ligand were previously published,[152] but some of these results are shown here for comparison.

4.3 Results and discussion

The observed aggregation of palladium and of the dipalladium intermediates in the Heck reaction led to our interest in a reaction cycle based on dipalladium, $Pd_2(PR_3)_2$, as the active catalyst. The success of low-loading palladium in “ligand-free” conditions also prompted us to investigate reaction pathways involving phosphine-free substrate-bound palladium intermediates: free Pd, $PdBr^-$, and $Pd(\eta^2\text{-}C_2H_4)$. Generally, the following steps were examined: the oxidative addition of the phenyl bromide, the migratory insertion of the ethylene, β-hydride transfer/olefin elimination of the product styrene, and the abstraction of proton by NEt_3 base. The free energy profiles for the pathways involving dipalladium and substrate-bound palladium complexes will be discussed in comparison to monopalladium $Pd(PR_3)$. In all tables, figures and schemes, the B3LYP relative enthalpies, gas-phase free energies and free energies with solvent correction are relative to $Pd_4 + PR_3 + PhBr + C_2H_4 + NEt_3$ except for the ones for dipalladium complexes which are relative to $2Pd_4 + 2PR_3 + PhBr + C_2H_4 + NEt_3$. Unless specified otherwise, the energies mentioned throughout the article refer to the B3LYP relative free energies with solvent correction.

4.3.1 Pre-catalytic reaction

4.3.1.1 Ligand/substrate binding to atomic palladium

The observation of palladium nanoparticles in the Heck reaction led to suggestions that the active palladium catalyst is slowly released from palladium cluster during the reaction cycle.[23-29] The monopalladium leached from the cluster can be stabilized by ligands or substrates (eq 4.1). Tetra-nuclear palladium Pd_4 (**1**) is used as our model for a palladium cluster; the optimized geometry has tetrahedral symmetry with 2.642 Å Pd-Pd bonds. Ligand/substrate binding to a "released" palladium forms a mono-ligated palladium complex and tri-nuclear palladium Pd_3 (**2**), which is trigonal planar with 2.508 Å Pd-Pd bonds. In a comparison to the phosphine ligand, we examined the stability of palladium binding with substrates, which are ethylene, phenyl bromide and bromide ion, to mimic the "ligand-free" condition.

$$Pd_4 + L \rightarrow PdL + Pd_3 \qquad ; L = PMe_3, P^tBu_3, C_2H_4, PhBr, Br^- \qquad (4.1)$$

When phosphine binds to palladium, the formation of palladium monophosphine, $PdPR_3$ and tri-nuclear palladium from the tetra-nuclear palladium and phosphine is exergonic by -0.39 and -0.70 kcal/mol for $PdPMe_3$ (**6m**) and PdP^tBu_3 (**6t**), respectively (Table 4.1). The similar reaction for substrate binding leads to the formation of Pd(η^2-C_2H_4) (**32**) and Pd(η^2-PhBr) (**41**) complex with the energy changes of 3.06 and 17.08 kcal/mol, respectively. The π-donor and π*-acceptor in the ethylene play the same role in stabilizing Pd as the lone-pair donor and σ*-acceptor in the phosphine. The PhBr binds more weakly to palladium in part because the binding decreases the conjugation of the aromatic ring. De Vries proposed that halide ions plays a role to stabilize atomic palladium in the "ligand-free" mechanism for the Heck reaction.[24,26] In our calculation,

Table 4.1 Relative B3LYP//PBE enthalpy and free energy of ligand/substrate (L) binding in the reaction: $Pd_4 + L \rightarrow Pd_3 + PdL$

		ΔH	ΔG_{gas} (1 atm)	ΔG_{tot} (1 M)
Pd-Ligand				
6m	$Pd(PMe_3)$	2.26	2.02	-0.39
6t	$Pd(P^tBu_3)$	2.03	2.20	-0.70
Pd-Substrate				
32	Pd(η^2-C_2H_4)	10.07	9.12	3.06
41	Pd(η^2-PhBr)	22.41	21.50	17.08
60	$PdBr^-$	18.39	15.14	19.28

the formation of $PdBr^-$ produces an energy change of 19.28 kcal/mol. The high free energy change corresponds to the fact that bromide ion has π-donor but no π-acceptor capacity; therefore, without the backbonding interaction, the bromide ion is a poorer ligand than ethylene for the electron rich Pd atom.

These initial results show that the atomic palladium leached from a palladium cluster is stabilized by phosphine ligands in the presence of phosphines, but, in the absence of phosphine, the ethylene serves as a better ligand than either phenyl bromide or bromide ion.

4.3.1.2 Dipalladium formation

Experimentally, dipalladium complexes were found with the bridging ligands,[155] e.g., diene,[156] allene,[157] halogen,[158,159] and phosphine.[160] We examined the dimerization of palladium monophosphine to form the dipalladium diphosphine $Pd_2(PR_3)_2$ **44** (R = Me, and ^{t}Bu for **44m** and **44t**, respectively). With the PMe_3 ligand, the Pd(1)-Pd(2) bond distance in **44m** is 2.652 Å (Figure 4.1) and one phosphine ligand is semi-bridging between the two palladiums with a strong Pd(1)-P(1) bond, 2.227 Å, and a weak Pd(2)-P(1) bond, 2.870 Å. The other phosphine is attached solely to one palladium; Pd(2)-P(2) bond is 2.250 Å. In the semi-bridging interaction, the Pd(1)-P(1) bond tilts toward the neighboring Pd(2) atom to form a three-center four-electron bond (C(1)-P(1)-Pd(2) bond); P(1) begins to take on a 5-coordinate hypervalent (expanded octet) structure. The P^tBu_3 ligand's steric bulk prevents the bridging geometry; structure **44t** is nearly symmetrical**.** With the semi-bridging coordination of phosphine, the dipalladium **44m**

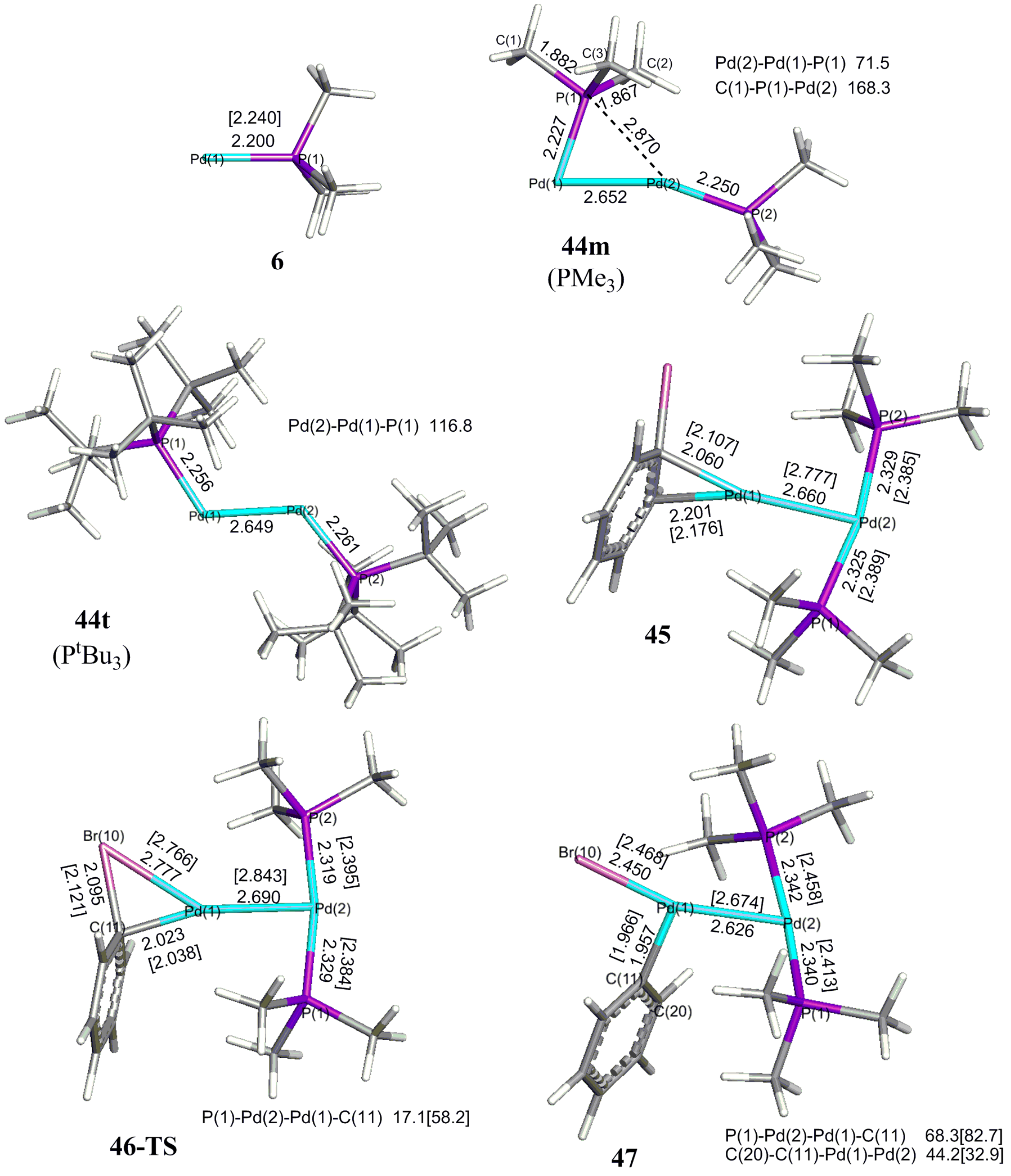

Figure 4.1 Molecular stuctures in the oxidative addition to dipalladium complex. Calculated bond distances and angles for PMe_3 and P^tBu_3 (in bracket) are given in Å and deg. Except for **44**, only the structures for PMe_3 are shown to simplify the figure.

Table 4.2 Relative enthalpy and free energy for the oxidative addition to phosphine-bound palladium complexes (R = Me and ^{t}Bu).

		PMe_3			P^tBu_3		
		ΔH	ΔG_{gas} (1 atm)	ΔG_{tot} (1 M)	ΔH	ΔG_{gas} (1 atm)	ΔG_{tot} (1 M)
Dipalladium							
1	Pd_4	0.00	0.00	0.00	0.00	0.00	0.00
6	$Pd(PR_3)$	2.26	2.02	-0.39	2.03	2.20	-0.70
44	$Pd_2(PR_3)_2$	-12.43	-3.53	-8.37	-12.59	-0.50	-0.49
45	$Pd_2(PR_3)_2(\eta_2$-PhBr)	-26.43	-5.78	-3.73	-21.94	2.98	10.20
46-TS	$TS1Pd_2(PR_3)_2(Ph)(Br)$	-23.09	-1.62	0.43	-17.94	7.13	13.54
47	$Pd_2(PR_3)_2(Ph)(Br)$	-43.86	-23.36	-24.39	-30.86	-6.56	-1.40
Monopalladium							
1	Pd_4	0.00	0.00	0.00	0.00	0.00	0.00
6	$Pd(PR_3)$	2.26	2.02	-0.39	2.03	2.20	-0.70
18	$Pd(PR_3)(\eta^2$-PhBr)	-10.36	-0.96	-1.61	-12.19	-1.46	-0.48
7-TS	$TS1Pd(PR_3)(Br)(Ph)$	-4.17	6.19	5.63	-8.75	2.28	2.53
8	$Pd(PR_3)(Br)(Ph)$	-25.87	-16.05	-21.31	-24.06	-13.55	-16.67

Scheme 4.1 Solvation (DMSO) corrected relative free energy (kcal/mol) profiles for the oxidative addition of phenyl bromide to di- and monopalladium complexes (in brackets) for PMe_3 and P^tBu_3 ligands.

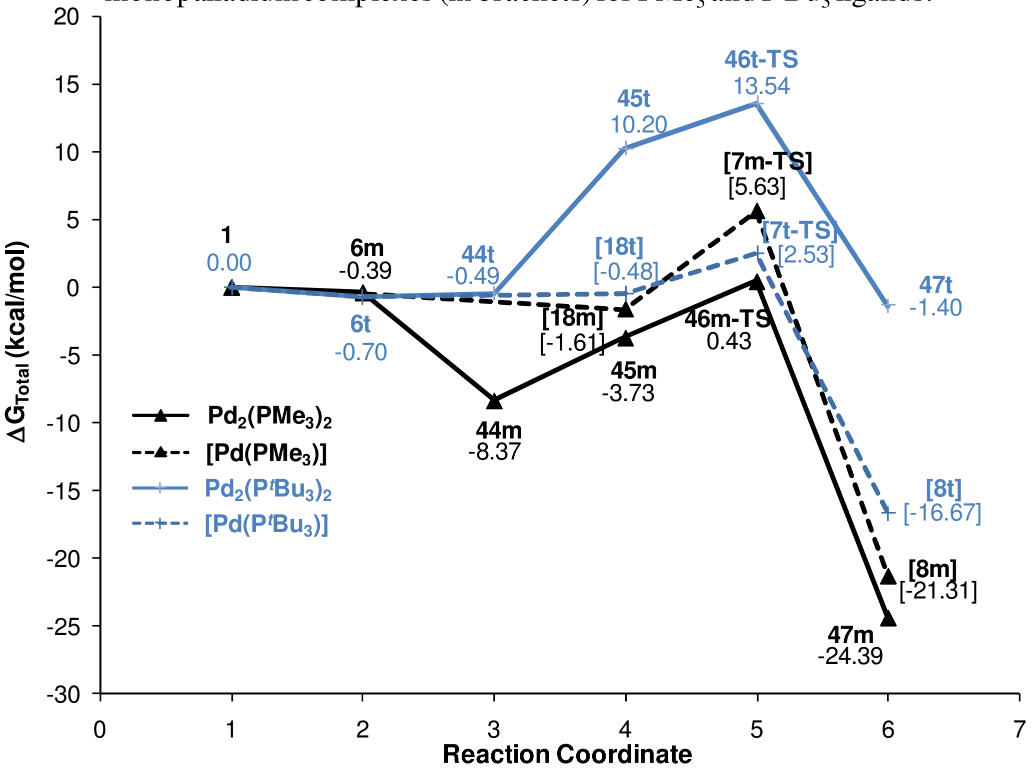

is stabilized to -8.37 kcal/mol, whereas without the semi-bridging phosphine, structure **44t** is only stabilized to -0.49 kcal/mol (Table 4.2 and Scheme 4.1).

4.3.2 The oxidative addition to dipalladium, $Pd_2(PR_3)_2$

In the formation of the π-bound complex, $Pd_2(PR_3)_2(\eta^2\text{-}PhBr)$ **45**, both phosphines migrate to one palladium while the other palladium forms the π interaction with the phenyl bromide. The energies are -3.73 and 10.20 kcal/mol for PMe_3 (**45m**) and P^tBu_3 (**45t**), respectively (Table 4.2 and Scheme 4.1). The much higher energy for P^tBu_3 in comparison to PMe_3 arises from the steric interaction leading to weaker Pd-Pd and Pd-P bonds; the Pd-Pd and Pd-P bond distances are 0.12 Å and 0.06 Å longer in **45t** than in **45m**. Then, the oxidative addition proceeds through transition state **46-TS**. In **46-TS**, the phenyl ring twists about the Pd(1)-C(11) bond to avoid steric interactions with the phosphines; the dihedral angles P(1)-Pd(2)-Pd(1)-C(11) are 17.1° and 58.2° for **46m-TS** and **46t-TS**, respectively. The energy barriers relative to the π-complex **45m** and **45t** are similar for **46m-TS** and **46t-TS**, 4.16 and 3.34 kcal/mol, respectively. Therefore, the main contributions to the difference in overall reaction barrier at **46-TS** for different phosphines are from (i) the dimerization of monopalladium monophosphine and (ii) the rearrangement of the phosphine ligands to be on the same palladium center to open the other palladium for coordination with phenyl bromide. Finally, the reaction coordinate leads from **46-TS** to the stable intermediate $Pd_2(PR_3)_2(Ph)(Br)$ **47** with energies of -24.39 and -1.40 kcal/mol for **47m** and **47t**, respectively. The phenyl ring is twisted further in these intermediates as the P(1)-Pd(2)-Pd(1)-C(11) dihedral angles have increased to 68.3° and 82.7°, respectively.

In our previous study of monopalladium with various ligands, the palladium monophosphine provided the lowest pathway to phenyl bromide oxidative addition.[152] The energies for mono- and dipalladium complex are compared in Table 4.2 and Scheme 4.1. For monopalladium monophosphine, the better σ-donor ligand (P^tBu_3 vs. PMe_3) produces a lower barrier for the oxidative addition transition state (**7-TS**) relative to the phenyl bromide π-complex (**18**), 7.24 and 3.01 kcal/mol for **7m-TS** and **7t-TS**, respectively. For dipalladium diphosphine, in contrast, the energy barriers of transition state (**46-TS**) relative to the π-complex (**45**) are similar for **46m-TS** and **46t-TS**, 4.16 and 3.34 kcal/mol, respectively. In the dipalladium complex, the neighboring $Pd(PMe_3)_2$ served as a ligand to the active palladium and as a better σ-donor than PMe_3 alone produces a lower barrier. The steric effect of the phosphine substituents is also important for the energy of the transition state. The steric hindrance of P^tBu_3 causes more difficulty in the formation of dipalladium diphosphine and its π-complex, the main contribution to the free energy of the oxidative addition transition state (**46-TS**). For the small phosphine ligand, PMe_3, the monopalladium transition state (**7m-TS**) is 5.20 kcal/mol higher than the dipalladium transition state (**46m-TS**), whereas for large phosphine ligand, P^tBu_3, **7t-TS** is -11.01 kcal/mol lower than **46t-TS**. Thus, for small phosphine ligands, such as PMe_3, phenyl bromide oxidative addition can proceed not only on monopalladium monophosphine but also on dipalladium diphosphine complexes. On the other hand, for the sterically hindered phosphine ligands, such as P^tBu_3, phenyl bromide oxidative addition on monopalladium monophosphine is preferred to that on dipalladium diphosphine.

4.3.3 The oxidative addition to substrate-bound palladium

In the absence of phosphine ligands, both free Pd atoms and Pd bound to other substrate molecules, acting as supporting ligands, can initiate the oxidative addition of PhBr. The energies for the oxidative-addition of PhBr on free Pd, Pd(η^2-C_2H_4), and $PdBr^-$ are presented in Table 4.3 and Scheme 4.2 and the related structures are shown in Figure 4.2. The formation of Pd(η^2-PhBr) **41** from Pd_4 cluster causes an energy increase of 17.08 kcal/mol. Then, **41** completes the oxidative addition via **42-TS** (19.55 kcal/mol) forming Pd(Ph)(Br) **43** at -0.15 kcal/mol. The main contribution for the oxidative addition barrier on atomic Pd is derived mainly from the formation of π-bound phenyl bromide palladium complex from Pd_4.

Formation of Pd(η^2-C_2H_4) **32** from Pd_4 is more facile (3.06 kcal/mol) because of the strong π-acceptor properties of C_2H_4. The C-C bond length increases by 0.08 Å on formation of Pd(η^2-C_2H_4). The palladium in **32** forms π-bound phenyl bromide complex, Pd(η^2-C_2H_4)(η^2-PhBr) **33** (0.46 kcal/mol); then, oxidative addition via transition state **34-TS** proceeds with a low barrier (4.59 kcal/mol). In the transition state structure, the two Pd-C bonds to ethylene are not equivalent; since C(21) is nearly co-linear with the phenyl group which has a high trans-influent group, Pd-C(21) is longer than Pd-C(22) by 0.04 Å (Figure 4.2). With the formation of the T-shape intermediate

Pd(η^2-C_2H_4)(Br)(Ph) **35**, the phenyl group is now trans to the empty site and the energy decreases to -10.96 kcal/mol.

Formation of $[PdBr]^-$ **60** causes an energy increase of 19.28 kcal/mol. Then, the phenyl bromide binds to **60**, forming [Pd(Br)(η^2-PhBr)]$^-$ **61** (6.19 kcal/mol), before proceeding to the oxidative-addition transition state **62-TS** with an energy of 9.51 kcal/mol (Table 4.3 and Scheme 4.2). Following **62-TS**, the system rearranges to the intermediate [Pd(Br)(Br)(Ph)]$^-$ **63**, in which two bromides are trans to each other and

Scheme 4.2 Solvation (DMSO) corrected relative free energy (kcal/mol) profiles for the oxidative addition of phenyl bromide to substrate-bound and free palladium (Pd(η^2-C_2H_4), $PdBr^-$, and Pd).

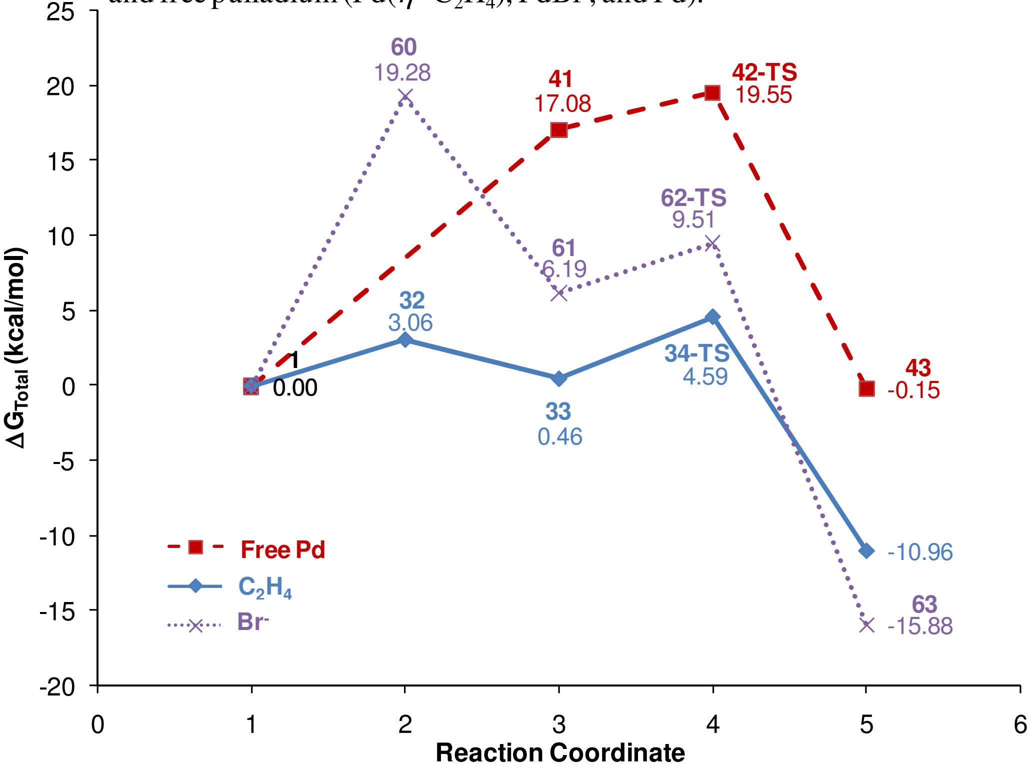

Table 4.3 Relative enthalpy and free energy for the oxidative addition to substrate-bound palladium complexes.

		ΔH	ΔG_{gas} (1 atm)	ΔG_{tot} (1 M)
C_2H_4				
1	Pd_4	0.00	0.00	0.00
32	Pd(η^2-C_2H_4)	10.07	9.12	3.06
33	InPd(η^2-C_2H_4)(η^2-PhBr)	-2.88	6.11	0.46
34-TS	TS1Pd(η^2-C_2H_4)(Br)(Ph)	0.75	10.56	4.59
35	Pd(η^2-C_2H_4)(Br)(Ph)	-12.13	-2.77	-10.96
Free Pd				
1	Pd_4	0.00	0.00	0.00
41	Pd(η_2-PhBr)	22.41	21.50	17.08
42-TS	TS1Pd(Ph)(Br)	23.86	23.49	19.55
43	Pd(Ph)(Br)	8.75	6.09	-0.15
Br^-				
1	Pd_4	0.00	0.00	0.00
60	$PdBr^-$	18.39	15.14	19.28
61	Pd(Br)(η^2-PhBr)$^-$	-16.16	-9.89	6.19
62-TS	TS1Pd(Br)(Br)(Ph)$^-$	-12.48	-6.60	9.51
63	Pd(Br)(Br)(Ph)$^-$	-41.35	-35.78	-15.88

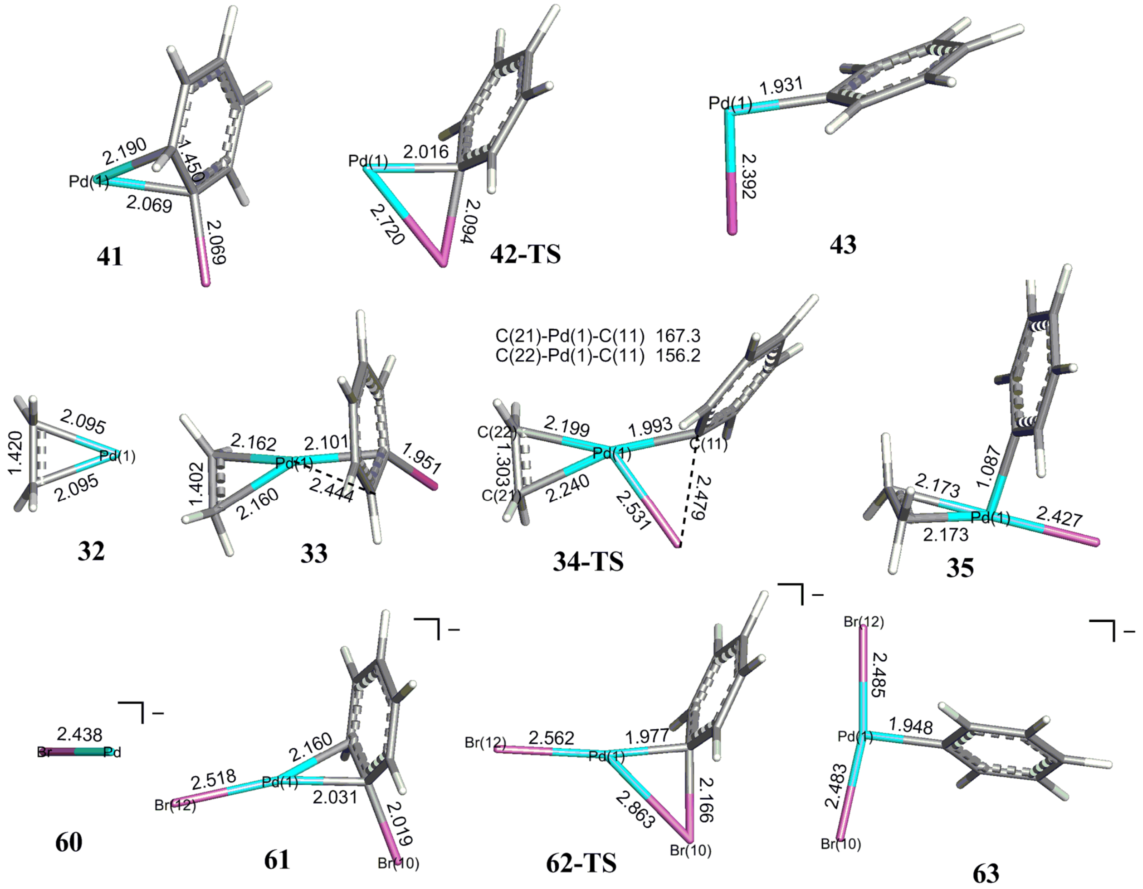

Figure 4.2 Molecular stuctures in the oxidative addition to substrate-bound palladium complex. Calculated bond distances and angles are given in Å and deg.

phenyl group is trans to the empty site; the energy decreases to -15.88 kcal/mol. Interestingly, the rate limiting step here is the formation of $PdBr^-$.

Of all of the phosphine free palladium complexes, Pd(η^2-C_2H_4) **32** is clearly preferred for phenyl bromide oxidative addition. The π-donor and π*-acceptor character of ethylene allows it to play a similar role to the phosphine in stabilizing atomic palladium. Although its transition state energy (**34-TS**) is comparable to **7m-TS**, it is still higher than **46m-TS** and **7t-TS**. Therefore, in the presence of phosphine ligands, the oxidative addition still prefers to proceed via palladium stabilized by phosphine ligand(s). However, in the absence of phosphine, the oxidative addition of phenyl bromide can proceed quite easily via ethylene supported palladium, Pd(η^2-C_2H_4) **32**.

4.3.4 The migratory insertion, β-hydride transfer/olefin elimination, and catalyst recovery of dipalladium

Because the oxidative addition step through the dipalladium diphosphine complex is unlikely for the sterically hindered P^tBu_3 ligand, we calculated the rest of the Heck reaction for the dipalladium diphosphine only for the PMe_3 ligand. The energy barrier for the phenyl bromide oxidative addition via dipalladium is lower than monopalladium complex by -5.20 kcal/mol for PMe_3 ligand. The energies for the entire Heck reaction path through $Pd_2(PMe_3)_2$ catalyst are shown and compared with the reaction path through $Pd(PMe_3)$ in Scheme 4.3 and Table 4.4.

Phenyl bromide oxidative addition produces $Pd_2(PMe_3)_2(Ph)(Br)$ **47** in which the phenyl ring twists about the Pd(1)-C(11) bond to reduce the steric interaction with the phosphines (Figure 4.1). Intermediate **47**, then, rearranges to **47b** with the neighboring palladium trans to the empty site; the Pd(1)-Pd(2) bond shortens from 2.626 Å to 2.578 Å and the Pd(1)-Br(10) bond lengthens from 2.450 Å to 2.522 Å (Figures 4.1 and 4.3). The phenyl, the highest trans-influence ligand, trans to the empty site in **47**, is now trans to the bromide ion in **47b**; therefore, the isomerization causes an energy increase from -24.39 to -21.22 kcal/mol (Table 4.4).

Scheme 4.3 Solvation (DMSO) corrected relative free energy (kcal/mol) profiles of the Heck catalytic cycle in the oxidative addition, migratory insertion, *β*-H transfer/olefin elimination, and catalyst recovery by mono- and dipalladium complexes with PMe_3.

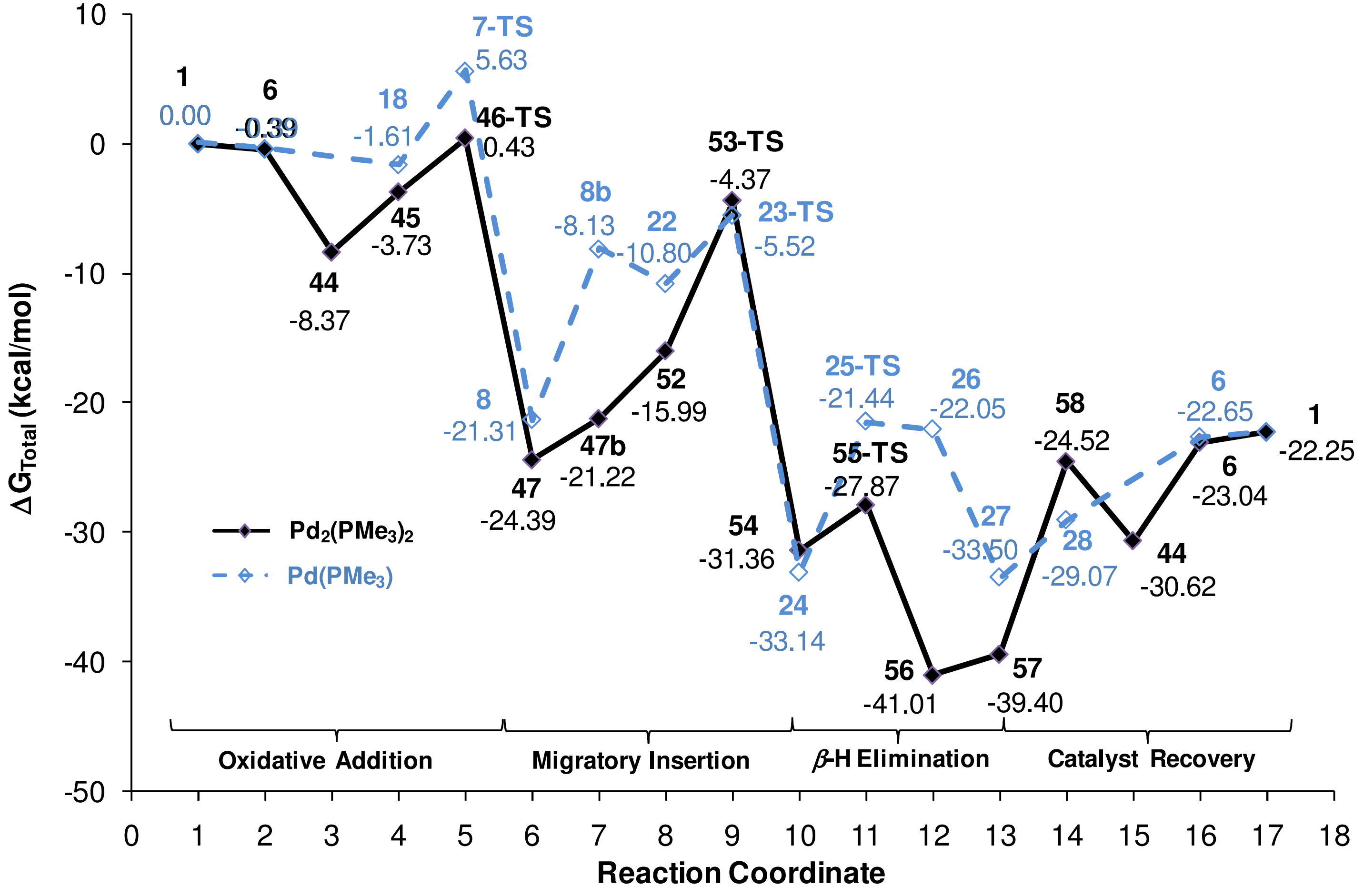

Table 4.4 Relative enthalpy and free energy for the migratory insertion, β-H transfer/ olefin elimination, and catalyst recovery for di- and monopalladium complexes.

		ΔH	ΔG_{gas} (1 atm)	ΔG_{tot} (1 M)
Dipalladium				
Migratory insertion				
47	$Pd_2(PMe_3)_2(Ph)(Br)$	-43.86	-23.36	-24.39
47b	$Pd_2(PMe_3)_2(Ph)(Br)b$	-39.61	-19.90	-21.22
52	$Pd_2(PMe_3)_2(Ph)(Br)(\eta^2\text{-}C_2H_4)$	-48.13	-16.42	-15.99
53-TS	$TS2Pd_2(PMe_3)_2(Ph)(Br)(C_2H_4)$	-37.28	-3.33	-4.37
β-H transfer/olefin elimination				
54	$Pd_2(PMe_3)_2(Br)(HC_2H_3Ph)$	-61.51	-28.88	-31.36
55-TS	$TS3Pd_2(PMe_3)_2(Br)(HC_2H_3Ph)$	-57.55	-25.02	-27.87
56	$Pd_2(PMe_3)_2(Br)(H)(C_2H_3Ph)$	-68.19	-38.10	-41.01
Catalyst recovery				
57	$Pd_2(PMe_3)_2(Br)(H)$	-50.92	-31.51	-39.40
58	$Pd_2(PMe_3)_2(Br)(H\text{--}NEt_3)$	-53.43	-21.62	-24.52
44	$Pd_2(PMe_3)_2$	67.81	81.30	-30.62
6	$Pd(PMe_3)$	84.75	88.86	-23.04
1	Pd_4	80.23	84.83	-22.25
Monopalladium				
Migratory insertion				
8	$Pd(PMe_3)(Br)(Ph)$	-25.87	-16.05	-21.31
8b	$Pd(PMe_3)(Br)(Ph)b$	-14.51	-5.86	-8.13
22	$Pd(PMe_3)(Br)(Ph)(\eta^2\text{-}C_2H_4)$	-25.04	-3.76	-10.80
23-TS	$TS2Pd(PMe_3)(Br)(Ph)(C_2H_4)$	-20.13	1.97	-5.52
β-H transfer/olefin elimination				
24	$Pd(PMe_3)(Br)(HC_2H_3Ph)$	-47.84	-25.87	-33.14
25-TS	$TS3Pd(PMe_3)(Br)(HC_2H_3Ph)$	-36.97	-14.26	-21.44
26	$Pd(PMe_3)(Br)(H)(C_2H_3Ph)$	-36.58	-15.45	-22.05
Catalyst recovery				
27	$Pd(PMe_3)(Br)(H)$	-34.53	-25.88	-33.50
28	$Pd(PMe_3)(Br)(H\text{--}NEt_3)$	-43.21	-20.40	-29.07
6	$Pd(PMe_3)$	82.49	86.84	-22.65
1	Pd_4	80.23	84.83	-22.25

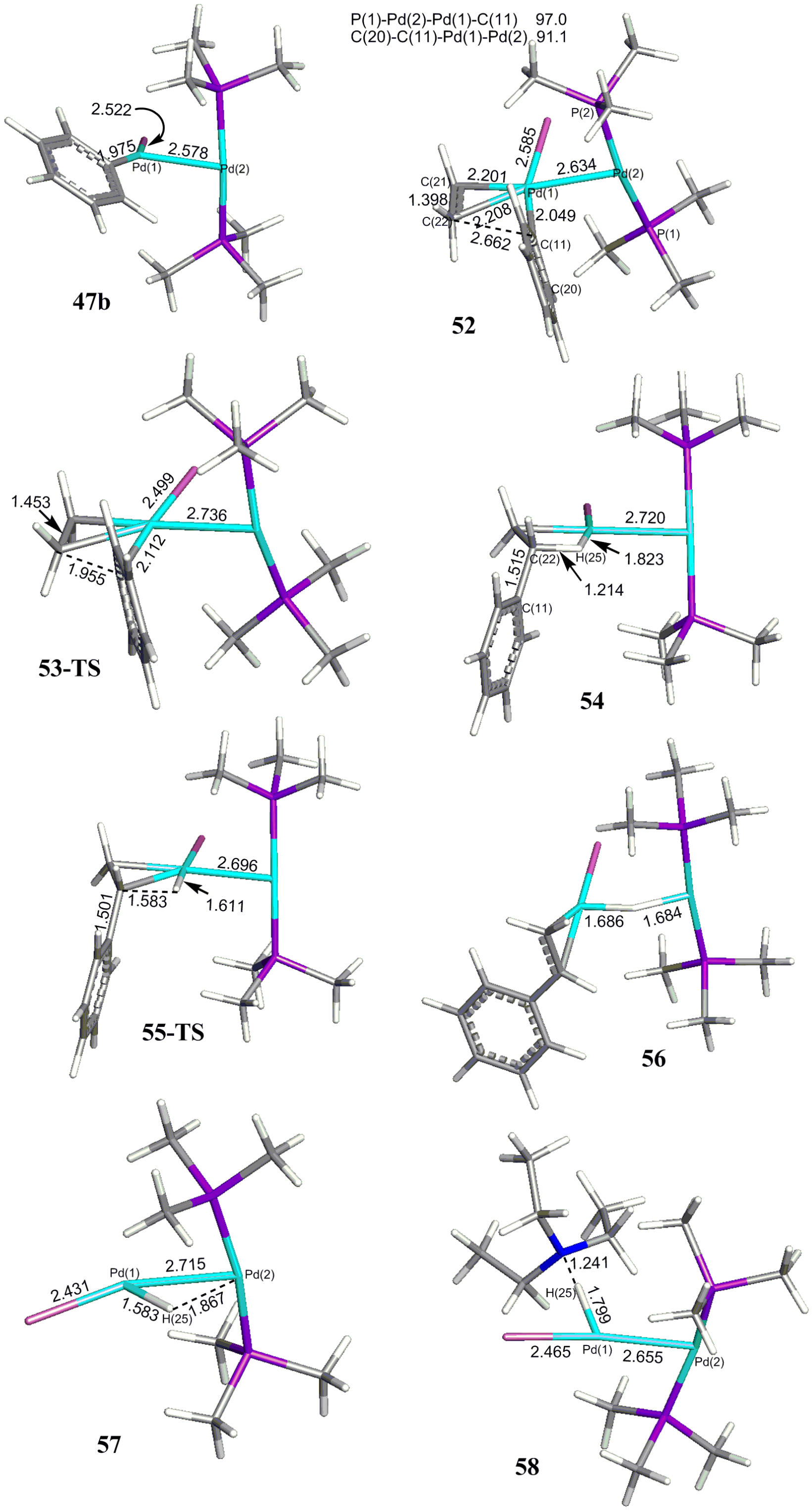

Figure 4.3 Molecular stuctures in the migratory insertion, β-H transfer/olefin elimination, and catalyst recovery of dipalladium complex with PMe_3 ligand. Calculated bond distances and angles are given in Å and deg.

Ethylene now binds at the empty site cis to the phenyl group to form $Pd_2(PMe_3)_2(Ph)(Br)(C_2H_4)$ **52**. The active Pd is in a nearly square planar environment with both ethylene carbons lying parallel to the coordination plane and perpendicular to P(1)-Pd(2)-P(2) plane. The ethylene binding causes an energy increases to -15.99 kcal/mol. Then, **52** proceeds to the migratory insertion via **53-TS**. The phenyl group in **53-TS** bends back toward phosphine substituents on the neighbor palladium. To reduce steric interaction, Pd(1)-Pd(2) bond is lengthened further by 0.10 Å; the energy increases to -4.37 kcal/mol. In completing this step, the phenyl group migrates to the nearest ethylene C(22) and then moves away from the Pd, which leaves a C-H agostic bond interaction to palladium where the phenyl was previously attached.

From the intermediate formed, $Pd_2(PMe_3)_2(Br)(HCH_2CHPh)$ **54** (-31.36 kcal/mol), the agostic β-hydrogen H(25) transfers from C(22) to palladium via **55-TS**, increasing an energy to -27.87 kcal/mol. Relative to **54**, the Pd(1)-H(25) bond is shortened by 0.21 Å and the C(22)-H(25) bond is lengthened by 0.37 Å in **55-TS**. The intermediate product **56** is formed at -41.01 kcal/mol, and the hydrogen H(25) atom is found bridging equally between the two palladium (Pd-H ~ 1.68 Å) and the Pd(1)-Pd(2) bond lengthens to 3.17 Å. In **56**, the styrene group is bound trans to bromide and the C(21)-C(22) bond is perpendicular to the coordination plane. Then, the dissociation of the styrene product is slightly endergonic relative to **56** (1.61 kcal/mol) and leads to $Pd_2(PMe_3)_2(Br)(H)$ **57**. The hydrogen atom becomes semi-bridging between two palladium atoms; the Pd(1)-H(25) and Pd(2)-H(25) bond distances are 1.583 Å and 1.867 Å, respectively, and the Pd(1)-Pd(2) bond shortens to 2.715 Å.

To recover the active catalyst, the base NEt_3 abstracts the proton and forms $Pd_2(PMe_3)_2(Br)(H\text{--}NEt_3)$ **58** (-24.52 kcal/mol). Now, the hydrogen H(25) is bound in between N and Pd(1) and the Pd(1)-Pd(2) bond shortens further to 2.655 Å. Elimination of $HNEt_3^+$ and Br^- and the formation of $Pd_2(PMe_3)_2$ **44** reduces the energy to -30.62 kcal/mol. This active catalyst can start the catalytic reaction again or the complete cycle leads back to Pd_4 and phosphine losses with an energy of -22.25 kcal/mol.

The free energy profiles of the Heck reaction through $Pd(PMe_3)$ and $Pd_2(PMe_3)_2$ are compared in Scheme 4.3; the structures of all species related to the pathway of $Pd(PMe_3)$[152] are shown in Chapter III. Since the energies of the species along the reaction coordinate involving $Pd_2(PMe_3)_2$ are similar or lower than those involving $PdPMe_3$, dipalladium complexes could easily be involved in the Heck catalytic cycle with small phosphines or even other small supporting ligands.

4.3.5 The migratory insertion, *β*-hydride transfer/olefin elimination, and catalyst recovery of substrated-bound palladium

4.3.5.1 Ethylene-bound palladium complex

In the absence of phosphine, ethylene bound Pd can provide a low energy oxidative-addition barrier. The intermediate **35** rearranges to place the ethylene parallel to the coordination plane and the phenyl group trans to the bromide ion (Figure 4.2 and

Figure 4.4); the energy increases from -10.96 (**35**) to -2.18 kcal/mol (**35b**) (Scheme 4.4 and Table 4.5). Then, the migratory insertion proceeds through transition state **36-TS**, in which the C(11)-C(22) bond between phenyl and ethylene is shortened by 0.48 Å and the C(21)-C(22) bond of ethylene is lengthened by 0.03 Å; energy slightly increases to 1.19 kcal/mol. The intermediate formed (**37**) has C(11)-C(22) and C(21)-C(22) single bonds and an agostic C-H bond to Pd (Pd(1)-H(25), 1.827 Å and C(22)-H(25), 1.198 Å), at an energy of -17.41 kcal/mol.

The β-H transfer/olefin elimination proceeds through transition state **38-TS** with an energy increase to -9.16 kcal/mol. The Pd(1)-H(25) bond distance shortens to 1.556 Å and C(22)-H(25) bond distance lengthens to 1.651 Å. Then, the reaction continues to the intermediate Pd(Br)(H)(C_2H_3Ph) **39** (-20.14 kcal/mol), in which C(21)-C(22) bond of styrene lies perpendicular to the Br(10)-Pd(1)-H(25) plane opposite the bromide ion, while hydrogen H(25) is cis to bromide ion. Because the products of styrene dissociation, Pd(Br)(H) **40** has no π-acceptor ligands to stabilize the palladium atom, the dissociation free energy of styrene is endergonic by 16.59 kcal/mol relative to **39**. Following styrene loss, the base NEt_3 abstracts the proton H(25) and forms Pd(Br)(H--NEt_3) **59**, which releases $HNEt_3^+$ and Br^-; the formation of the Pd_4 cluster completes the cycle.

Scheme 4.4 Solvation (DMSO) corrected relative free energy (kcal/mol) profiles of the Heck catalytic cycle in the oxidative addition, migratory insertion, *β*-H transfer/olefin elimination, and catalyst recovery by substrate-bound palladium complexes.

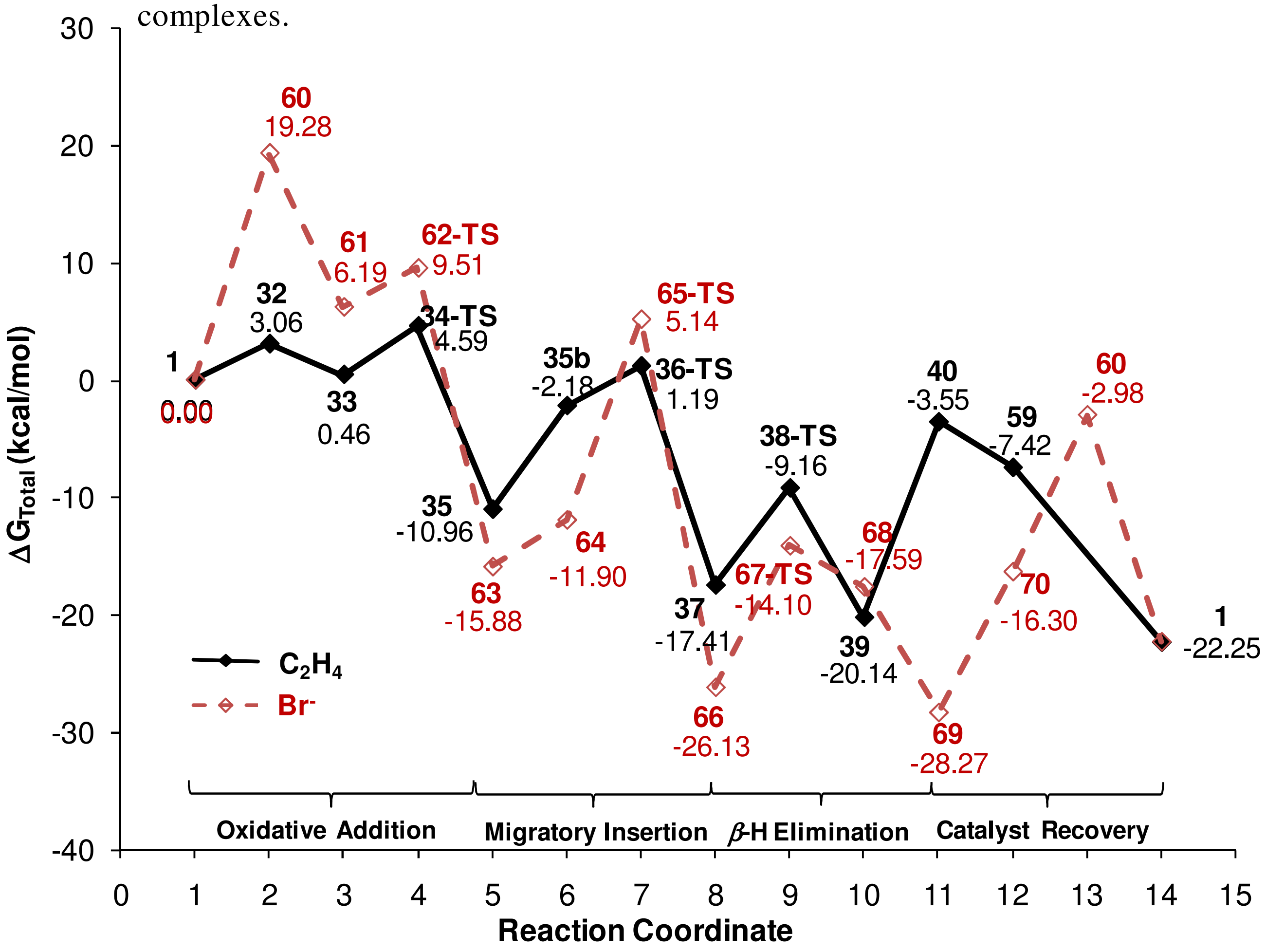

Table 4.5 Relative enthalpy and free energy for the migratory insertion, β-H transfer/ olefin elimination, and catalyst recovery for substrate-bound palladium complexes.

		ΔH	ΔG_{gas} (1 atm)	ΔG_{tot} (1 M)
C_2H_4				
Migratory insertion				
35	$Pd(\eta^2\text{-}C_2H_4)(Br)(Ph)$	-12.13	-2.77	-10.96
35b	$Pd(\eta^2\text{-}C_2H_4)(Br)(Ph)b$	-1.97	6.25	-2.18
36-TS	$TS2Pd(\eta^2\text{-}C_2H_4)(Br)(Ph)$	0.67	11.22	1.19
β-H transfer/olefin elimination				
37	$Pd(Br)(HC_2H_3Ph)$	-17.50	-7.58	-17.41
38-TS	$TS3Pd(Br)(HC_2H_3Ph)$	-9.24	0.17	-9.16
39	$Pd(Br)(H)(C_2H_3Ph)$	-21.27	-11.85	-20.14
Catalyst recovery				
40	$Pd(Br)(H)$	7.36	5.08	-3.55
59	$Pd(Br)(H\text{--}NEt_3)$	-6.08	4.79	-7.42
1	Pd_4	80.23	84.83	-22.25
Br^-				
Migratory insertion				
63	$Pd(Br)(Br)(Ph)^-$	-41.35	-35.78	-15.88
64	$Pd(Br)(Br)(Ph)(\eta^2\text{-}C_2H_4)^-$	-44.35	-27.03	-11.90
65-TS	$TS2Pd(Br)(Br)(Ph)(C_2H_4)^-$	-22.92	-5.07	5.14
β-H transfer/olefin elimination				
66	$InPd(Br)(Br)(HC_2H_3Ph)^-$	-61.43	-44.30	-26.13
67-TS	$TS3Pd(Br)(Br)(HC_2H_3Ph)^-$	-43.48	-25.73	-14.10
68	$Pd(Br)(Br)(H)(C_2H_3Ph)^-$	-49.13	-31.42	-17.59
Catalyst recovery				
69	$Pd(Br)(Br)(H)^-$	-48.19	-43.18	-28.27
70	$Pd(Br)(Br)(H\text{--}NEt_3)^-$	-47.66	-30.79	-16.30
60	$PdBr^-$	98.63	99.96	-2.98
1	Pd_4	80.23	84.83	-22.25

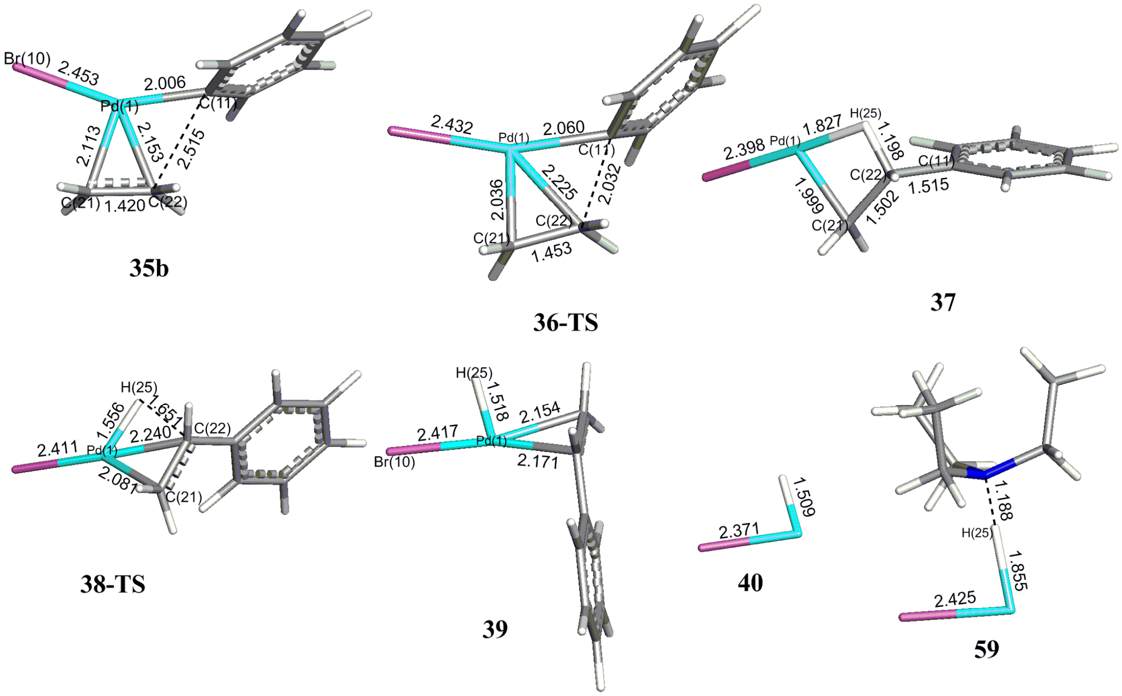

Figure 4.4 Molecular stuctures in the migratory insertion, β-H transfer/olefin elimination, and catalyst recovery of ethylene-bound palladium complex. Calculated bond distances and angles are given in Å and deg.

4.3.5.2 Bromide-bound palladium complex

Based on experimental evidence, de Vries proposed a mechanism in which the halide anion stabilizes atomic palladium and serves as a ligand for palladium catalyst in "ligand-free" Heck reaction cycle.[26] Although the bromide ion can serve as a spectator ligand like phosphine, it is a π-donor, not a π-acceptor. Because of this lack of π-backbonding, Br^- is not as effective in stabilizing a Pd atom and the energy of $PdBr^-$ is relatively high in comparison to Pd(η^2-C_2H_4) and $PdPR_3$.

After the oxidative addition step, $[Pd(Br)(Br)(Ph)]^-$ (**63**) binds ethylene and forms $[Pd(Br)(Br)(Ph)(C_2H_4)]^-$ (**64**) with a small energy increase from -15.88 (**63**) to -11.90

(**64**) kcal/mol (Scheme 4.4 and Table 4.5). The lowest energy isomer has ethylene perpendicular to the coordination plane and cis to the phenyl group (Figure 4.5); no minimum were found for an isomer with ethylene lying in the coordination plane.

Migratory insertion through transition state **65-TS** causes an energy increase to 5.14 kcal/mol. The higher energy barrier for the migratory insertion for **64** compared to that for Pd(Br)(Ph)(C_2H_4) (**35b**) arises because the ethylene in **35b** is already parallel to the coordination plane. Formation of the intermediate $[Pd(Br)(Br)(HC_2H_3Ph)]^-$ **66** proceeds with an energy of -26.13 kcal/mol. Interestingly, there is no agostic C-H bond interaction to palladium in the intermediate **66** unlike the corresponding one with phosphine ligand or ethylene as the supporting ligand.

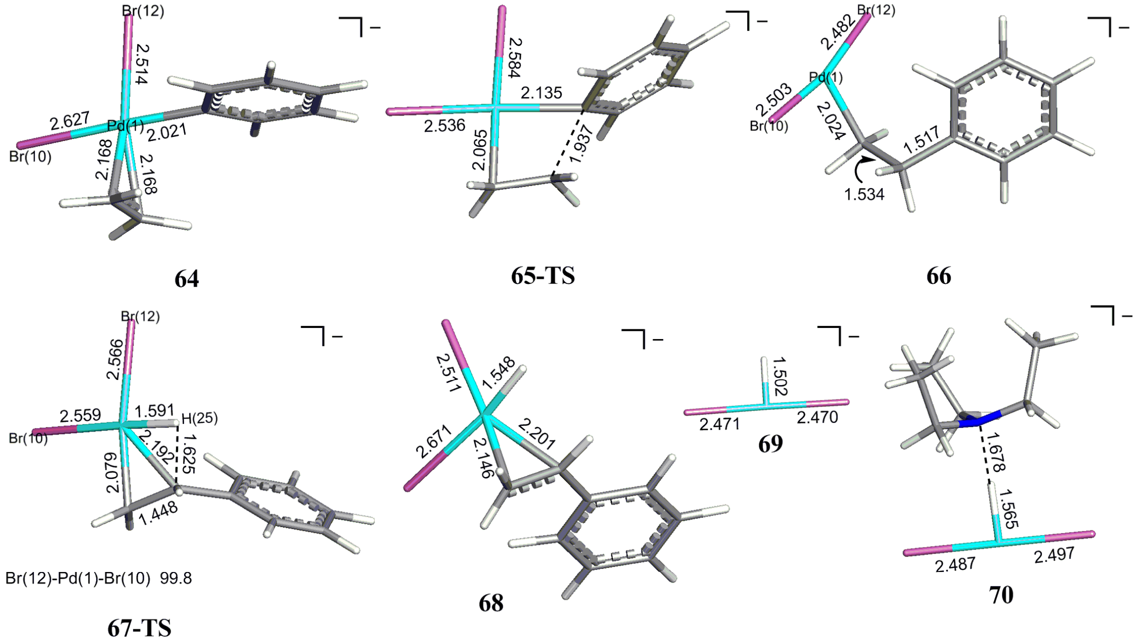

Figure 4.5 Molecular stuctures in the migratory insertion, β-H transfer/olefin elimination, andcatalyst recovery of palladium with bromide ion complex. Calculated bond distances and angles are given in Å and deg.

Then, the hydrogen H(25) transfers to palladium via the transition state **67-TS** (-14.10 kcal/mol) and forms intermediate $[Pd(Br)(Br)(H)(C_2H_3Ph)]^-$ **68** (-17.59 kcal/mol). The two Pd-Br bonds are in a cis position and the Pd(1)-H(25) bond distance is shortened to 1.548 Å. Finally, the styrene dissociation to form $[Pd(Br)(Br)(H)]^-$ **69** is exergonic by -10.68 kcal/mol relative to **68**. The two Pd-Br bonds rearrange to be trans to each other and Pd(1)-H(25) bond distance shortens further to 1.502 Å. Again, the NEt_3 base abstracts the proton, forms intermediate $[Pd(Br)(Br)(H\text{--}NEt_3)]^-$ **70** which can either loses $HNEt_3^+$ and all Br^- ions or transiently forms $PdBr^-$, then loses Br^- and forms Pd_4 to complete catalytic cycle.

4.3.5.3 Probable pathway for substrate-bound palladium

The free energy profiles for the complete pathways of the Heck reaction with substrate-bound (C_2H_4 and Br^-) palladium catalyst are compared in Scheme 4.4. Although de Vries[26] proposed a mechanism for "ligand free" Heck reaction, in which halide ion(s) stabilize the atomic palladium and act(s) as a ligand in the Heck catalytic cycle, our results show that the ethylene substrate is a better ligand than bromide ion to stabilize atomic palladium and abstract it from a palladium cluster. Moreover, $Pd(\eta^2\text{-}C_2H_2)$ leads to lower energy barriers than $PdBr^-$ for the oxidative addition and migratory insertion steps (**34-TS** to **62-TS** and **36-TS** to **65-TS**). However, after the C-C bond formation, the β-H transfer/olefin elimination has a lower barrier for the $PdBr^-$ complex (**38-TS** to **67-TS**). In fact, the two pathways can intercross by the association and dissociation of bromide ion. Therefore, the most probable pathway for the so-called "ligand free" Heck reaction (Scheme 4.5) begins with the ethylene stabilizing palladium and abstracting Pd atoms from nanoclusters. Then, phenyl bromide binds and the reaction proceeds through the oxidative addition and migratory insertion. Next the bromide ion binds to Pd(Br)(HC_2H_3Ph) **37** to stabilize this low-coordinated palladium complex and forms [Pd(Br)(Br)(HC_2H_3Ph)]$^-$ **66** before proceeding with the rest of the reaction. Note that a second ethylene could also take the place of second bromide, to stabilize the low-coordinated palladium **37**.

Scheme 4.5 The probable mechanism of the "ligand-free" Heck Reaction.

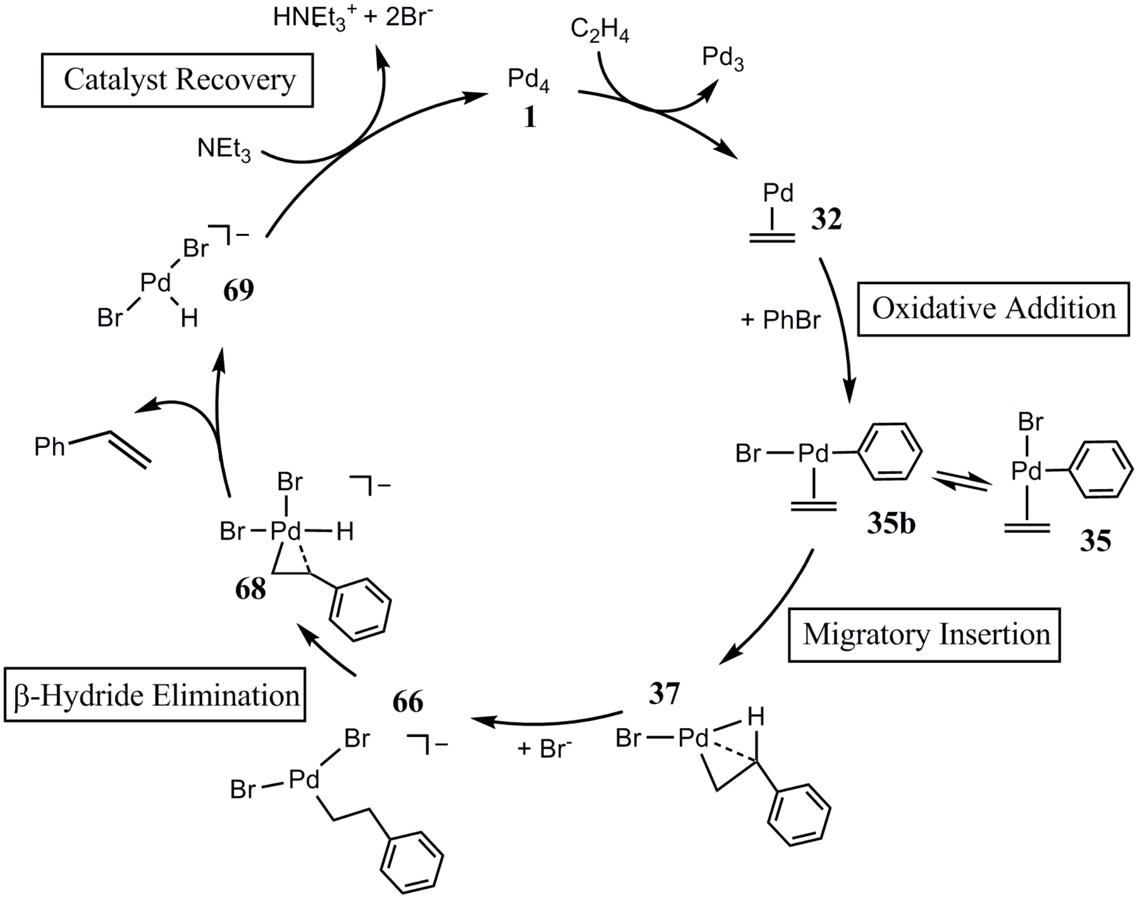

4.4 Conclusions

Both phosphine and ethylene can stabilize atomic palladium dissociated from the model nanocluster Pd_4. Under conditions with phosphine ligands, monopalladium monophosphine not only plays a role as an active catalyst, it can also dimerize to form dipalladium diphosphine (other monopalladium complexes might also undergo this reaction). For large sterically demanding phosphines, such as P^tBu_3, the phenyl bromide oxidative-addition barrier is lower on monopalladium monophosphine. On the other hand, for the small phosphine ligand, such as PMe_3 and possibly sterically less demanding phosphines not studied here, the phenyl bromide oxidative addition can proceed more easily via dipalladium diphosphine. Thus, the dipalladium complexes may lead to higher activity and lower energy barriers relative to monopalladium monophosphine. Our results confirm that pathways containing dipalladium species can form viable alternative Heck reaction pathways.

In the absence of phosphine ligand, the substrate-bound palladium complexes were investigated as the potential intermediates for the Heck reaction. The phenyl bromide oxidative addition on $Pd(\eta^2\text{-}C_2H_4)$ has the lowest energy barrier in comparison to $PdBr^-$ and bare Pd. Our study concludes that at the beginning of the Heck reaction, the ethylene but not Br^- stabilizes atomic palladium well enough to remove an atom from a palladium cluster. Then, phenyl bromide binds, undergoes oxidative addition, and migratory insertion. After C-C bond coupling, the binding of an additional bromide ion to low-coordinated $Pd(Br)(HC_2H_3Ph)$ **37** complex creates a more stable intermediate $[Pd(Br)(Br)(HC_2H_3Ph)]^-$ **66** which proceeds through the β-hydride transfer/olefin elimination and catalyst recovery steps over lower barriers. Thus, under phosphine free conditions, our study reveals additional supporting roles for both ethylene and bromide ion in the Heck reaction. Ethylene acts best as a ligand to stabilize palladium through the oxidative addition and migratory insertion steps; then the additional ligand, such as a second bromide or perhaps a second ethylene, ligates to the open site to stabilize the low-coordinated palladium complex before releasing the styrene product and recovering the active palladium catalyst.

CHAPTER V

DENSITY FUNCTIONAL STUDY OF THE FACTORS AFFECTING THE PRODUCTS FORMED BY CYTOCHROME P450 AND SUPEROXIDE REDUCTASE: INTERMEDIATE SPIN STATES AND HYDROGEN BONDS FROM WATER SOLVENT MOLECULES

5.1 Introduction

The active sites of both superoxide reductase (SOR) and cytochrome P450 monooxygenase enzymes have the same first coordination sphere containing an iron center coordinated by four nitrogen donor atoms and one cysteinate sulfur in a square pyramidal arrangement (Fe[N_4S] center). However, these enzymes catalyze very different reactions.[161-163] Superoxide reductase is a non-heme iron enzyme for detoxification of superoxide in anaerobic organisms.[164-166] The histidine and cysteine ligated iron active site of SOR binds superoxide, catalyzes one-electron reduction and produces hydrogen peroxide (i.e. $O_2^- + 2H^+ + e^- \rightarrow H_2O_2$). The cytochrome P450 monooxygenase is a heme-iron enzyme for biosynthesis of steroids, detoxification of xenobiotics, and metabolism of drugs.[36,167] The porphyrin and cysteine ligated iron active site of P450 binds O_2, catalyzes two-electron reduction and double protonation of O_2 to cleave the O-O bond and yield a high valent iron-oxo complex (and one equivalent of H_2O) that catalyzes the stereospecific alkane hydroxylation reaction.

The generally accepted catalytic mechanisms for P450[36,167] and SOR[168-170] are compared in Scheme 5.1. In both SOR and P450 mechanisms, after one electron reduction of ferric (Fe^{III}) resting state, a dioxygen species (O_2^- and O_2 respectively) binds to a ferrous (Fe^{II}) center with the addition of one electron to the latter giving a ferric peroxo (Fe^{III}-OO) intermediate. Protonation of the distal oxygen (terminal oxygen), O_d, yields a ferric hydroperoxo (Fe^{III}-OOH) species, a common intermediate in both enzymes.[161] However, this common intermediate proceeds through two very different reactions. A second protonation on the proximal oxygen (iron-bound oxygen), O_p, leads to the formation and release of hydrogen peroxide (HOOH), the product of SOR. The production of hydrogen peroxide is also a side-reaction for P450 (also known as an uncoupling or decoupling reaction since it wastes reducing equivalents and O_2).[171] On the other hand the productive reaction in P450 involves a second protonation on the distal oxygen that leads to loss of H_2O and formation of an oxo-ferryl (Fe^{IV}=O) species known as Compound I (Cpd I).

Scheme 5.1 Catalytic cycle of SOR and P450.

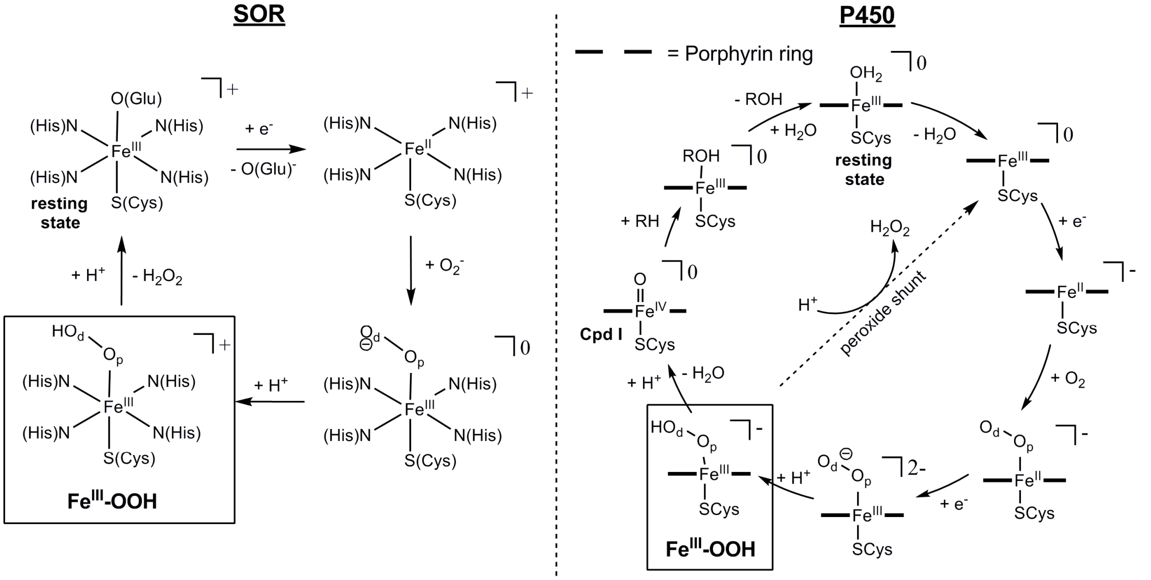

The SOR and P450 enzymes also differ significantly in the location of the enzyme active sites within their respective proteins. The P450 enzyme active site is located inside an enclosed pocket that is buried in the protein. Well-defined O_2 and alkane access channels, which also serve as H_2O and product egress channels, connect the P450 enzyme active site to the protein surface.[35] Similarly, well-defined hydrogen-bonded proton-transfer pathways deliver protons from the protein surface to the P450 enzyme active site.[35,37] In marked constrast, the active site of SOR is located in a cavity on the surface of the SOR enzyme that is fully exposed to solvent water molecules.[32,169]

Recent computational studies have provided new insights into the formation of oxo-ferryl complex in P450 and the production of hydrogen peroxide in SOR. The protonation of Fe^{III}-OOH at the distal oxygen is found more favorable than the protonation at the proximal oxygen from several theoretical studies of P450 models.[172-174] Later DFT and QM/MM studies also showed that the water network shuttles the proton from nearby amino acid residues to protonate the distal oxygen of Fe^{III}-OOH in P450 model.[175-178] For SOR model, the formation of hydrogen peroxide was investigated. Kurtz and coworkers performed density functional calculation on various mono- and di-protonated peroxo ferric complexes and found that the protonation at the proximal oxygen is an important step to the decay of Fe^{III}-OOH and release of hydrogen peroxide.[179]

Relatively few computational and spectroscopic studies were done for the structures and reactivity for the intermediates in SOR active site in comparison to the corresponding ones in P450 active site.[180,181] Yang et al. studied the electronic properties of cyano-ferric intermediates for both enzymes by ENDOR measurements complemented with DFT calculation and found that the difference in the in-plane heme and out-of-plane dihedral of four histidines and the inclusion of H-bonds to the cysteine axial ligands cause different spin density distribution on sulfur in the active sites.[180] Solomon and coworkers suggested that the strong equatorial ligand field from porphyrin results in a low-spin Fe^{III}-OOH, which will not support the H_2O_2 release because of the spin-crossing barrier in the formation of high-spin ferric pentacoordinate product; in contrast, the dianionic porphyrin could assist the formation of oxo-ferryl complex.[181] In addition to these studies, we believe that not only the equatorial ligand field but the nature of the equatorial ligand structures that form Fe-N bonds could also cause different ground spin states of Fe^{III}-OOH. The Fe^{III}-OOH structures in all possible spin states for SOR and P450 models need to be examined closely to explain why high-spin structure supports Fe-O bond cleavage in SOR and low-spin structure supports O-O bond cleavage in P450. Moreover, the effect from the difference in the iron active site location in these two enzymes should be investigated.

Therefore a careful comparison of both reactions in both active sites is presented in detail here. To understand the factors leading to the difference in the reaction pathways between these two similar active site enzymes, the structural properties of the corresponding intermediates from both enzymes should be compared, as well as the inclusion of the effect from different active site locations, which have not been addressed elsewhere yet. Here, we used density functional calculation to study the geometric parameters, electronic structures, and relative free energies of all possible spin states for the model of ferric hydroperoxo, $(SCH_3)(L)Fe^{III}$-OOH (L = four imidazoles for SOR and porphyrin for P450), the common intermediate of SOR and P450, to examine the factors leading to different mechanisms for both enzyme models. Then, the formation of ferric hydrogen peroxide, $(SCH_3)(L)Fe^{III}$-HOOH, complex is compared to the formation of oxo-ferryl, $(SCH_3)(L)Fe^{IV}=O$, complex for both enzyme active site models. Finally, we also studied the effect from the solvent-exposed position of the active site in SOR enzymes to the production of hydrogen peroxide by including the explicit water molecules in the calculation of $(SCH_3)(L)Fe^{III}$-HOOH intermediate.

5.2 Computational details

In both iron active site models for SOR and P450, a methyl thiolate (SCH_3^-) is used as the axial ligand. At the equatorial ligands, in SOR four histidines are replaced by four neutral imidazole (ImH) ligands (Scheme 5.2) and in P450 heme was replaced by porphyrin (Por) (Scheme 5.3). For all SOR models, the crystal structure in the resting ferric state with glutamate bound at the sixth-coordinate (PDB code: 1DQI)[32] was used as the starting structure. The sixth-coordinate ligand was replaced by acetate (CH_3COO^- or OAc^-) in the model of glutamate-bound resting state, $[(SCH_3)(ImH)_4Fe^{III}\text{-OAc}]^+$, and by hydroperoxo ($OOH^-$), hydrogen peroxide (HOOH), and oxo (O^{2-}) in the models of ferric hydroperoxo $[(SCH_3)(ImH)_4Fe^{III}\text{-OOH}]^+$, ferric hydrogen peroxide $[(SCH_3)(ImH)_4Fe^{III}\text{-}HOOH]^{2+}$, and oxo-ferryl $[(SCH_3)(ImH)_4Fe^{IV}{=}O]^{2+}$ complexes, respectively. For all P450, the crystal structure

Scheme 5.2 The $[(SCH_3)(ImH)_4Fe^{III}\text{-}OAc]^{+}$ model for SOR active site. The residue numbers showed in parenthesis is from the crystal structure of *Pyrococcus furiosus* SOR structure (PDB code: 1DQI).

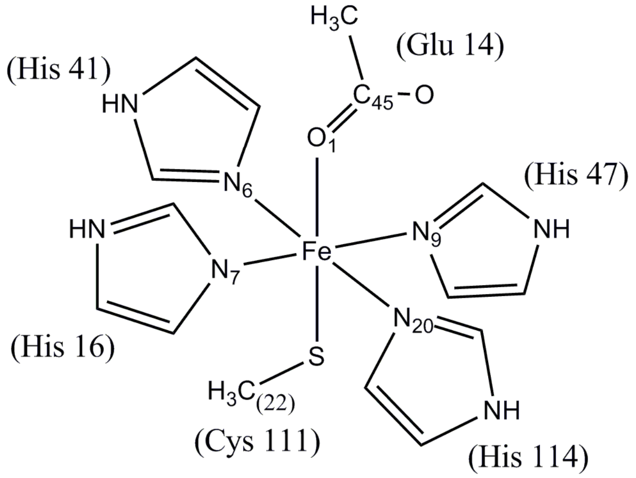

Scheme 5.3 The $(SCH_3)(Por)Fe^{III}\text{-}X$ model for P450 active site. ($X = OOH^-$, HOOH, and O^{2-})

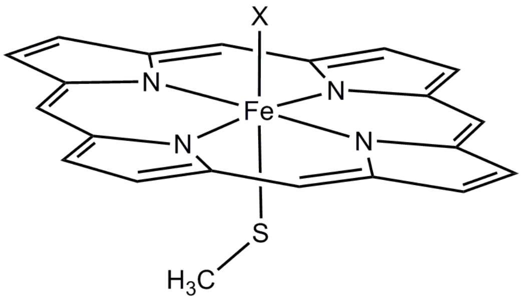

of cytochrome P450 from PDB code: 1DZ8[35] was used as the starting structure. Like SOR models, the sixth-coordinate was replaced by hydroperoxo, hydrogen peroxide, and oxo in the model of $[(SCH_3)(Por)Fe^{III}\text{-}OOH]^-$, $[(SCH_3)(Por)Fe^{III}\text{-}HOOH]^0$, and $[(SCH_3)(Por)Fe^{IV}{=}O]^0$ complexes, respectively.

All calculations were performed with the Gaussian03 program package.[132] The PBE[73] density functional was used for all geometry optimization with basis set I (BS-I), in which modified LANL2DZ+f basis set with effective core potentials (ECP)[133-135] is used for Fe; 6-31++G(d,p)[136-138] is used for sulfur, iron-bound nitrogen, and oxygen and hydrogen atoms of H_2O and H_2O_2; and 6-31G(d)[136-138] is used for all other atoms. Only the geometry optimization of $[(SCH_3)(ImH)_4Fe^{III}\text{-}OAc]^+$ in SOR model used both basis set I and II; in BS-II, 6-31++G(d,p) is used for iron while the rest is identical to BS-I. All structures were fully optimized and frequency calculations were calculated to ensure that there are no imaginary frequencies for minima. Frequency calculations were performed with the PBE functional and single point energies were recalculated with the B3LYP functional[140,141] under the same basis set. Zero point energies and thermodynamic functions were calculated at 298.15 K and 1 atm.

5.3 Results and discussion

We begin with the density functional calculation of $[(SCH_3)(ImH)_4Fe^{III}\text{-}OAc]^+$, the model for ferric resting state of SOR, to compare geometry parameters and ground spin state with the one from the crystal structure (PDB: 1DQI and 1DO6)[32] and spin state from the experiment.[182] Then, the electronic structures of all possible spin states for ferric hydroperoxo model, $(SCH_3)(L)Fe^{III}$-OOH, a common intermediate of SOR (L = ImH_4) and P450 (L = Por), will be examined for the factors causing different pathways in each enzyme. The protonation at distal oxygen of $(SCH_3)(L)Fe^{III}$-OOH leads to O-O bond cleavage and $(SCH_3)(L)Fe^{IV}$=O and H_2O product formation (the main product for P450) whereas the protonation at proximal oxygen leads to $(SCH_3)(L)Fe^{III}$-HOOH intermediates and Fe-O bond cleavage releasing hydrogen peroxide as a product (the product for SOR).[172] Therefore, the stability of $(SCH_3)(L)Fe^{III}$-HOOH and $(SCH_3)(L)Fe^{IV}$=O intermediates will be compared for both SOR and P450 models. Finally, to represent the solvent-exposed location of the active site of the enzymes, we also compare the stability of $(SCH_3)(L)Fe^{III}$-HOOH and $(SCH_3)(L)Fe^{IV}$=O complexes that included hydrogen bonds from explicit water molecules.

5.3.1 Ferric acetate model, $[(SCH_3)(ImH)_4Fe^{III}\text{-OAc}]^+$, the resting state of SOR

The crystal structures of the iron active site in SOR shows the iron center binds to four histidine ligands at the equatorial plane and one cysteine at the axial position; the sixth coordinate is either found empty[183,184] or vary from glutamate,[32,185] water,[32] to (hydro)peroxide.[185] Typically, the water molecule binds loosely to iron center (Fe-O ~ 2.6 Å).[32] On the other hand, the glutamate binds tightly at the ferric resting state of SOR[32] and is known to be in the high-spin (S = 5/2) state.[182] Therefore we chose to perform geometry optimization of all possible spin state (S = 1/2, 3/2, and 5/2) for $[(SCH_3)(ImH)_4Fe^{III}\text{-OAc}]^+$ (Scheme 5.2) to verify the accuracy of PBE and B3LYP density functionals for our calculation system in comparison to the glutamate-bound ferric resting state from the crystal structure.[32] The geometry parameters from calculations and the crystal structure are shown in Table 5.1 and atom labels are displayed in Scheme 5.2.

Table 5.1 Geometry parameters and relative free energies of $(SCH_3)(ImH)_4Fe^{III}$-OAc for SOR model.

	1DQI[a]	**1DO6**[a]	**PBE/BS-II**			**PBE/BS-I**			**B3LYP/BS-I**		
S	5/2	5/2	1/2	3/2	5/2	1/2	3/2	5/2	1/2	3/2	5/2
ΔG (kcal/mol)	-	-	0.00	9.93	11.01	0.00	6.79	5.40	0.00	-4.02	-8.60
ΔG^b (kcal/mol)	-	-	0.00	-1.56	-8.39	0.00	-1.79	-8.84	-	-	-
Geometry (Å, deg)											
Fe-O1	2.15	2.01	1.99	1.95	2.00	2.01	1.93	2.01	2.00	1.97	2.02
Fe-S	2.46	2.42	2.21	2.23	2.37	2.23	2.28	2.41	2.28	2.34	2.40
Fe-N7	2.09	2.14	2.02	2.04	2.20	2.01	2.04	2.21	2.03	2.09	2.21
Fe-N20	2.20	2.09	1.99	2.34	2.22	2.01	2.37	2.24	2.05	2.33	2.24
Fe-N9	2.16	2.20	2.00	2.03	2.17	2.01	2.02	2.18	2.03	2.07	2.19
Fe-N6	2.20	2.15	1.97	2.28	2.21	1.97	2.35	2.23	2.00	2.30	2.22
Fe-S-C22	117.0	117.6	114.1	112.1	111.4	115.3	111.4	110.4	114.8	111.4	113.8
Fe-O1-C45	175.0	162.7	133.1	136.0	146.7	134.5	135.5	149.3	135.3	136.7	140.3
N7-Fe-S-C22	10.4	18.4	-7.8	8.7	-19.1	-34.9	10.1	-18.6	-39.9	8.4	-11.7

[a] PDB codes of the X-ray crystal structures.
[b] B3LYP//PBE

The PBE relative free energies and structures from "all-electron" basis set on iron (BS-II) are compared to those from an effective core potential (ECP) on iron (BS-I). The Fe-ligand atom bond distances are closest to the crystal structure for the high-spin state in both PBE and B3LYP optimization (Table 5.1). In particular, the Fe-N bonds are a little too long in the high-spin calculation, but too short in the low-spin case and too varied in the intermediate-spin case. The high-spin structures have Fe-O and Fe-S bonds in a good agreement with the crystal structure but these bonds are predicted to be too short in the lower spin states. Although, the N7-Fe-S-C22 dihedral angle is negative for the high-spin structure, in which the methyl group of methyl thiolate is on the opposite side of N7-Fe-S plane from the one found in the crystal structure, this angle is still in the small range. The Fe-S-C22 and Fe-O1-C45 bond angles and are also varied from the crystal structure mainly because the interaction from the amino acid side chain is not included. In general, all electron basis set (BS-II) and the basis set with effective core potential on iron (BS-I) give similar structural parameters and the same trend for the relative free energy (Table 5.1). As expected from other studies,[186,187] the pure density functional PBE tends to prefer the low-spin states. With B3LYP functional, the high-spin state has the lowest relative free energy consistent with the experimental results. However, the high-spin geometries from PBE and B3LYP are insignificantly different; the bond distances differ by only 0.01 Å and the bond angles vary by 9^{o}. Moreover, the calculated single point energy by B3LYP with PBE optimized geometry gave the same trend for the relative free energies as B3LYP optimized geometry with high-spin state as the most stable structure. Therefore, we will apply B3LYP//PBE/BS-I to all other structures as this compromise produces the correct spin states and has more rapid geometry optimization than B3LYP.

5.3.2 Ferric hydroperoxo model, $(SCH_3)(L)Fe^{III}$-OOH

The ferric hydroperoxo, Fe^{III}-OOH, is a common intermediate observed for the active sites of both SOR and P450 enzymes. The optimized geometric parameters and the enthalpies and free energies relative to the low-spin state for $(SCH_3)(L)Fe^{III}$-OOH model of SOR and P450 active sites are shown in Figure 5.1. Mulliken atomic charges and spin densities are presented in Table 5.2. From the calculated spin densities, one and three unpair electrons, for doublet and quartet state, respectively, reside mainly on the iron center in both enzyme models (> 80%). In the sextet state, four of the five unpair electrons are on iron while the other is distributed differently in SOR and P450 models. In SOR model, the other electron is mainly on the SCH_3 group (~45%) with the remainder on proximal oxygen (~25%) and four imidazole ligands (~23%); in P450 model, the other electron is mainly on both proximal oxygen (~41%) and SCH_3 (~30%) with the remainder on the distal oxygen (~10%) and porphyrin (~18%).

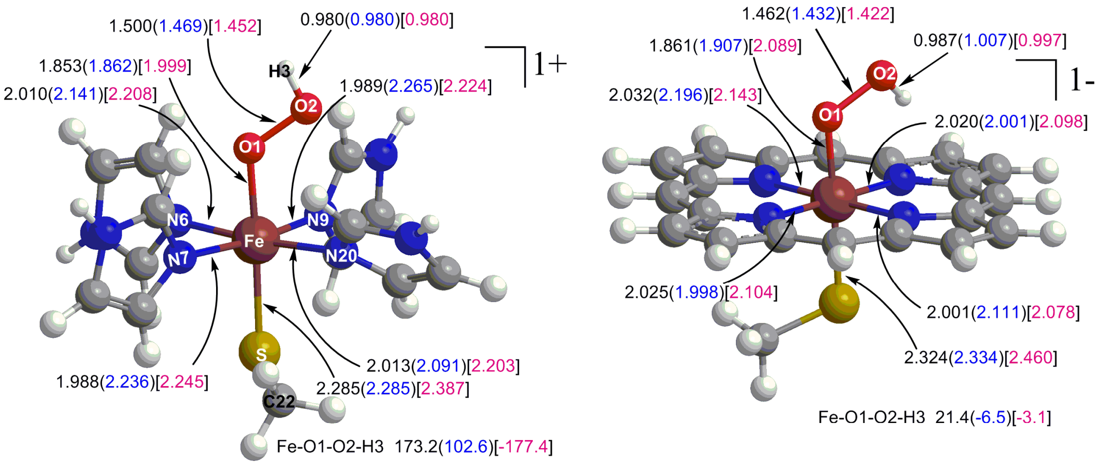

$\Delta H = 0.00(-0.57)[0.60]$
$\Delta G = 0.00(-4.33)[-5.98]$

$\Delta H = 0.00(14.03)[11.83]$
$\Delta G = 0.00(13.13)[9.27]$

Figure 5.1 Ferric hydroperoxo model, $(SCH_3)(L)Fe^{III}$-OOH, for SOR (L=ImH_4) and P450 (L=Por). The enthalpies and the free energies relative to doublet state in kcal/mol, selected bond distances in Å, and selected dihedral angles in deg of doublet, quartet (in parenthesis), and sextet (in bracket) states are presented.

Table 5.2 Mulliken atomic charges and spin densities in ferric hydroperoxo model, **$(SCH_3)(L)Fe^{III}$-OOH** (L = ImH_4 for SOR and Por for P450).

	SOR			P450		
spin	1/2	3/2	5/2	1/2	3/2	5/2
Total charge	1+	1+	1+	1-	1-	1-
Atomic charge						
Fe	-1.302	-1.107	-1.265	-1.169	-1.158	-1.209
O_p	-0.237	-0.442	-0.334	-0.075	-0.059	0.059
O_d	-0.543	-0.230	-0.411	-0.451	-0.472	-0.481
SCH_3	0.106	0.165	0.139	-0.017	0.018	-0.070
L	2.581	2.328	2.487	0.346	0.230	0.283
Atomic spin density						
Fe	0.869	3.063	4.035	0.880	2.804	4.011
O_p	0.103	0.006	0.245	0.154	0.176	0.408
O_d	0.007	-0.023	0.038	0.018	0.045	0.103
SCH_3	0.093	-0.112	0.452	0.050	0.001	0.300
L	-0.071	0.064	0.229	-0.102	-0.025	0.182

From the free energy calculation, SOR is predicted to have a high-spin ground state with low-spin and intermediate-spin states higher in free energies by 5.98 and 1.65 kcal/mol, respectively, whereas P450 has low-spin ground state with intermediate-spin and high-spin states higher in free energies by 13.13 and 9.27 kcal/mol, respectively (Figure 5.1). The high-spin ground state for SOR model and the low-spin ground state for P450 model of $(SCH_3)(L)Fe^{III}$-OOH complexes correspond to their spin states found by the experiment.[188,189]

The difference in ground spin state for Fe^{III}-OOH intermediates of P450 and SOR models derives from the difference in equatorial-ligand structure, the constrained ring of porphyrin ligand vs. the extendable Fe-N bonds of imidazole ligands, which can be explained by their molecular orbital energies. Since the SOR and P450 models contain different total charges (1+ and 1-, respectively), the relative molecular orbital (MO) energies with respect to the orbital with π-OOH$^-$ bonding with d_{xz} character are used to compare the MO energy levels in the high-spin $(SCH_3)(L)Fe^{III}$-OOH complexes between two enzyme models (Scheme 5.4). In the unrestricted B3LYP calculation, the singly occupied MOs are the occupied alpha orbitals that resemble to the unoccupied beta orbitals. Here, all five singly occupied MOs consist of the main contribution from iron d-orbitals antibonding to ligand orbitals. Since we defined the y-axis to parallel to the O-O bond and the orientation of O-O bond over the equatorial ligand plane is different in SOR and P450 models as shown Scheme 5.4, the d_{x2-y2} in P450 model is equivalent to d_{xy} in SOR model in that these d orbitals form σ-antibonding to the equatorial ligands whereas the d_{xy} in P450 model is equivalent to d_{x2-y2} in SOR model in that these d orbitals form π-antibonding to the equatorial ligands. In the high-spin state, unlike low- and intermediate-spin states, the unpair electrons occupy d_{x2-y2} and d_{z2} orbitals, which are σ-antibonding to ligand orbitals; lengthening of Fe-N, Fe-O and Fe-S bonds stabilizes these orbitals.

The MO energies of d_{x2-y2} orbital in P450 model are higher than the d_{xy} orbital in SOR model. Without any constraint on the ligands, SOR has all Fe-O, Fe-S, and Fe-N bond distances in sextet state longer than the corresponding ones in doublet and quartet states (Figure 5.1). For P450 model, although Fe-O and Fe-S bond distances in sextet state extend longer than the ones in doublet and quartet states, the porphyrin constrains the Fe-N bond distances, which are barely change for different spin states. Therefore the

Scheme 5.4 The molecular orbital energies (ε) of the selected orbitals relative to the orbital of π-OOH^- bonding to d_{xz} for the high-spin $(SCH_3)(L)Fe^{III}$-OOH model for SOR and P450 active sites are shown in hartree for both alpha and beta orbitals. The absolute molecular orbital energies are ε - 0.510 for SOR model and ε - 0.262 for P450 model. Note that we defined the z axis parallel to Fe-S bond and the y axis parallel to O-O bond.

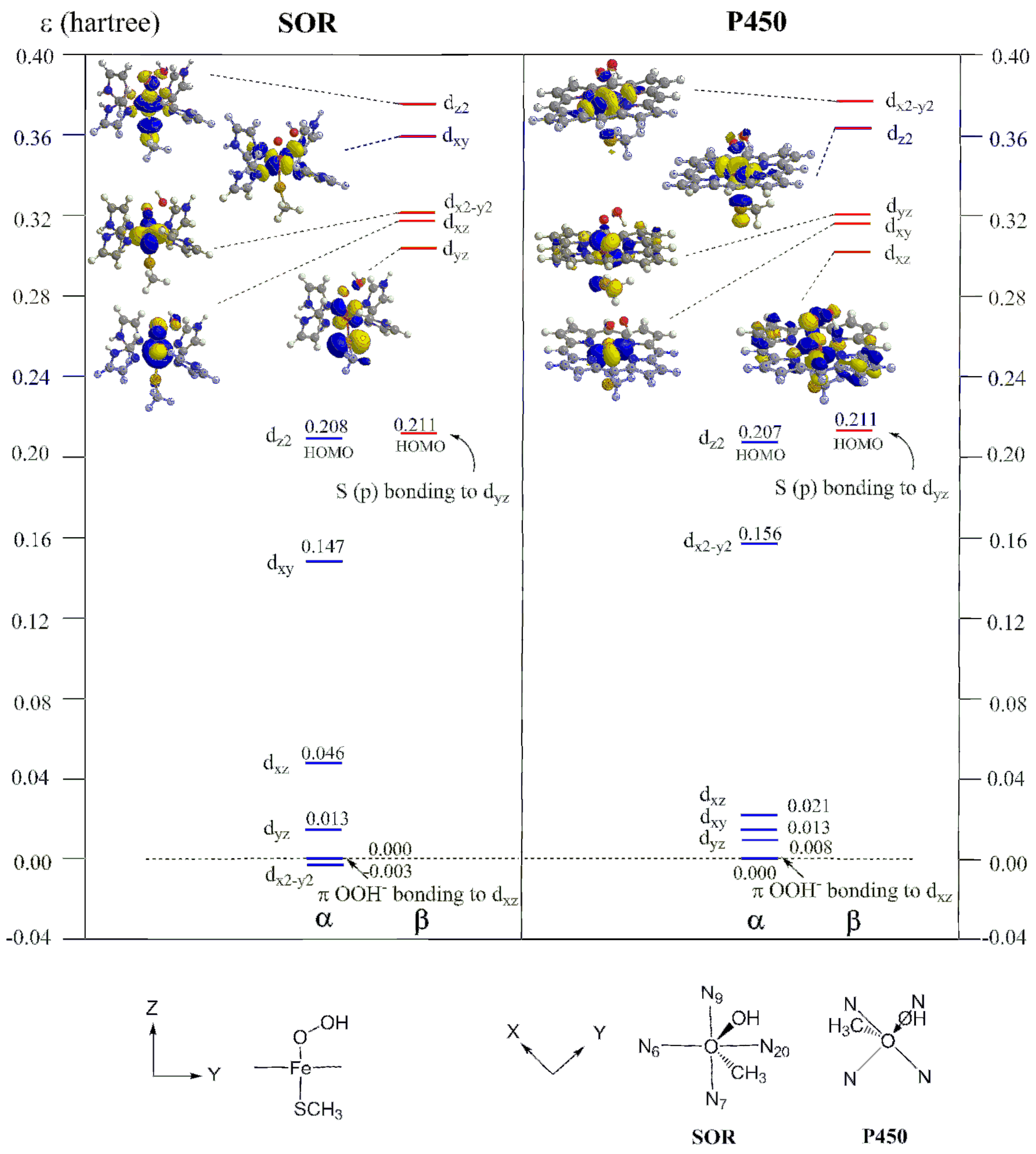

constrained ring of porphyrin ligand prevents the high-spin ground state of $(SCH_3)(L)Fe^{III}$-OOH in P450 model whereas extendable Fe-N bonds with imidazole ligands accommodate the high-spin ground state in SOR.

The different ground spin states of $(SCH_3)(L)Fe^{III}$-OOH intermediates for SOR and P450 models can contribute to different reaction paths. Interestingly, in our calculation, for the higher spin state in both enzyme models, O-O bond distances shorten whereas Fe-O bond distances lengthen (Figure 5.1). Thus, the high-spin ground state in SOR has a strong O-O bond but a weak Fe-O bond, whereas the low-spin ground state in P450 has a weak O-O bond but a strong Fe-O bond. Moreover, in SOR the atomic charge (Table 5.2) on distal oxygen in the high-spin ground state is only slightly more negative than that on the proximal oxygen (-0.411 and -0.334, respectively) whereas the atomic charge on the distal oxygen in its low-spin state is much more negative than on the proximal oxygen (-0.543 and -0.237, respectively). The same situation is found for the low-spin ground state in P450; the atomic charge on distal oxygen is highly negative (-0.481) in comparison to the one on proximal oxygen which is almost neutral (0.059). Therefore, the charges and the distances in the high-spin $(SCH_3)(L)Fe^{III}$-OOH of SOR model favors protonation at proximal oxygen and Fe-O bond cleavage, whereas the charges and the distances in the low-spin $(SCH_3)(L)Fe^{III}$-OOH of P450 model favors protonation at distal oxygen and O-O bond cleavage.

5.3.3 Ferric hydrogen peroxide model, $(SCH_3)(L)Fe^{III}$-HOOH, vs. oxo-ferryl model, $(SCH_3)(L)Fe^{IV}=O$

The protonation at the proximal oxygen of ferric hydroperoxo, Fe^{III}-OOH, leads to the formation of ferric hydrogen peroxide (Fe^{III}-HOOH), the intermediate before Fe-O bond cleavage and release of H_2O_2, the product of SOR catalytic cycle. For both SOR and P450 models, in comparison to $(SCH_3)(L)Fe^{III}$-OOH, the $(SCH_3)(L)Fe^{III}$-HOOH has a shorter Fe-S bond and a longer Fe-O bond in preparation for H_2O_2 release (Figure 5.1 and 5.2). For the SOR model, the sextet ground state of $(SCH_3)(L)Fe^{III}$-HOOH is much lower in free energy than the doublet and quartet states that have free energies close to

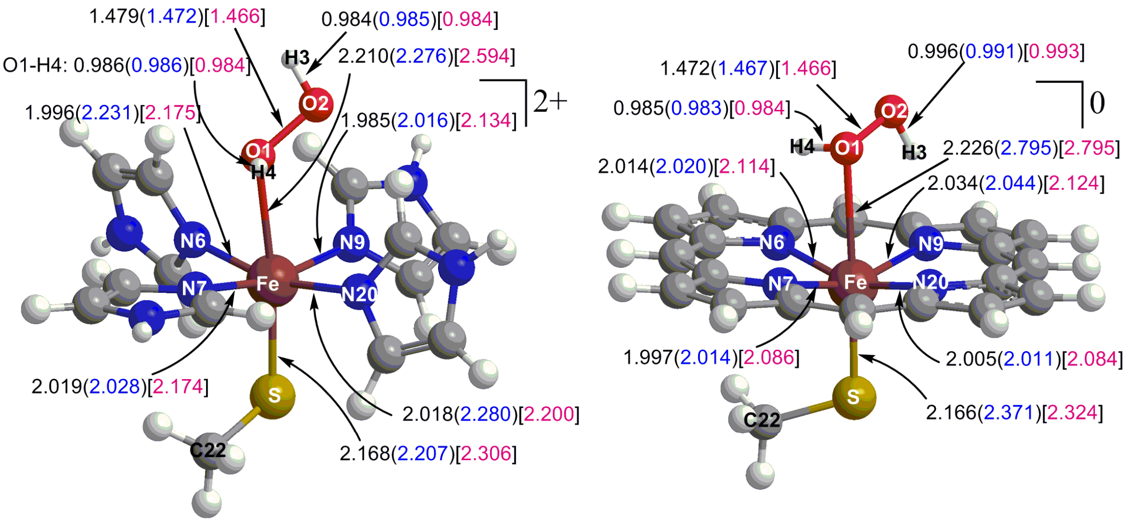

Figure 5.2 Ferric hydrogen peroxide model, $(SCH_3)(L)Fe^{III}$-HOOH, for SOR (L=ImH_4) and P450 (L=Por). The selected bond distances of doublet, quartet (in parenthesis), and sextet (in bracket) states are presented in Å.

Table 5.3 The relative enthalpies and free energies (kcal/mol) of ferric hydrogen peroxide and oxo-ferryl models with respect to the doublet state of $(SCH_3)(L)Fe^{III}$-HOOH ($L = ImH_4$ for SOR and Por for P450).

	Spin	ΔH	ΔG
SOR			
$[(SCH_3)(ImH)_4Fe^{III}\text{-HOOH}]^{2+}$	S = 1/2	0.00	0.00
	S = 3/2	0.74	-2.65
	S = 5/2	-7.06	-13.47
$[(SCH_3)(ImH)_4Fe^{IV}{=}O]^{2+} + H_2O$	S = 1/2	-7.59	-18.69
	S = 3/2	-8.76	-20.33
	S = 5/2	-4.09	-19.17
$[(SCH_3)(ImH)_4Fe^{IV}{=}O\text{--}H_2O]^{2+}$	S = 1/2	-16.38	-19.58
	S = 3/2	-16.45	-18.66
	S = 5/2	-10.19	-16.58
P450			
$[(SCH_3)(Por)Fe^{III}\text{-HOOH}]^0$	S = 1/2	0.00	0.00
	S = 3/2	4.78	1.09
	S = 5/2	3.45	-0.17
$[(SCH_3)(Por)Fe^{IV}{=}O]^0 + H_2O$	S = 1/2	-3.99	-14.66
	S = 3/2	-5.37	-16.80
	S = 5/2	6.87	-5.11
$[(SCH_3)(Por)Fe^{IV}{=}O\text{--}H_2O]^0$	S = 1/2	-10.25	-12.76
	S = 3/2	-11.47	-14.46
	S = 5/2	0.93	-2.76

each other (Table 5.3). For the P450 model, the high-spin state of $(SCH_3)(L)Fe^{III}$-HOOH is found to lie very close in free energy to low- and intermediate-spin states, all within a range of 1 kcal/mol (Table 5.3).

Like $(SCH_3)(L)Fe^{III}$-OOH, the calculated spin density predicted that the one and three unpair electrons for doublet and quartet states of $(SCH_3)(L)Fe^{III}$-HOOH reside mainly on the iron center (Table 5.4). For the sextet state, four of five unpair electrons are on iron while the other unpair electron is distributed mainly on SCH_3 (~78%) with the remainder on four imidazole ligands (~24%) in SOR model, but distributed mainly on both SCH_3 (~56%) and porphyrin (~42%) in P450 model. In both enzyme models, the small spin density is found on distal oxygen in $(SCH_3)(L)Fe^{III}$-HOOH (Table 5.4) just like in $(SCH_3)(L)Fe^{III}$-OOH (Table 5.1). Unlike $(SCH_3)(L)Fe^{III}$-OOH, the proximal oxygen in $(SCH_3)(L)Fe^{III}$-HOOH has very small spin density due to the long Fe-O bond.

Protonation at the distal oxygen of ferric hydroperoxo leads to O-O bond cleavage and formation of oxo-ferryl complex, Fe^{IV}=O, and H_2O, the main product for P450. The $(SCH_3)(L)Fe^{IV}$=O model complexes are calculated for both P450 and SOR

Table 5.4 Mulliken atomic charges and spin densities in ferric hydrogen peroxide model, **$(SCH_3)(L)Fe^{III}$-HOOH** (L = ImH_4 for SOR and Por for P450).

	SOR			P450		
spin	1/2	3/2	5/2	1/2	3/2	5/2
Total charge	2+	2+	2+	0	0	0
Atomic charge						
Fe	-1.423	-1.404	-1.389	-1.181	-0.965	-1.092
O_p	-0.080	-0.069	-0.159	0.155	-0.010	0.026
O_d	-0.465	-0.449	-0.441	-0.555	-0.550	-0.573
SCH_3	0.459	0.531	0.531	0.317	0.150	0.325
L	2.722	2.588	2.665	0.487	0.639	0.563
Atomic spin density						
Fe	0.879	3.154	3.997	0.968	2.582	4.042
O_p	-0.007	-0.012	-0.026	-0.010	-0.025	-0.018
O_d	0.000	0.000	0.006	0.000	0.007	0.005
SCH_3	0.195	-0.187	0.783	0.129	0.534	0.559
L	-0.066	0.044	0.242	-0.088	-0.090	0.420

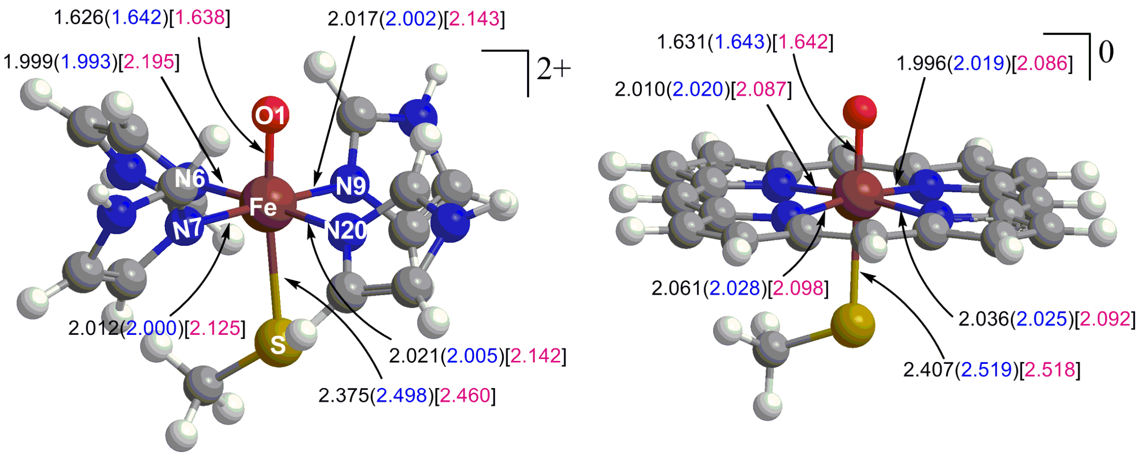

Figure 5.3 Oxo-ferryl model, $(SCH_3)(L)Fe^{IV}{=}O$, for SOR ($L{=}ImH_4$) and P450 (L=Por). The selected bond distances of doublet, quartet (in parenthesis), and sextet (in bracket) states are presented in Å.

(Figure 5.3) to compare their stability with that of $(SCH_3)(L)Fe^{III}$-HOOH. In both SOR and P450 models, $(SCH_3)(L)Fe^{IV}{=}O$ has a shorter Fe-O bond and a longer Fe-S bond than those in $(SCH_3)(L)Fe^{III}$-OOH implying a strong Fe-O bond with stronger trans influence. From the spin density calculation, unlike either $(SCH_3)(L)Fe^{III}$-OOH or $(SCH_3)(L)Fe^{III}$-HOOH, in doublet and quartet spin states of $(SCH_3)(L)Fe^{IV}{=}O$ for both enzyme models (Table 5.5), two unpair electrons of the same spin distribute more or less equally over both the iron and oxygen atoms,[37] whereas the third unpair electron is distributed on SCH_3 and the equatorial ligands, antiparallel and parallel to the other two unpaired electrons, respectively. Although, in both SOR and P450 models, the third unpair electron is distributed mainly on SCH_3 more than equatorial ligand, there is still a substantial amount of spin density on porphyrin compared to the minor extent on four imidazole ligands because of the conjugated structure of the porphyrin in P450.

Moreover, the issue of whether the spin density distribution from the third unpaired electron is mainly on sulfur or porphyrin can depend on various aspects of the model[37] and is particularly sensitive to H-bonding to the thiolate.[190,191]

Table 5.5 Mulliken atomic charges and spin densities in oxo-ferryl model, **$(SCH_3)(L)Fe^{IV}{=}O$** (L = ImH_4 for SOR and Por for P450).

	SOR			P450		
spin	1/2	3/2	5/2	1/2	3/2	5/2
Total charge	2+	2+	2+	0	0	0
Atomic charge						
Fe	-0.812	-0.738	-0.768	-0.724	-0.626	-0.600
O_p	-0.518	-0.495	-0.505	-0.381	-0.369	-0.395
SCH_3	0.509	0.420	0.493	0.296	0.220	0.250
L	2.821	2.813	2.781	0.809	0.775	0.745
Atomic spin density						
Fe	1.157	1.106	3.053	1.177	1.093	3.087
O_p	0.965	0.940	0.722	0.937	0.950	0.707
SCH_3	-1.000	0.938	0.851	-0.726	0.687	0.581
L	-0.123	0.015	0.374	-0.388	0.270	0.626

In SOR, the quartet ground state of $(SCH_3)(L)Fe^{IV}{=}O$ is found to lie close to the sextet and doublet states which have free energies in small range within ~1 kcal/mol. In P450 model, the ground state of the $(SCH_3)(L)Fe^{IV}{=}O$ complex is also the quartet state, which has the free energy close to the doublet state but much lower than the sextet state. Considering the relative free energy for the various states of both $(SCH_3)(L)Fe^{III}$-HOOH and $(SCH_3)(L)Fe^{IV}{=}O$ + H_2O (Table 5.3), the most stable structure is the $(SCH_3)(L)Fe^{IV}{=}O$ complex in the quartet state for both SOR and P450 models. The low free energy of the $(SCH_3)(L)Fe^{IV}$=O complex and H_2O in comparison to $(SCH_3)(L)Fe^{III}$-HOOH complex is largely derived from the entropy contribution (~ -11 to -15 kcal/mol), which favors the $(SCH_3)(L)Fe^{IV}$=O and H_2O, dissociated products, over the $(SCH_3)(L)Fe^{III}$-HOOH, a single product. In P450 model, the free energies of quartet state $(SCH_3)(L)Fe^{IV}$=O and H_2O is much more favorable than sextet state $(SCH_3)(L)Fe^{III}$-HOOH by -16.63 kcal/mol whereas the enthalpy change favors quartet state $(SCH_3)(L)Fe^{IV}$=O and H_2O by a smaller number (-8.82 kcal/mol). The same situation is also applied to SOR model; the enthalpy of sextet ground state of $(SCH_3)(L)Fe^{III}$-HOOH is only 1.60 kcal/mol higher than the enthalpy of quartet ground state of $(SCH_3)(L)Fe^{IV}$=O and H_2O whereas the free energy difference is 6.86 kcal/mol.

To assure that the lower free energy of $(SCH_3)(L)Fe^{IV}$=O complex compared to Fe^{III}-HOOH complex in both enzyme active-site models is not merely from the dissociation of H_2O, we also calculated water-bound oxo-ferryl, $(SCH_3)(L)Fe^{IV}$=O--H_2O, complex (Figure 5.4). Although the Fe-O bond is slightly longer in $(SCH_3)(L)Fe^{IV}$=O--H_2O than the one in $(SCH_3)(L)Fe^{IV}$=O complex, there is no significantly change in the overall geometry of $(SCH_3)(L)Fe^{IV}$=O--H_2O from $(SCH_3)(L)Fe^{IV}$=O complex. The relative free energies of $(SCH_3)(L)Fe^{IV}$=O--H_2O product showed a similar trend to those of $(SCH_3)(L)Fe^{IV}$=O and H_2O products (Table 5.3). For P450 model, the doublet ground state of $(SCH_3)(L)Fe^{III}$-OOH favors protonation at distal oxygen in corresponding to the fact that the quartet ground state of $(SCH_3)(L)Fe^{IV}$=O--H_2O product is more favorable than the sextet ground state of $(SCH_3)(L)Fe^{III}$-HOOH. This result is in consistent with the appearance of Compound I

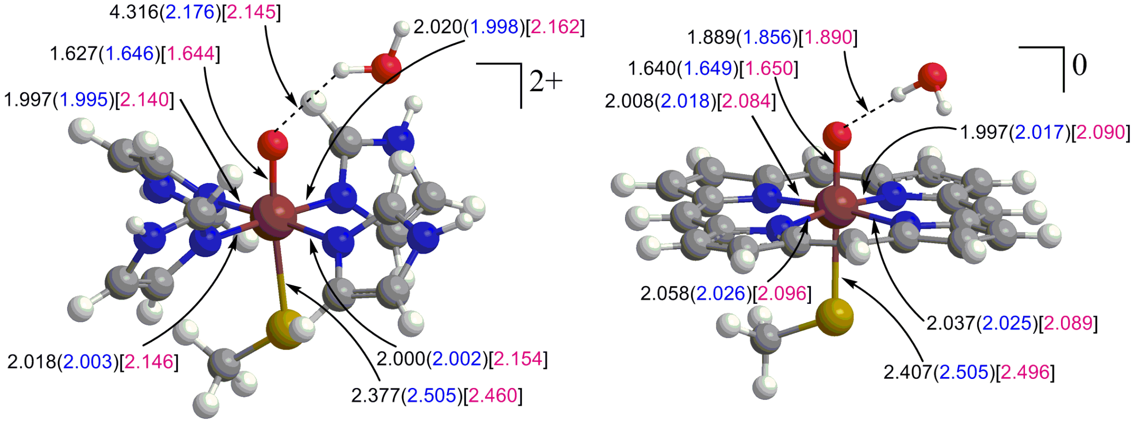

Figure 5.4 Oxo-ferryl model with a water molecule, $(SCH_3)(L)Fe^{IV}{=}O{-}{-}H_2O$, for SOR (L=$ImH_4$) and P450 (L=Por). The selected bond distances of doublet, quartet (in parenthesis), and sextet (in bracket) states are presented in Å.

intermediate in P450 catalytic cycle, in which the quartet ground state of $(SCH_3)(L)Fe^{IV}{=}O$ complex is found with the free energy closely lying to the doublet state as in previous calculation studies.[37,192-194] On the other hand, for the SOR model, the doublet state of $(SCH_3)(L)Fe^{IV}{=}O{-}{-}H_2O$ is the lowest free energy spin state with the quartet state lying very closely. Although, in SOR model, the electronic structure of the sextet ground state of $(SCH_3)(L)Fe^{III}$-OOH could support the formation of the $(SCH_3)(L)Fe^{III}$-HOOH, the intermediate to produce H_2O_2, the sextet ground state $(SCH_3)(L)Fe^{III}$-HOOH is still lying 6.11 kcal/mol higher than the doublet ground state $(SCH_3)(L)Fe^{IV}{=}O{-}{-}H_2O$. Thus, there must be other factors that stabilize the Fe^{III}-HOOH intermediate in SOR. In the next section, the effect of hydrogen bonding from explicit water molecules will be included to represent the solvent-exposed location of the active site of SOR.

5.3.4 The models including explicit water molecules for ferric hydrogen peroxide, $(SCH_3)(L)Fe^{III}$-HOOH--$2H_2O$, and oxo-ferryl, $(SCH_3)(L)Fe^{IV}$=O--$3H_2O$

Since the active site of SOR is located at the solvent-exposed position, the hydrogen bonding between hydrogen peroxide at the sixth coordinate on iron active site and water molecules could be involved in stabilizing the Fe^{III}-HOOH species. On the other hand, the active site of P450 is located within the enclosed pocket of the enzyme, which may constrain the water network arrangement with respect to ligands in the sixth coordination site of the iron center.[35] However, we will assume a similar arrangement of water molecules for $(SCH_3)(L)Fe^{III}$-HOOH model of both SOR and P450. The free energy of $(SCH_3)(L)Fe^{III}$-HOOH--$2H_2O$ complex, in which two water molecules and proximal and distal oxygen atoms form three hydrogen bonds, is calculated and compared to the free energy of $(SCH_3)(L)Fe^{IV}$=O complex and three-water-molecule cluster and the free energy of $(SCH_3)(L)Fe^{IV}$=O--$3H_2O$ complex. This latter complex and three-water-molecule cluster are chosen to provide the same total number of hydrogen bonds in order to provide a fair energetic comparison. The relative free energies and enthalpies of $(SCH_3)(L)Fe^{III}$-HOOH--$2H_2O$, $(SCH_3)(L)Fe^{IV}$=O + $3H_2O$-cluster, and $(SCH_3)(L)Fe^{IV}$=O--$3H_2O$ active site models of SOR and P450, which included three-hydrogen bonding from explicit water molecules, are shown in Table 5.6.

Table 5.6 The relative enthalpies and free energies (kcal/mol) of ferric hydrogen peroxide and oxo-ferryl models with two extra water molecules with respect to the doublet state of $(SCH_3)(L)Fe^{III}$-HOOH--$2H_2O$ (L = ImH_4 for SOR and Por for P450).

	Spin	ΔH	ΔG
SOR			
$[(SCH_3)(ImH)_4Fe^{III}\text{-HOOH--}2H_2O]^{2+}$	S = 1/2	0.00	0.00
	S = 3/2	0.66	-2.66
	S = 5/2	-5.23	-10.84
$[(SCH_3)(ImH)_4Fe^{IV}=O]^{2+}$ + $3H_2O$-cluster	S = 1/2	5.83	-6.06
	S = 3/2	4.66	-7.71
	S = 5/2	9.33	-6.55
[a]$[(SCH_3)(ImH)_4Fe^{IV}=O\text{--}3H_2O]^{2+}$	S = 1/2	-4.36	-8.18
	S = 3/2	-4.41	-8.70
	S = 5/2	1.67	-4.86
P450			
$[(SCH_3)(Por)Fe^{III}\text{-HOOH--}2H_2O]^0$	S = 1/2	0.00	0.00
	S = 3/2	4.10	1.39
	S = 5/2	0.89	-2.31
$[(SCH_3)(Por)Fe^{IV}=O]^0$ + $3H_2O$-cluster	S = 1/2	-6.66	-17.66
	S = 3/2	-8.05	-19.80
	S = 5/2	4.20	-8.11
$[(SCH_3)(Por)Fe^{IV}=O\text{--}3H_2O]^0$	S = 1/2	-17.87	-18.43
	S = 3/2	-18.71	-20.07
	S = 5/2	-5.97	-7.77

[a]Structures have one small imaginary frequency (~ -30).

The addition of two water molecules to $(SCH_3)(L)Fe^{III}$-HOOH model creates three hydrogen-bonds: O14—H4, O14—H5, and O13—H3 (Figure 5.5), whereas $(SCH_3)(L)Fe^{IV}$=O--$3H_2O$ also compose of three hydrogen-bonds: O1—H4, O13—H3, and O14—H5 (Figure 5.6), so does $(SCH_3)(L)Fe^{IV}$=O and three-water-molecule cluster

(Figure 5.7). In fact, for SOR model, the fully optimized structure of $(SCH_3)(L)Fe^{IV}$=O--$3H_2O$ has four hydrogen-bonds, in which the fourth hydrogen-bond is formed between O14 and N-H from one of the imidazole ligands. Therefore, we fixed the bond angles of Fe-O1-H4, O1-H4-O2, and O2-H3-O13 for $(SCH_3)(L)Fe^{IV}$=O--$3H_2O$ in SOR model during the geometry optimization to keep the water chain in the upright direction (Figure 5.6), preventing the formation of the fourth H-bond.

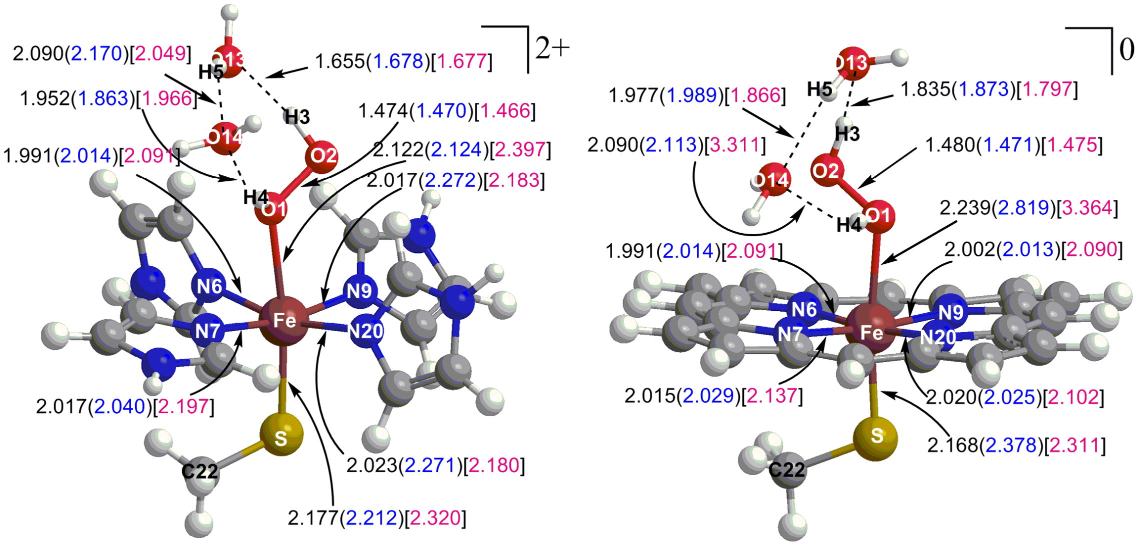

Figure 5.5 Ferric hydrogen peroxide model with hydrogen bonding from two explicit water molecules, $(SCH_3)(L)Fe^{III}$-HOOH--$2H_2O$, for SOR (L=ImH_4) and P450 (L=Por). The selected bond distances of doublet, quartet (in parenthesis), and sextet (in bracket) states are presented in Å.

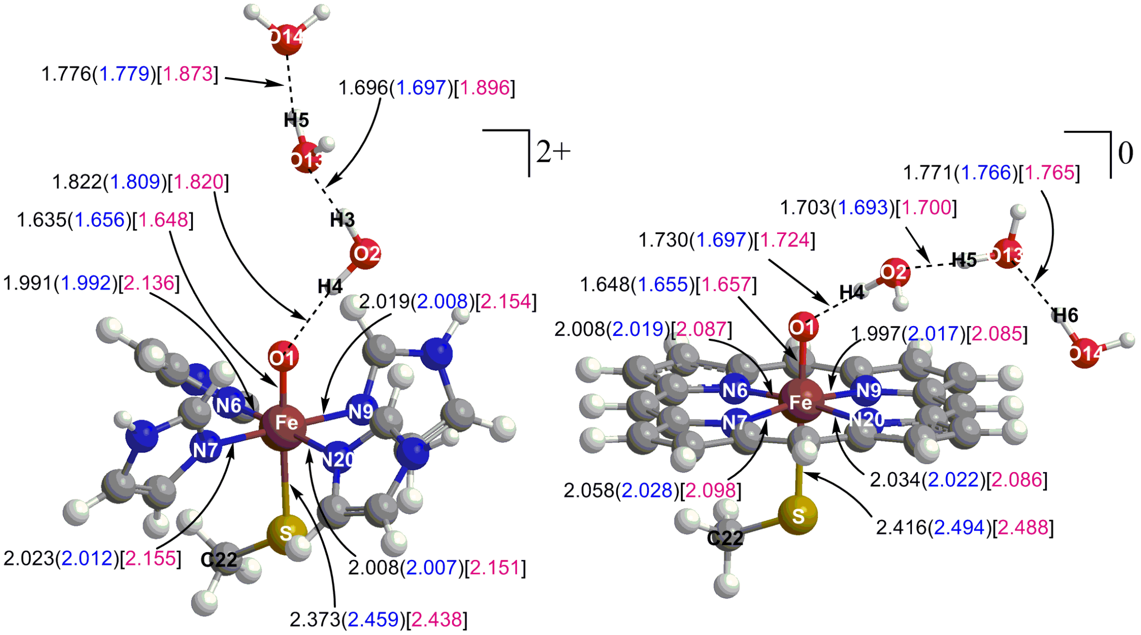

Figure 5.6 Oxo-ferryl model with hydrogen bonding from three explicit water molecules, $(SCH_3)(L)Fe^{IV}{=}O{-}{-}3H_2O$, for SOR (L=ImH$_4$) and P450 (L=Por). The selected bond distances of doublet, quartet (in parenthesis), and sextet (in bracket) states are presented in Å.

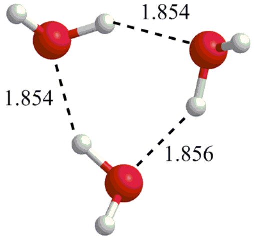

Figure 5.7 Three water cluster

For both SOR and P450 models, the iron-ligand bond lengths of $(SCH_3)(L)Fe^{IV}{=}O{-}{-}3H_2O$ are not significantly changed from $(SCH_3)(L)Fe^{IV}{=}O$. The relative free energies of $(SCH_3)(L)Fe^{IV}{=}O{-}{-}3H_2O$ and $(SCH_3)(L)Fe^{IV}{=}O + 3H_2O$-cluster show the similar trend (Table 5.6); for P450, the quartet ground state is lying close to the doublet state and the sextet state has higher free energy whereas for SOR, the quartet state has the lowest free energies with doublet and sextet states lying close to the ground state within the range of ~ 4 kcal/mol.

With two explicit water molecules, the Fe-O bond in the P450 model of $(SCH_3)(L)Fe^{III}$-HOOH--$2H_2O$ lengthens from that without water molecules (Figure 5.2 and 5.5). Clearly, the hydrogen bonds from water molecules do not help stabilize $(SCH_3)(L)Fe^{III}$-HOOH in the P450 model; the quartet ground state of both $(SCH_3)(L)Fe^{IV}$=O--$3H_2O$ complex and $(SCH_3)(L)Fe^{IV}$=O + $3H_2O$-cluster still have lower free energy than the sextet ground state of Fe^{III}-HOOH--$2H_2O$ by ~ -17 kcal/mol (Table 5.6). Unlike the P450 model, the SOR model of $(SCH_3)(L)Fe^{III}$-HOOH--$2H_2O$ has shorter Fe-O bond than that without explicit water molecules by 0.1-0.2 Å (Figure 5.2 and 5.5). The hydrogen bonds from water molecules in the SOR model stabilize $(SCH_3)(L)Fe^{III}$-HOOH as reflected in the stronger Fe-O bond. With hydrogen bonds from just water molecules the sextet ground state of $(SCH_3)(L)Fe^{III}$-HOOH--$2H_2O$ is more stable than the quartet ground state of both $(SCH_3)(L)Fe^{IV}$=O--$3H_2O$ complex and $(SCH_3)(L)Fe^{IV}$=O + $3H_2O$-cluster by -2.14 and -3.13 kcal/mol in free energy. Our result suggests that the solvent exposed position of the active site in the SOR enzyme is a significant factor to stabilize the ferric hydrogen peroxide complex which leads SOR to hydrogen peroxide production rather than oxo-ferryl formation.

5.5 Conclusions

One of the factors that lead SOR and P450 into different reaction pathways is the different ground spin states of the ferric hydroxo, Fe^{III}-OOH, intermediate for SOR and P450 which leads to the different geometric parameters and electronic structures that results the different protonation sites. From our calculation, the high-spin ground state of $(SCH_3)(L)Fe^{III}$-OOH model for SOR has strong O-O bond, weak Fe-O bond and the atomic charge on distal oxygen is comparable to the one on proximal oxygen; therefore, the Fe^{III}-OOH intermediate in SOR tends to be protonated at proximal oxygen, forms the Fe^{III}-HOOH intermediate, and proceeds to Fe-O bond cleavage giving H_2O_2 product. On the other hand, the low-spin ground state of $(SCH_3)(L)Fe^{III}$-OOH model for P450 has weak O-O bond, strong Fe-O bond and the atomic charge on distal oxygen is highly negative compared to the one on proximal oxygen; thus, the Fe^{III}-OOH intermediate in P450 tends to be protonated at distal oxygen and proceeds to O-O bond cleavage giving H_2O and the oxo-ferryl, Fe^{IV}=O, products. Correspondingly, the quartet ground state of $(SCH_3)(L)Fe^{IV}$=O--H_2O in P450 model has lower free energy than the sextet ground state of $(SCH_3)(L)Fe^{III}$-HOOH by -14.29 kcal/mol.

The other significant factor is the active site location in the enzyme. The solvent-exposed position of the active site in SOR gives a chance for the proximal and distal oxygen in Fe^{III}-HOOH to form hydrogen bonds with water molecules. By including explicit water molecules, the sextet ground state of $(SCH_3)(L)Fe^{III}$-HOOH--$2H_2O$ in SOR has lower free energy than the quartet ground state of $(SCH_3)(L)Fe^{IV}$=O--$3H_2O$ and $(SCH_3)(L)Fe^{IV}$=O + $3H_2O$-cluster by -2.14 and -3.13 kcal/mol, respectively. Our calculation showed that both the spin state which is controlled by the differences between four N-donor ligands and the degree of solvent-exposure of the active site play an important role in the production of hydrogen peroxide in SOR.

CHAPTER VI

DENSITY FUNCTIONAL STUDY OF THE HYDROGEN PRODUCTION BY $Fe_4[MeC(CH_2S)_3]_2(CO)_8$ TETRAIRON HEXATHIOLATE HYDROGENASE MODEL

6.1 Introduction

Di-iron hydrogenases catalyze the reduction of protons to H_2. The X-ray crystal structures reveal that the enzyme's active site, named the H-cluster, consists of a di-iron [2Fe] cluster bridged to a [4Fe-4S] cluster by a cysteine ligand from the protein backbone as shown in Figure 6.1a.[41,42] The two catalytically active redox states of di-iron cluster were examined crystallographically: the Fe^IFe^{II} ($\mathbf{H_{ox}}$)[41] with one CO ligand bridging between two irons and a weakly-bound H_2O on Fe_d, and the Fe^IFe^I ($\mathbf{H_{red}}$)[42] with bridging CO in a semi-bridging position.[38-40,42] More highly oxidized $Fe^{II}Fe^{II}$ forms are also known but are believed to be catalytically inactive.[195,196]

The design of biomimetic catalyst to simulate the function of hydrogenase and to study the hydrogen production mechanism are also being persued[43-49] as alternatives materials for hydrogen production for rare and expensive platinum electrode.[197-199] Model complexes with structures similar to the active site of hydrogenase, such as di-iron hexacarbonyl dithiolate complexes and their substituted derivatives (Figure 6.1b), have been studied for hydrogen production reactivity.[43,45-49,200-216] The substitution of CO by better donor ligands, i.e., cyanide,[45] phosphine,[46-48] and cyanide/phosphine,[49] are necessary to achieve catalysis with weaker acids, at less negative reduction potential, and at high H_2 rates. Although the identity of dithiolate bridgehead in the di-iron hydrogenase structure is unknown, basic sites at the bridging thiolate[211,217] ligands have been introduced in the synthetic model catalysts. However, the H_2 production rates of these di-iron model complexes are still relatively low compared to di-iron hydrogenase.

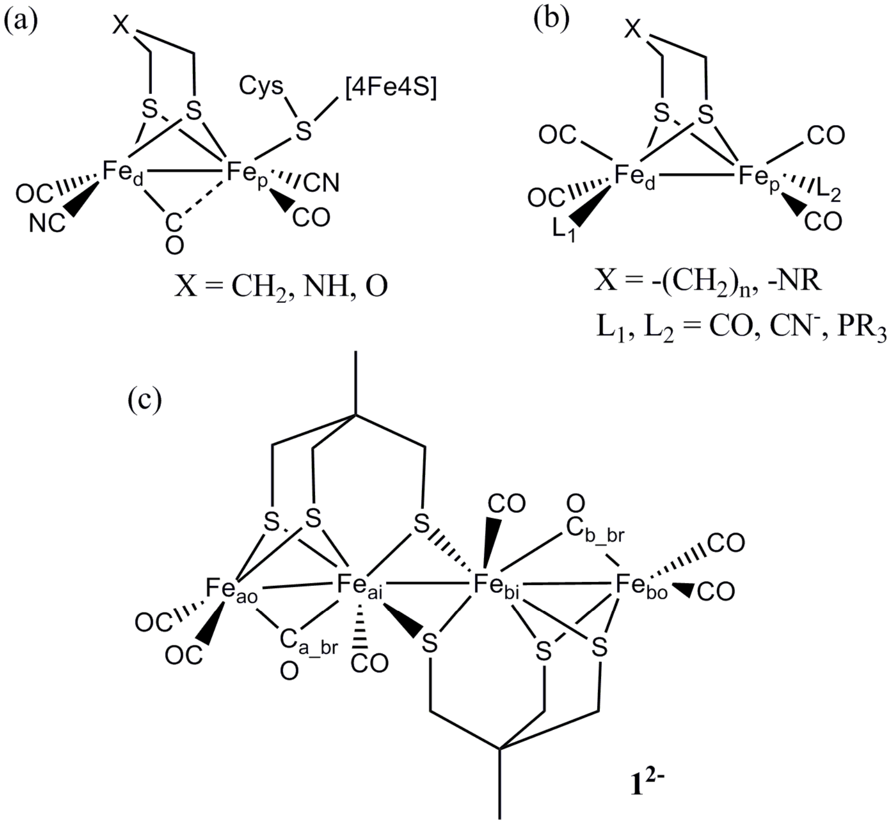

X = CH$_2$, NH, O

X = -(CH$_2$)$_n$, -NR
L_1, L_2 = CO, CN$^-$, PR$_3$

1^{2-}

Figure 6.1 Structures of (a) di-iron hydrogenase active site, (b) di-iron synthetic models, and (c) $[Fe_4(MeC(CH_2S)_3)_2(CO)_8]^{2-}$ (**1^{2-}**).

There is major difference between the stable structures of di-iron model complexes and di-iron subsite in hydrogenases. Although the structures of unstable mixed-valence $Fe^{I}Fe^{II}$ model[202,208,218] complexes are found with semi-bridging CO, a structure which resembles the $\mathbf{H_{ox}}$ state of di-iron hydrogenases, the stable $Fe^{I}Fe^{I}$ model complexes are generally found with all terminal CO, a structure which does not fully replicate the semi-bridging CO structures in $\mathbf{H_{red}}$ state of di-iron hydrogenases. The semi-bridging carbonyl structure at [2Fe] subsite in $\mathbf{H_{red}}$ state of di-iron hydrogenases is created for the location of the vacant site on distal iron (Fe_d), which favors the protonation at the terminal position of Fe_d. The experimental data on $[Fe_2(S(CH_2)_2S)(\mu\text{-}CO)(H)(CO)(PMe_3)_4]^+$ also showed that a terminal hydride can be more active than a bridging hydride.[206]

Density functional calculation[39] suggested that the synthetic catalysts of di-iron hydrogenase active site model are protonated either at the Fe-Fe bond for all terminal CO structures[219,220] or at the terminal position on one of the Fe for a bridging CO structures.[221-224] Gioia and coworkers[219] showed that $(\mu\text{-}S(CH_2)_3S)[Fe(CO)_3]_2$ with all terminal CO structures leads to hydrogen production at between Fe-Fe bond through an intermediate with one hydrogen on each iron. On the other hand, the hydrogen production path through the terminal hydride adducts is favorable in the density functional calculation of $[(CO)(CN)Fe_d(\mu\text{-}DTMA)(\mu\text{-}CO)Fe_p(CO)(CN)(SMe)]^-$ (DTMA = SCH_2NHCH_2S) complex,[222,223] in which DTMA can assist proton-transfer reaction to the distal iron.

More recently Pickett and coworkers synthesized $Fe_4[MeC(CH_2S)_3]_2(CO)_8$ (**1**), a catalyst in which [2Fe3S] units are fused by two bridging thiolate ligands (Figure 6.1c).[50,51] The catalyst undergoes two-electron reduction forming $\mathbf{1}^-$ and $\mathbf{1}^{2-}$ at -1.22 V and -1.58 V (vs. Fc/Fc^+) respectively, in CH_2Cl_2 solvent. Interestingly, unlike other Fe^IFe^I model and **1** structures that have all terminal CO,[45-49] the $\mathbf{1}^{2-}$ with equivalent oxidation state of Fe^IFe^I has bridging CO structure close to the structure of di-iron subsite in $\mathbf{H_{red}}$ state of di-iron hydrogenase. Moreover, when the 2,6-dimethylpyridinium acid ($LutH^+$) is used as a proton source, the rate of H_2 elimination for **1** after two-electron reduction and two-proton addition is significantly higher than that for $(\mu\text{-}S(CH_2)_3S)[Fe(CO)_3]_2$ and $Fe_2(\mu\text{-}PPh(CH_2)_3PPh)(CO)_6$.[51]

The presence of bridging CO structures and two di-iron subsites connecting by two thiolate ligands in the molecule of $\mathbf{1}^{2-}$ may open alternative reaction pathways when compares with those of di-iron models with all terminal CO for the proton reduction to H_2. In this article, we investigated the mechanism of proton- and electron-transfer in the H_2 production by **1**. The reduction potentials (E^0) and the proton-transfer free energies relative to $LutH^+$ of intermediates are calculated to compare with the applied reduction potentials. These density functional studies reveal the most probable intermediates and the H_2 production mechanism of the tetra-iron hexa-sulfur catalyst **1** and offer insight into the higher reactivity of $\mathbf{1}^{2-}$ for H_2 production.

6.2 Computational details

All calculations were performed with the Gaussian03 program.[132] The TPSS[225] density functional was used for all geometry optimization and frequency calculation. Stuttgart RSC 1997 ECP basis set[226] is used for Fe; LANL2DZdp[227] with effective core potential (ECP) is used for sulfur; 6-31G(d,p)[136-138] is used for C, O, and Fe-bound H; and 6-31G(d)[136-138] is used for other hydrogen atoms. All structures were fully optimized with default convergence criteria, and frequencies were calculated to ensure that there is no imaginary frequency for minima and only one imaginary frequency for transition states. Zero point energies and thermodynamic functions were calculated at 298.15 K and 1 atm. The solvation energies were calculated on the geometries from TPSS gas-phase optimizations by using CPCM[86,142] method with UAKS atomic radii and solvation parameters corresponding to CH_2Cl_2 ($\varepsilon = 8.93$).

6.2.1 Reduction potential (E^0) calculation

The thermodynamic cycle in Scheme 6.1 is used for calculation of reduction potential of A, $E^0(A)$. The reduction potential can be derived from ΔG^{EA}_{sol} in eq 6.1.

$$E^0(A) = -\Delta G^{EA}_{sol}/F \qquad ; \text{F = Faraday constant} \qquad (6.1)$$

$$\Delta G^{EA}_{sol} = \Delta G^{EA}_{gas} - \Delta G_{solv}(A) - \Delta G_{solv}(e^-) + \Delta G_{solv}(A^-) \qquad (6.2)$$

Scheme 6.1 Thermodynamic cycle of electron reduction.

$$\begin{tikzcd}
A_{gas} \arrow[d, "\Delta G_{solv}(A)"] & + & e^-_{gas} \arrow[r, "\Delta G^{EA}_{gas}"] \arrow[d, "\Delta G_{solv}(e^-)"] & A^-_{gas} \arrow[d, "\Delta G_{solv}(A^-)"] \\
A_{sol} & + & e^-_{sol} \arrow[r, "\Delta G^{EA}_{sol}"] & A^-_{sol}
\end{tikzcd}$$

The ΔG^{EA}_{sol} can be calculated from eq 6.2 where ΔG^{EA}_{gas} is the free energy change for the electron addition to A in gas phase and $\Delta G_{solv}(A)$, $\Delta G_{solv}(e^-)$, and $\Delta G_{solv}(A^-)$ are the solvation free energies of A, e^-, and A^-, respectively. The solvation free energy of e^- cannot be obtained directly from the calculation. However, we can eliminate this value by the calculation of relative reduction potential with a specific redox couple; here, we chose ferrocene/ferrocinium (Fc/Fc^+). The relative reduction potential of half reaction $A + e^- \rightarrow A^-$ vs. $Fc^+ + e^- \rightarrow Fc$ is reported as shown in eq 6.3.

$$E^0(A) \text{ vs } (Fc/Fc^+) = E^0(A) - E^0(Fc^+) \tag{6.3}$$

6.2.2 Proton-transfer free energy calculation

The acidity of a particular compound is usually determined by proton dissociation constant (pK_a). Thermodynamic cycle in Scheme 6.2 is used for the calculation of pK_a of AH^+, which can be derived from the free energy change upon proton loss, ΔG^{PL}_{sol} (eq 6.4).

Scheme 6.2 Thermodynamic cycle of proton dissociation.

$$\begin{tikzcd}
AH^+_{gas} \arrow[r, "\Delta G^{PL}_{gas}"] \arrow[d, "\Delta G_{solv}(AH^+)"] & A_{gas} \arrow[d, "\Delta G_{solv}(A)"] & + & H^+_{gas} \arrow[d, "\Delta G_{solv}(H^+)"] \\
AH^+_{sol} \arrow[r, "\Delta G^{PL}_{sol}"] & A_{sol} & + & H^+_{sol}
\end{tikzcd}$$

$$pK_a = \Delta G^{PL}_{sol} / 2.303RT \tag{6.4}$$

$$\Delta G^{PL}_{sol} = \Delta G^{PL}_{gas} + \Delta G_{solv}(A) + \Delta G_{solv}(H^+) - \Delta G_{solv}(AH^+) \tag{6.5}$$

In eq 6.5, only the proton solvation free energy, $\Delta G_{solv}(H^+)$, cannot be calculated directly by quantum mechanical method. Although, it can be deduced from the pK_a of acid known by experiment, to the best of our knowledge, neither of the proton solvation free energy or the pK_a of $LutH^+$ in CH_2Cl_2 solvent is known experimentally. Thus, we cannot calculate the pK_a of intermediate AH^+ and $LutH^+$ in CH_2Cl_2. Fortunately, giving the same information as pK_a of AH^+ and $LutH^+$, the free energy change to transfer a proton from $LutH^+$ to A can be used to compare the acidities between AH^+ and $LutH^+$ with no need for the proton solvation free energy as shown in eq 6.6 to eq 6.8.

$$LutH^+ \rightarrow Lut + H^+ \tag{6.6}$$

$$AH^+ \rightarrow A + H^+ \tag{6.7}$$

$$A + LutH^+ \rightarrow AH^+ + Lut \tag{6.8}$$

The $\Delta G^{PL}_{sol}(LutH^+)$ in eq 6.6 and $\Delta G^{PL}_{sol}(AH^+)$ in eq 6.7 can be converted to pK_a of $LutH^+$ and AH^+, respectively. When the pK_a of AH^+ is larger than $LutH^+$, $LutH^+$ is more acidic and the proton transfer from $LutH^+$ to A is more favorable than from AH^+ to Lut. On the other hand, the free energy difference in the process of proton transfer from $LutH^+$ to A (eq 6.8) can be derived by the subtraction of eq 6.7 from eq 6.6. From here, this free energy difference will be referred to as proton-transfer free energy of A. When the proton-transfer free energy of A is negative, $LutH^+$ is more acidic than AH^+. Just as when the pK_a of AH^+ is larger than $LutH^+$, the proton transfer from $LutH^+$ to A is favorable. Therefore, instead of calculated pK_a, we calculated the proton-transfer free energy of A, which is sufficient to compare the ability of intermediate A to be protonated by $LutH^+$ acid.

6.3 Results and discussion

We investigated the mechanism of hydrogen production by **1** in the presence of $LutH^+$ acid by beginning with the calculation of one- and two-electron reduced forms of **1** ($\mathbf{1}^-$ and $\mathbf{1}^{2-}$), then followed by the proton transfers to **1**, $\mathbf{1}^-$, and $\mathbf{1}^{2-}$, forms $\mathbf{H\text{-}1}^+$, **H-1**, and $\mathbf{H\text{-}1}^-$, respectively. We calculated alternative structures for $\mathbf{H\text{-}1}^x$ (x = 1+, 0, 1-, and 2-) based on the arrangement of the hydride and carbonyl ligands to determine the most stable structure of each species. Various structures of $\mathbf{2H\text{-}1}^x$ and $\mathbf{3H\text{-}1}^x$ (x = 1+, 0, and 1-) from the second and third proton addition are also examined. Then, the proton-transfer free energies of the most stable structures in each species are calculated. The reduction potentials of intermediates relative to ferrocenium (Fc^+) are also calculated to compare with the applied reduction potential. Finally, the overall scheme for hydrogen production is constructed to show the most probable pathways and intermediates in the catalytic cycle.

6.3.1 The structure determination of 1, 1^- and 1^{2-}

The calculated minimum structure of **1** has all terminal CO on both outer Fe atoms with C_i symmetry (Figure 6.2). The Mulliken atomic charges show that the outer Fe atoms (Fe_{ao} and Fe_{bo}) are more electron rich than the inner Fe atoms (Fe_{ai} and Fe_{bi}) (-0.873 and -0.552, respectively) (Table 6.1). The oxidation number of Fe in **1** could be assigned as $Fe^{1+}Fe^{2+}Fe^{2+}Fe^{1+}$. The Fe_{ao}-Fe_{ai} bond is 2.527 Å whereas Fe_{ai}-Fe_{bi} bond is slightly longer (2.618 Å) (Figure 6.2 and Table 6.2). We also determined a structure with one of the terminal CO on Fe_{ao} rotated to the semi-bridging position between Fe_{ao}-Fe_{ai} bond (**1b**). However, **1b** is a transition state, 9.00 kcal/mol less stable than **1**.

The first-electron reduction forms $\mathbf{1^-}$, which has a minimum structure similar to **1**, C_i symmetry and all terminal CO. The main difference is that the Fe_{ai}-Fe_{bi} bond distance in $\mathbf{1^-}$ lengthens to 2.900 Å, a change which results from the electron occupation of the LUMO of **1** that is Fe_{ai}-Fe_{bi} anti-bonding as in the previous calculations of Best, Pickett and coworkers.[51] The unpair electron in $\mathbf{1^-}$ is located mainly on inner Fe atoms; spin densities on Fe_{ai} and Fe_{bi} are 0.492 whereas spin densities on Fe_{ao} and Fe_{bo} are 0.023 (Table 6.3). The charge density rearranges such that at the outer Fe (-0.923) has even more electrons and the inner Fe (-0.423) has fewer electrons in spite of the added

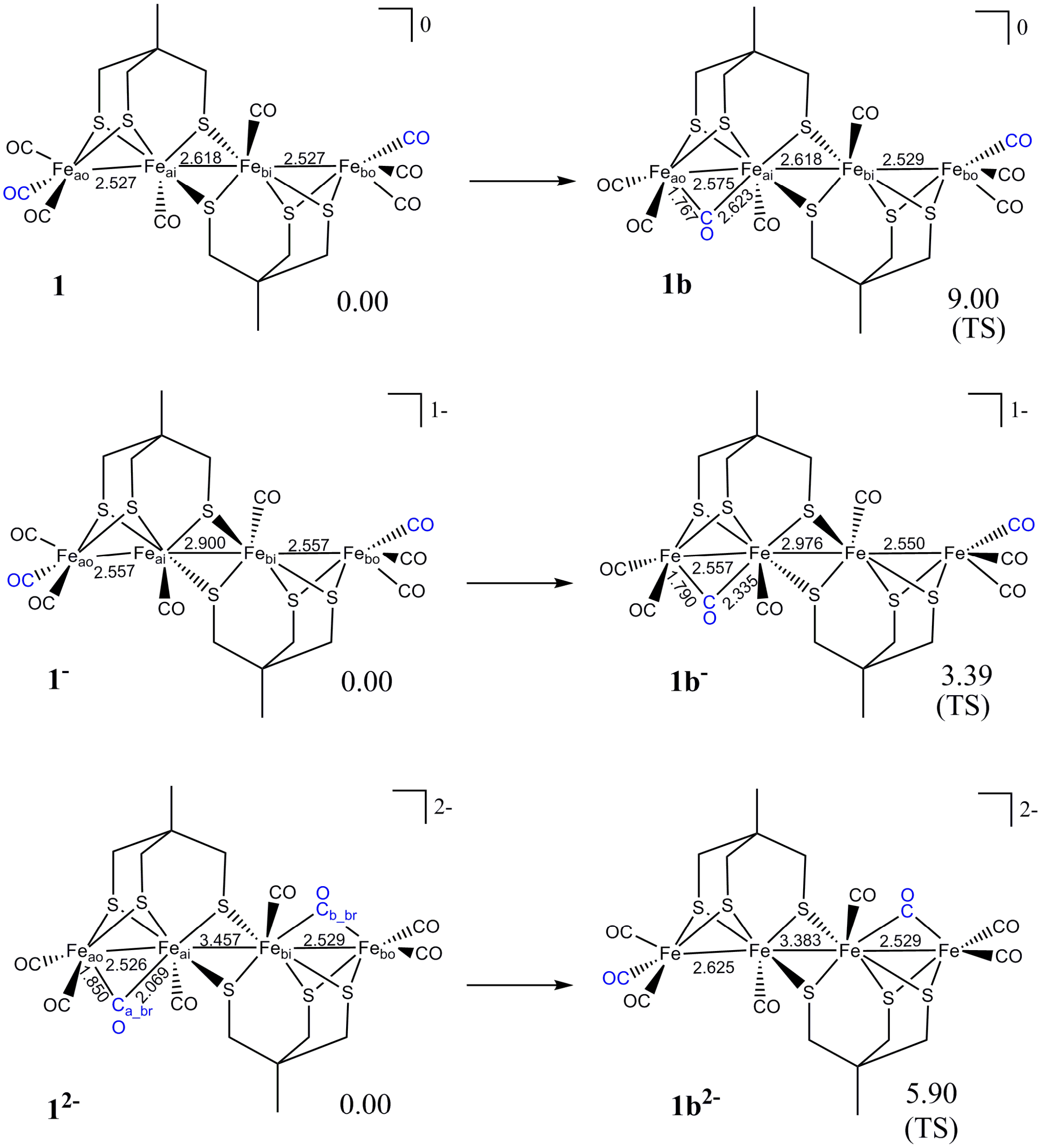

Figure 6.2 Rotation of carbonyl on one of the iron of **1**, **1$^-$**, and **1^{2-}**. The relative free energies in CH_2Cl_2 solution are given in kcal/mol. Selected bond distances are given in Å.

Table 6.1 Mulliken atomic charges of **nH-1^x** (n = 0, 1, 2, and 3; x = 2-, 1-, and 0).

	1	**1$^-$**	**1^{2-}**	**H-1(d)**	**H-1(b)$^-$**	**H-1(c)$^-$**	**H-1(c)$^{2-}$**	**2H-1(e)**	**2H-1(c)$^-$**	**2H-1(e)$^-$**	**3H-1(d)**	**3H-1(c)$^-$**
Fe_{ao}	-0.873	-0.923	-0.587	-0.863	-0.603	-0.862	-0.924	-0.993	-0.832	-1.033	-0.643	-1.029
Fe_{ai}	-0.552	-0.423	-0.700	-0.432	-0.660	-0.784	-0.752	-0.443	-0.778	-0.455	-0.718	-0.681
Fe_{bi}	-0.552	-0.423	-0.700	-0.617	-0.667	-0.736	-0.742	-0.563	-0.785	-0.564	-0.675	-0.738
Fe_{bo}	-0.873	-0.923	-0.587	-1.008	-1.019	-0.570	-0.626	-0.929	-0.686	-0.975	-0.969	-0.945
C_{a_br}			0.546		0.541	0.550	0.543		0.535		0.531	
C_{b_br}			0.546			0.545	0.552		0.559			
H_{a_br}								0.069		0.068		0.126
H_{b_br}				0.143	0.125			0.067		0.070	0.121	0.071
H_{ao_t1}						0.117	0.078		0.078		0.062	
H_{ao_t2}									0.087		0.066	
H_{bi_t}												0.150
H_{bo_t}												

Table 6.2 Selected geometry parameters of **nH-1**^{x} (n = 0, 1, 2, and 3; x = 2-, 1-, and 0).

	1	**1**$^-$	**1**$^{2-}$	**H-1(d)**	**H-1(b)**$^-$	**H-1(c)**$^-$	**H-1(c)**$^{2-}$	**2H-1(e)**	**2H-1(c)**$^-$	**2H-1(e)**$^-$	**3H-1(d)**	**3H-1(c)**$^-$
Fe_{ao}-Fe_{ai}	2.527	2.557	2.526	2.517	2.525	2.524	2.660	2.581	2.725	2.686	2.691	2.606
Fe_{ai}-Fe_{bi}	2.618	2.900	3.457	2.934	3.353	3.433	3.517	3.305	3.456	3.254	3.403	3.380
Fe_{bo}-Fe_{bi}	2.527	2.557	2.529	2.616	2.605	2.518	2.524	2.580	2.519	2.686	2.580	3.129
Fe_{ao}-C_{a_br}			1.850		1.822	2.107	2.071		2.386		2.258	
Fe_{ai}-C_{a_br}			2.069		2.130	1.898	1.911		1.821		1.844	
Fe_{bi}-C_{b_br}			2.071			2.136	2.067		2.120			
Fe_{bo}-C_{b_br}			1.850			1.820	1.851		1.823			
Fe_{ao}-H_{a_br}								1.700		1.735		1.731
Fe_{ai}-H_{a_br}								1.673		1.663		1.660
Fe_{bi}-H_{b_br}				1.703	1.678			1.673		1.662	1.672	1.773
Fe_{bo}-H_{b_br}				1.662	1.708			1.701		1.736	1.701	2.084
Fe_{ao}-H_{ao_t1}						1.506	1.548		1.876		1.830	
Fe_{ao}-H_{ao_t2}									1.874		1.835	
Fe_{bi}-H_{bi_t}												1.640
Fe_{bo}-H_{bo_t}												
H_{ao_t1}-H_{ao_t2}									0.777		0.781	
H_{bi_t}-H_{b_br}												0.857

Table 6.3 Mulliken spin densities of **nH-1**^{x} (n = 0, 1, 2, and 3; x = 2-, 1-, and 0).

	1^{-}	**H-1(d)**	**H-1(c)**$^{2-}$	**2H-1(c)**$^{-}$	**2H-1(e)**$^{-}$	**3H-1(d)**
Fe_{ao}	0.023	-0.058	0.311	0.754	0.187	0.849
Fe_{ai}	0.492	0.888	0.500	0.227	0.175	0.201
Fe_{bi}	0.492	0.230	0.013	0.020	0.298	0.005
Fe_{bo}	0.023	0.022	-0.001	-0.001	0.402	0.000
C_{a_br}			0.059	-0.014		-0.015
C_{b_br}			-0.001	0.000		
H_{a_br}					-0.017	
H_{b_br}		0.001			-0.014	0.000
H_{ao_t1}			0.056	0.010		0.029
H_{ao_t2}				0.045		0.010
H_{bi_t}						
H_{bo_t}						

electron residing mainly here. The oxidation number of Fe could be assigned as $Fe^{1+}Fe^{1.5+}Fe^{1.5+}Fe^{1+}$. The structure with semi-bridging CO on Fe_{ao}-Fe_{ai} bond (**1b**$^{-}$) is also determined to be a transition state, 3.39 kcal/mol less stable than **1**$^{-}$.

The second-electron reduction forms **1**$^{2-}$. Unlike **1** and **1**$^{-}$, the minimum structure of **1**$^{2-}$ has bridging COs on both Fe_{ao}-Fe_{ai} and Fe_{bo}-Fe_{bi} bonds with the Fe_{ai}-C_{a_br} bond (2.069 Å) slightly longer than the Fe_{ao}-C_{a_br} bond (1.850 Å). The Fe_{ai}-Fe_{bi} bond distance in **1**$^{2-}$ further extends to 3.457 Å corresponding to fully occupied Fe_{ai}- Fe_{bi} anti-bonding orbital. Now, the atomic charges on the outer Fe atoms (-0.587) are less negative than that on the inner Fe atoms (-0.700), which may derived from the electron back-bonding from bridging CO to the inner Fe; the oxidation number of Fe atoms could be assigned as $Fe^{1+}Fe^{1+}Fe^{1+}Fe^{1+}$. The structure with only one semi-bridging CO on one of the inner-outer Fe pairs, **1b^{2-}**, is also determined to be a transition state that is less stable than **1^{2-}** by 5.90 kcal/mol.

6.3.2 The first proton addition: H-1^{+}, H-1, H-1^{-}, and H-1^{2-}

The possible structures for **H-1^{x}** (x = 2-, 1-, 0, and 1+) based on various hydride and CO ligands arrangement are shown in Figure 6.3. The addition of the first proton to **1** forms **H-1^{+}**. **H-1(a)$^{+}$** and **H-1(c)$^{+}$** are found less stable than **H-1(d)$^{+}$** by 15.01 and 38.58 kcal/mol, respectively (Table 6.4). **H-1(b)$^{+}$** cannot be located; instead, the bridging CO rotated to the terminal position becoming **H-1(d)$^{+}$** after geometry optimization. The most stable structure, **H-1(d)$^{+}$**, has a hydride bridging (H_{b_br}) between Fe_{bi}-Fe_{bo} bond and all terminal CO on both outer Fe. The proton-transfer free energy of **1** to form **H-1(d)$^{+}$** is unfavorable by 21.46 kcal/mol (Table 6.5). Therefore, the formation of **H-1(d)$^{+}$** in the reaction is less likely because the **H-1(d)$^{+}$** is more acidic than LutH^{+}.

The addition of the first proton to **1^{-}** forms **H-1**. Like the cationic species, **H-1(a)** and **H-1(c)** are found less stable than **H-1(d)** (Table 6.4). Here, **H-1(b)** can be located but is still less stable than **H-1(d)** by 10.78 kcal/mol. Unlike the cationic species, the proton-transfer free energy of **1^{-}** forming **H-1(d)** is favorable by -6.25 kcal/mol (Table 6.5). Thus, the **H-1(d)** can be formed in the electrocatalytic reaction. The atomic charges on outer iron atoms are still more negative than that on inner iron atoms (Table 6.1); notably, the atomic charges on Fe_{bi}-Fe_{bo} pair with bridging hydride (H_{b_br}) is more negative than that on Fe_{ai}-Fe_{ao} pair without bridging hydride. In comparison to **1^{-}**, the

Fe_{bi}-Fe_{bo} bond and the Fe_{ai}-Fe_{bi} bond in **H-1(d)** lengthen by 0.06 Å and 0.03 Å, respectively, whereas Fe_{ai}-Fe_{ao} bond shortens by 0.04 Å (Table 6.2). Mulliken analysis shows that the unpair electron in **H-1(d)** is located mainly on inner Fe atoms with some on Fe_{bi} (0.230) and a larger amount on Fe_{ai} (0.888) (Table 6.3).

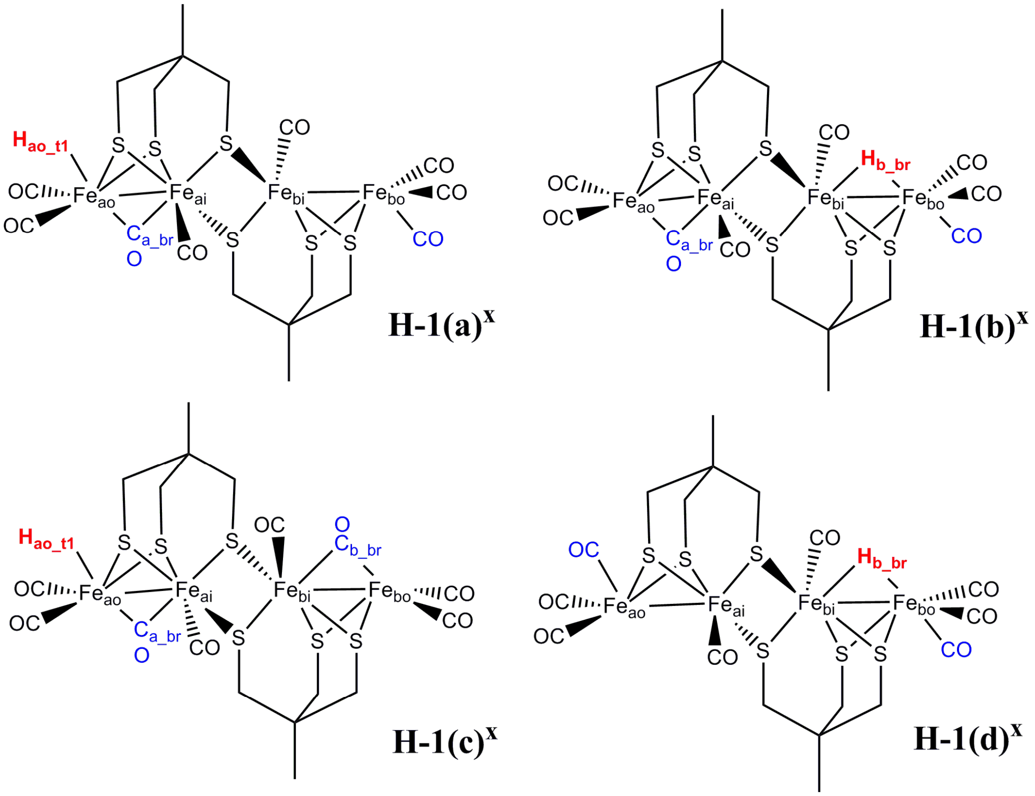

H-1(a)^x **H-1(b)^x** **H-1(c)^x** **H-1(d)^x**

Figure 6.3 Possible structures of **H-1^x** (x = 2-, 1-, 0, and 1+) based on different arrangements of various hydride and CO ligands. **H-1(a)^x** has a terminal hydride on Fe_{ao}, a bridging CO between Fe_{ao}-Fe_{ai} bond, and all terminal COs on Fe_{bo}. **H-1(b)^x** has a bridging hydride between Fe_{bo}-Fe_{bi} bond, all terminal COs on Fe_{bo}, and a bridging CO between Fe_{ao}-Fe_{ai} bond. **H-1(c)^x** has a terminal hydride on Fe_{ao} and a bridging CO between Fe_{ao}-Fe_{ai} bond and between Fe_{bo}-Fe_{bi} bond. **H-1(d)^x** has a bridging hydride between Fe_{bo}-Fe_{bi} bond and all terminal COs on both Fe_{ao} and Fe_{bo}.

Table 6.4 Solvation (CH_2Cl_2) corrected relative free energies of **H-1**^{x} (x = 2-, 1-, 0, and 1+) with respect to the most stable structure.

x	1+	0	1-	2-
H-1(a)	15.01	9.47	7.34(c)	n/l(b)
H-1(b)	n/l(a)	10.78	0.00	5.20
H-1(c)	38.58	17.12(c)	2.73	0.00
H-1(d)	0.00	0.00	5.52(c)	n/l(d)

(a) The structure is found as **H-1(d)**$^{+}$. (b) The structure is found as **H-1(c)**$^{2-}$. (c) These structures are transition states. (d) The structure is found as **H-1(b)**$^{2-}$.

Table 6.5 Proton-transfer free energies (ΔG^{PT}) of **nH-1**^{x} with CH_2Cl_2 solvation correction calculated from the reaction: LutH^{+} + **nH-1**^{x} --> Lut + **(n+1)H-1**$^{(x+1)}$ (n = 0, 1, and 2; x = 2-, 1-, and 0).

Reaction	ΔG^{PT}
1 + LutH^{+} -- > **H-1(d)**$^{+}$ + Lut	21.46
1^{-} + LutH^{+} -- > **H-1(d)** + Lut	-6.25
1^{2-} + LutH^{+} -- > **H-1(b)**$^{-}$ + Lut	-19.83
H-1(d) + LutH^{+} --> **2H-1(e)**$^{+}$ + Lut	15.44
H-1(b)$^{-}$ + LutH^{+} --> **2H-1(e)** + Lut	-10.36
H-1(c)$^{2-}$ + LutH^{+} --> **2H-1(c)**$^{-}$ + Lut	-21.77
H-1(c)$^{2-}$ + LutH^{+} --> **2H-1(e)**$^{-}$ + Lut	-22.73
2H-1(e) + LutH^{+} --> **3H-1(d)**$^{+}$ + Lut	34.03
2H-1(c)$^{-}$ + LutH^{+} --> **3H-1(d)** + Lut	-8.86
2H-1(e)$^{-}$ + LutH^{+} --> **3H-1(d)** + Lut	-7.90

The addition of the first proton to **1^{2-}** forms **H-1$^-$**. Here, **H-1(d)$^-$** is a transition state with an imaginary mode of CO rotating about the outer iron from terminal to bridging position; the same situation is also found for **H-1(a)$^-$**. **H-1(d)$^-$** and **H-1(a)$^-$** have higher energies than **H-1(b)$^-$**, the lowest energy structure by 5.52 and 7.34 kcal/mol, respectively, whereas **H-1(c)$^-$**, the structure with a terminal hydride (H_{ao_t1}) on Fe_{ao} and a bridging CO between the Fe_{ai}-Fe_{ao} bond and between the Fe_{bi}-Fe_{bo} bond, is only 2.73 kcal/mol above **H-1(b)$^-$**. The Fe-Fe bond distances in **H-1(c)$^-$** are not significantly different from those in **1^{2-}**. However, with a proton terminally bound at Fe_{ao}, the bridging CO in **H-1(c)$^-$** shifts from Fe_{ao} closer to Fe_{ai}; the Fe_{ao}-C_{a_br} bond is lengthened (from 1.850 to 2.107 Å) and the Fe_{ai}-C_{a_br} bond is shortened (from 2.069 to 1.898 Å).

Like the cationic and neutral complexes, the lowest energy structure for the anions, **H-1(b)$^-$**, also has a bridging hydride between Fe_{bi}-Fe_{bo} bond, but with a bridging CO between Fe_{ai}-Fe_{ao} bond, instead of all terminal COs as found in **H-1(d)$^+$** and **H-1(d)**. The proton-transfer free energy of **1^{2-}** forming **H-1(b)$^-$** is favorable by -19.83 kcal/mol (Table 6.5). In **H-1(b)$^-$**, the atomic charges on Fe_{bo}-Fe_{bi} pair (mainly on Fe_{bo}) with bridging hydride is more negative than that on Fe_{ai}-Fe_{ao} pair without bridging hydride (Table 6.1) as found in **H-1(d)** and the Fe_{bi}-Fe_{bo} bond is found longer than the Fe_{ai}-Fe_{ao} bond by 0.08 Å (Table 6.2). Interestingly, the Fe_{ai}-C_{a_br} bond in **H-1(b)$^-$** lengthens from the corresponding one in its unprotonated form, **1^{2-}**, by 0.06 Å leading to less electron back-bonding from bridging CO to Fe_{ai}; then the atomic charges on Fe_{ao} and Fe_{ai} in **H-1(b)$^-$** are more symmetric than that in **1^{2-}**.

The proton addition to **1**, **1$^-$**, and **1^{2-}** forms **H-1$^+$**, **H-1**, and **H-1$^-$**, respectively. Thus far, the structures of **H-1$^+$**, **H-1**, and **H-1$^-$** are calculated. However, **H-1^{2-}** can also be formed through the one-electron reduction of **H-1$^-$** (discussed later in the text). Therefore we also calculated **H-1^{2-}** structures. Here, **H-1(a)$^{2-}$** and **H-1(d)$^{2-}$** cannot be located; after their geometry optimizations, one of the CO ligands on outer iron rotates from terminal to bridging position becoming **H-1(c)$^{2-}$** and **H-1(b)$^{2-}$**, respectively. Unlike the anion, in the dianion, **H-1(c)$^{2-}$**, a terminal hydride complex is more stable than **H-1(b)$^{2-}$**, a bridging hydride complex, by -5.20 kcal/mol (Table 6.4). In comparison to **H-1(c)$^-$**, the dianion **H-1(c)$^{2-}$** has Fe_{ao}-Fe_{ai} and Fe_{ai}-Fe_{bi} bonds lengthen by 0.14 and 0.08 Å, respectively and the outer iron atoms, Fe_{ao} and Fe_{bo}, become more electron rich (Table 6.1). Note that the atomic charge on the hydride (H_{ao_t1}) in **H-1(c)$^{2-}$** also becomes more hydridic and would be expected to abstract a proton to form H_2 better than the hydride in **H-1(c)$^-$**.

6.3.3 The second proton addition: 2H-1$^+$, 2H-1, and 2H-1$^-$

The proton addition to **H-1**, **H-1$^-$**, and **H-1^{2-}** forms **2H-1$^+$, 2H-1, and 2H-1$^-$**, respectively. From results described above, the formation of **H-1$^+$** is unlikely; therefore, **2H-1^{2+}** structures were not examined. All possible structures of **2H-1^x** (x = 1-, 0, and 1+) are shown in Figure 6.4 based on the arrangements of two hydrides and CO ligands in the molecule; their relative energies are also shown in Table 6.6. Interestingly, the structure with a bridging hydride between Fe_{ai}-Fe_{ao} and between Fe_{bi}-Fe_{bo} bond and all terminal COs on Fe_{ao} and Fe_{bo}, **2H-1(e)**^{x} is the most stable structure in all cationic, neutral, and anionic **2H-1**^{x} species.

For the cation, **2H-1(e)**$^{+}$ is more stable than **2H-1(d)**$^{+}$, the structure with a hydride (H_{b_br}) bridging between Fe_{bi}-Fe_{bo} bond, a terminal hydride (H_{ao_t1}) on Fe_{ao}, and a bridging carbonyl between Fe_{ai}-Fe_{ao} bond, by 12.61 kcal/mol and more stable than other structures by 24-34 kcal/mol (Table 6.6). The proton-transfer free energy of **H-1(d)**, the lowest energy structure of **H-1**, to form **2H-1(e)**$^{+}$ is unfavorable by 15.44 kcal/mol (Table 6.5). Therefore, as for **H-1(d)**$^{+}$, the cationic species **2H-1(e)**$^{+}$ is unlikely to be formed in the reaction.

Table 6.6 Solvation (CH_2Cl_2) corrected relative free energies of **2H-1**^{x} (x = 1-, 0, and 1+) with respect to the most stable structure.

x	1+	0	1-
2H-1(a)	28.88	29.58	n/l(d)
2H-1(b)	26.17	11.53	5.60
2H-1(c)	33.93	n/l(a)	0.96
2H-1(d)	12.61	5.26	2.36
2H-1(e)	0.00	0.00	0.00
2H-1(f)	34.22	n/l(b)	7.63
2H-1(g)	24.08	n/l(c)	n/l(c)
2H-1(h)	n/c(e)	12.71	8.35

(a) The structure is found as **2H-1(g)**. (b) The structure is found as **2H-1(a)**. (c) The minimum structure is not found because H_2 dissociates from Fe center. (d) The structure is found as **2H-1(f)**$^{-}$. (e) The structure is not calculated.

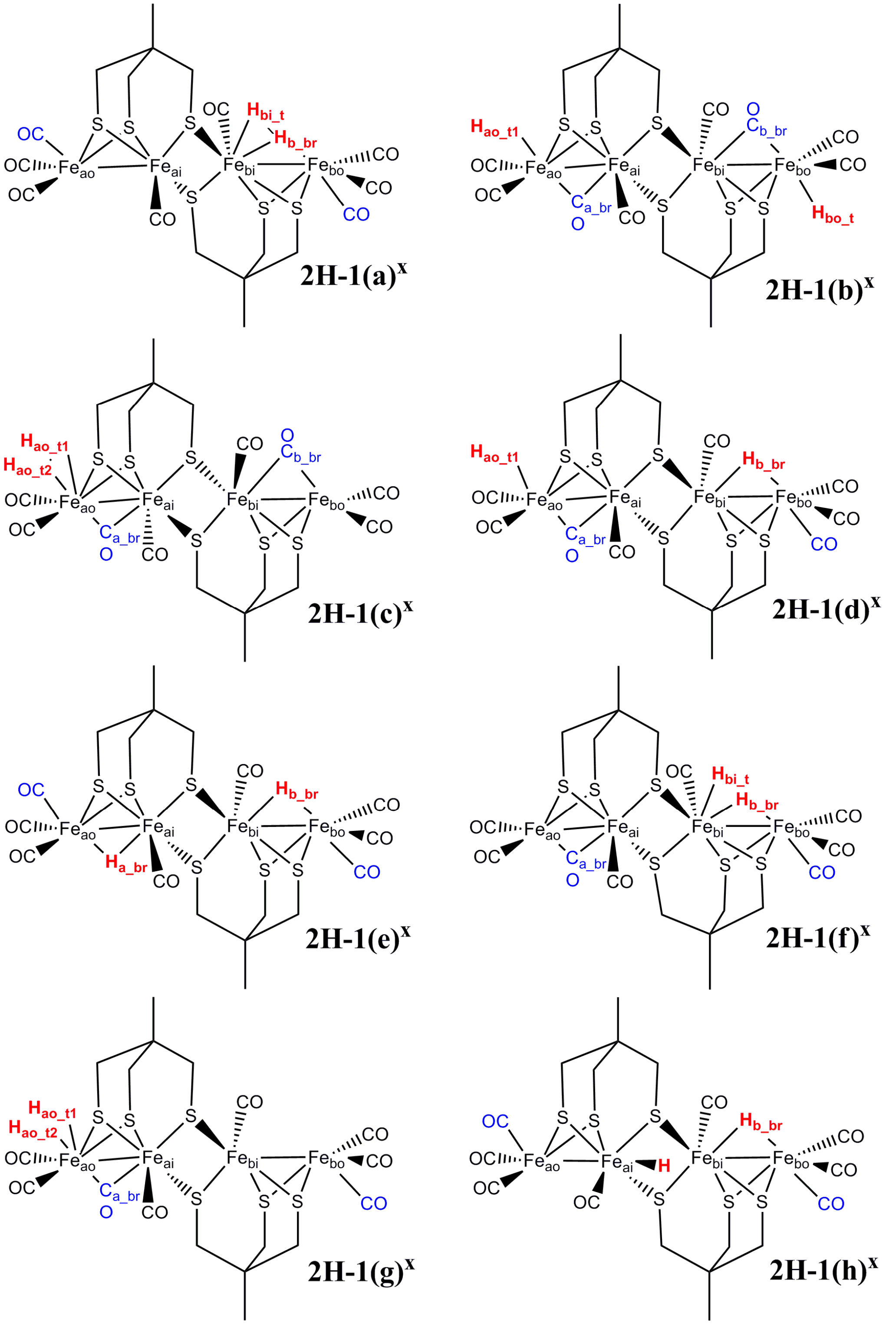

2H-1(a)^x

2H-1(b)^x

2H-1(c)^x

2H-1(d)^x

2H-1(e)^x

2H-1(f)^x

2H-1(g)^x

2H-1(h)^x

Figure 6.4 Possible structures of **2H-1^x** (x = 1-, 0, and 1+) based on different arrangements of hydrides and CO ligands.

In neutral species, **2H-1(d)** lies close to **2H-1(e)** but still has higher energy by 5.26 kcal/mol whereas other structures have higher energies than **2H-1(e)** by 11-30 kcal/mol. Here, **2H-1(c)** and **2H-1(f)** cannot be located; in their geometry optimizations, the bridging CO rotates to terminal position, becoming **2H-1(g)** and **2H-1(a)**, respectively. In addition, the hydrogen bound state of **2H-1(g)** is not found; during the geometry optimization, two hydrogen atoms on the same outer Fe in **2H-1(g)** forms a hydrogen molecule that dissociates from iron center.

The proton-transfer free energy of **H-1(b)**$^-$ to form **2H-1(e)** is favorable by -10.36 kcal/mol (Table 6.5). Because of the symmetry, the atomic charges in **2H-1(e)** are nearly equal for both the Fe_{ai}-Fe_{ao} and the Fe_{bi}-Fe_{bo} pair with more negative charge on the outer Fe than on the inner Fe (Table 6.1). The **2H-1(e)** could be an intermediate for hydrogen production and regeneration of **1**, as the free energy for hydrogen production is favorable by -8.91 kcal/mol (Table 6.7). However, the positions of two hydrogen atoms in **2H-1(e)** are too far from each other to directly form hydrogen molecule, i.e., we expect a high energy transition state for the process. To produce the hydrogen molecule, a bridging hydride on one of the inner-outer Fe pairs in **2H-1(e)** needs to come closer to the other hydrogen atom; the process could involve a bridging hydride transfer to the inner Fe closer to the other hydride through the **2H-1(h)** intermediate, for which the energy is higher than **2H-1(e)** by 12.71 kcal/mol. Although the overall energy for the hydrogen production by **2H-1(e)** is exergonic, the reaction proceeds necessarily through the higher energy intermediate **2H-1(h)**, and would be expected to have even higher energy transition state.

Table 6.7 Free energies for H_2 releasing (ΔG^{H2}) of **nH-1**^{x} with CH_2Cl_2 solvation correction calculated from the reaction: **nH-1**^{x} --> H_2 + (**n-2)H-1**^{x} (n = 2 and 3; x = 1- and 0).

Reaction	ΔG^{H2}
2H-1(e) -- > **1** + H_2	-8.91
2H-1(c)$^-$ --> **1**$^-$ + H_2	-20.77
2H-1(e)$^-$ --> **1**$^-$ + H_2	-19.81
3H-1(d) --> **H-1(d)** + H_2	-18.16
3H-1(c)$^-$ --> **H-1(b)**$^-$ + H_2	-29.60

For anionic species, **2H-1(d)**$^-$ lies even closer to the lowest energy structure **2H-1(e)**$^-$ (2.36 kcal/mol) (Table 6.6). However as described earlier, the hydrogen molecule cannot be produced directly from either **2H-1(e)**$^-$ or **2H-1(d)**$^-$ because two hydrogen atoms locate at different sites in these molecules; therefore, the reaction has to proceed through higher energy intermediates, such as **2H-1(h)**$^-$ (8.35 kcal/mol relative to **2H-1(e)**$^-$). On the other hand, the structures that support direct hydrogen production (collocation of both hydrogens), **2H-1(f)**$^-$ and **2H-1(c)**$^-$, can lead to two reaction paths: (i) **2H-1(f)**$^-$, the structure with one terminal hydride (H_{bi_t}) on Fe_{bi} and a bridging hydride (H_{b_br}) between Fe_{bi}-Fe_{bo} bond, produces hydrogen at Fe_{bi}-Fe_{bo} bond and (ii) **2H-1(c)**$^-$, the structure with two hydrogen atoms at the same outer Fe (Fe_{ao}) in the terminal position, produces hydrogen at a single iron, Fe_{ao}. Since the **2H-1(f)**$^-$ has higher energy than **2H-1(c)**$^-$ (7.63 and 0.96 kcal/mol relative to **2H-1(e)**$^-$, respectively), the hydrogen molecule is more likely to be produced at the single Fe_{ao} in **2H-1(c)**$^-$. The **2H-1(c)**$^-$ can be formed readily by direct proton transfer to **H-1(c)**$^{2-}$ (-21.77 kcal/mol) (Table 6.5) and can generate H_2 and **1**$^{-}$, releasing the energy of -20.77 kcal/mol (Table 6.7).

6.3.4 The third proton addition: 3H-1^{+}, 3H-1, 3H-1^{-}

The third proton addition can form different **3H-1**^{x} (x = 1-, 0, and 1+) structures as shown in Figure 6.5. The three hydrogen atoms in all **3H-1**^{x} molecules are located such that two hydrogen atoms are on the same di-iron subsite whereas the third hydrogen atom is on the other di-iron subsite. The cationic species **3H-1**$^{+}$ is formed by the proton addition to **2H-1**. The lowest energy structure, **3H-1(d)**$^{+}$ has two terminal hydrides (H_{ao_t1} and H_{ao_t2}) at the same outer Fe (Fe_{ao}) and a bridging hydride (H_{b_br}) between Fe_{bi}-Fe_{bo} bond. The structure with a terminal hydride on Fe_{bi} (H_{bi_t}), a bridging hydride between Fe_{bi}-Fe_{bo} bond (H_{b_br}) and between Fe_{ai}-Fe_{ao} bond (H_{a_br}), **3H-1(c)**$^{+}$ is 1.56 kcal/mol above **3H-1(d)**$^{+}$ while **3H-1(a)**$^{+}$ and **3H-1(b)**$^{+}$ have higher energies than **3H-1(d)**$^{+}$ by ~10 kcal/mol (Table 6.8). As in **H-1(d)**$^{+}$ and **2H-1(e)**$^{+}$, the cationic species **3H-1(d)**$^{+}$ is unlikely an intermediate in the reaction as the proton-transfer free energy of **2H-1(e)** to form **3H-1(d)**$^{+}$ is largely endergonic by 34.04 kcal/mol (Table 6.5).

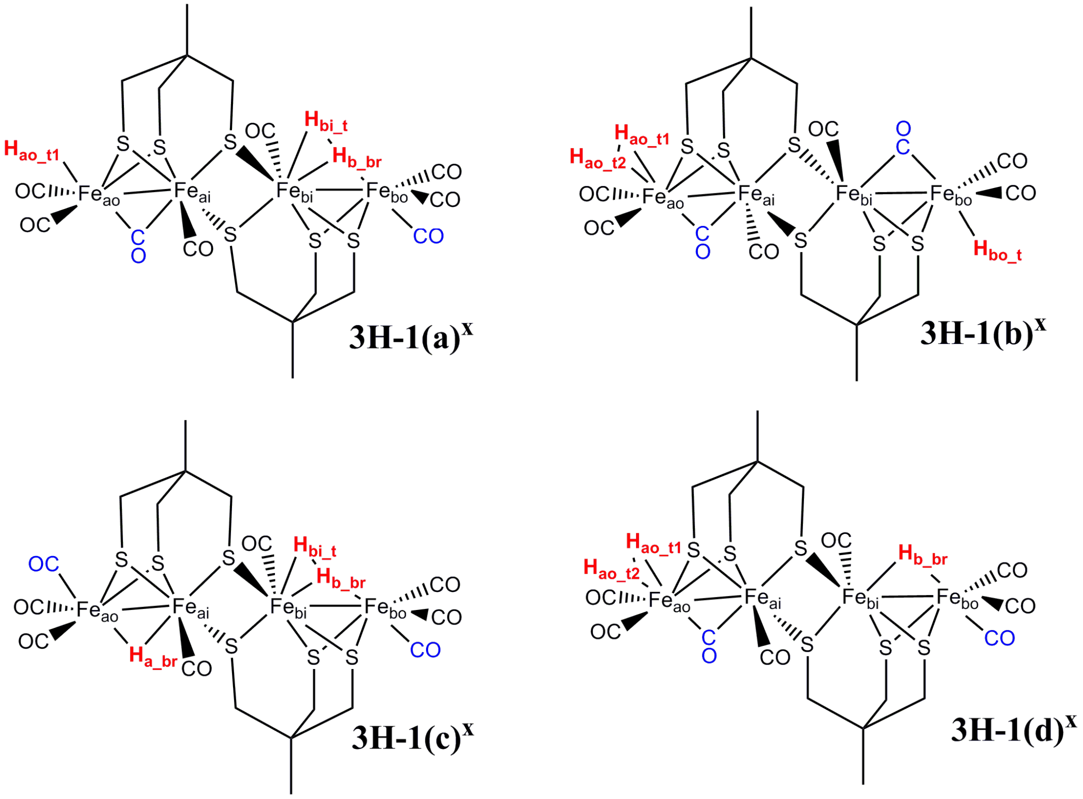

Figure 6.5 Possible structures of **3H-1**^{x} (x = 1-, 0, and 1+) based on different arrangements of hydrides and CO ligands.

Table 6.8 Solvation (CH_2Cl_2) corrected relative free energies of **3H-1**^{x} (x = 1-, 0, and 1+) with respect to the most stable structure.

x	1+	0	1-
3H-1(a)	10.75	13.05	3.47
3H-1(b)	10.66	5.76	n/l$^{(a)}$
3H-1(c)	1.56	7.16	0.00
3H-1(d)	0.00	0.00	n/l$^{(a)}$

(a) The minimum structure is not found because H_2 dissociates from Fe center.

From the relative free energies of four different structures in cationic and neutral species **3H-1**^{x} (x = +1 and 0), when one compares the structures that have the same position of two hydrogen atoms at one iron pair, the third hydrogen atom prefers to be at the bridging position between the other inner-outer Fe-Fe bond rather than at the terminal position on the outer Fe, i.e., **3H-1(d)**^{x} is more stable than **3H-1(b)**^{x} and **3H-1(c)**^{x} is more stable than **3H-1(a)**^{x} by a similar amount of free energy difference (Table 6.8). For the neutral species, **3H-1(d)** is still the lowest energy structure, more stable than **3H-1(c)** by -7.16 kcal/mol; once again, the hydrogen production would be more favorable at a single Fe_{ao} in **3H-1(d)** rather than at Fe_{bi}-Fe_{bo} bond in **3H-1(c)**. The **3H-1(d)** can be formed by the proton transfer of **2H-1(c)**$^-$, which is favorable by -8.86 kcal/mol (Table 6.5). Moreover, the hydrogen production of **3H-1(d)** releases H_2 and regenerates **H-1(d)**, exergonic by -18.16 kcal/mol (Table 6.7).

The electron reduction of neutral **3H-1** forms anionic species **3H-1**$^-$. For the anion, the bound states of **3H-1(b)**$^-$ and **3H-1(d)**$^-$, in which two terminal hydrogen atoms (H_{ao_t1} and H_{ao_t2}) are at the same outer iron (Fe_{ao}), cannot be located because during the geometry optimization the two hydrogen atoms form a hydrogen molecule that dissociates from the iron center. On the other hand, structures with two hydrogen atoms posed to form a hydrogen molecule at the Fe_{bi}-Fe_{bo} bond, **3H-1(a)**$^-$ and **3H-1(c)**$^-$, can be located as minima. **3H-1(c)**$^-$ is found more stable than **3H-1(a)**$^-$ by -3.47 kcal/mol, confirming that the third hydrogen atom prefers to be at bridging site between an Fe-Fe bond rather than at a terminal position on the outer Fe. Here, **3H-1(c)**$^-$ produces H_2 and regenerates **H-1(b)**$^-$ releasing the energy of -29.60 kcal/mol.

6.3.5 Calculated reduction potential

The calculated reduction potentials of **1** and **1^-** are -0.92 and -1.74 V (vs. Fc/Fc^+) (Table 6.9) whereas the experimental ones are -1.22 and -1.58 V, respectively (vs. Fc/Fc^+).[50,51] Within this error of the calculated reduction potential (~0.3 V), we can qualitatively determine the possible intermediates formed in the first applied potential that can reduce **1** to **1^-** and in the lower applied potential that can reduce **1^-** to **1^{2-}**. Unless specified otherwise, the reduction potential of a particular species refers to the reduction potential of that species vs. Fc/Fc^+.

Table 6.9 Calculated reduction potential (E^0 vs. Fc/Fc^+) with solvation (CH_2Cl_2) correction of selected structures of **$H\text{-}1^x$**, **$2H\text{-}1^x$**, and **$3H\text{-}1^x$** (x = 1-, 0, and 1+).

Reaction	E^0 (V)
1 + e^- --> **1^-**	-0.92
1^- + e^- --> **1^{2-}**	-1.74
H-1(d)$^+$ + e^- --> **H-1(d)**	0.28
H-1(d) + e^- --> **H-1(b)$^-$**	-1.15
H-1(b)$^-$ + e^- --> **H-1(c)$^{2-}$**	-1.81
2H-1(e)$^+$ + e^- --> **2H-1(e)**	-0.03
2H-1(e) + e^- --> **2H-1(c)$^-$**	-1.43
2H-1(e) + e^- --> **2H-1(e)$^-$**	-1.39
3H-1(d)$^+$ + e^- --> **3H-1(d)**	0.43
3H-1(d) + e^- --> **3H-1(c)$^-$**	-1.64

Calculated reduction potentials of the related intermediates in the lowest energy structures of each species are shown in Table 6.9. From their reduction potentials, all the cationic species **H-1(d)**$^+$, **2H-1(e)**$^+$, and **3H-1(d)**$^+$, can be reduced easily; however, as described earlier, these cationic species are too acidic to be formed with LutH$^+$ as the acid.

The spectroelectrochemical experiment[51] of **1** in the presence of LutH$^+$ acid showed that in the first applied potential that can reduce **1** at -1.22 V (vs. Fc/Fc$^+$), the concentration of LutH$^+$ decreases very slowly with **1**$^-$ as a main species in solution. In the lower applied potential that is sufficient to reduce **1**$^-$ to **1**$^{2-}$ at -1.58 V (vs. Fc/Fc$^+$), the concentration of LutH$^+$ decreases more rapidly. This observation is consistent with our calculation in that at the first reduction potential, apart from the reduction of **1** to **1**$^-$ (-0.92 V), only **H-1(d)** can be reduced (-1.15 V) to **H-1(b)**$^-$. Then, the proton addition to **H-1(b)**$^-$ forms **2H-1(e)**, which can produce H_2 necessarily through the higher energy intermediate **2H-1(h)**. Therefore, the hydrogen production in the first applied potential is inefficient.

Our calculation also showed that at the lower applied reduction potential not only **1**$^-$ can be reduced further to **1**$^{2-}$ (-1.74 V), more protonated intermediate species can be reduced than at the first potential. Within the range of the calculation error, **H-1(b)**$^-$ can be reduced further to **H-1(c)**$^{2-}$ (-1.81 V). Here, the anion **2H-1(c)**$^-$ can be formed by the protonation of **H-1(c)**$^{2-}$ and also by the electron reduction of **2H-1(e)** (-1.43 V). Then, **2H-1(c)**$^-$ is protonated to form **3H-1(d)**, which is reduced to **3H-1(c)**$^-$ at -1.64 V. These intermediates **2H-1(c)**$^-$, **3H-1(d)**, and **3H-1(c)**$^-$ produce H_2 favorably and regenerate initial species that can uptake more protons to start the reaction cycle again. Thus, at the lower applied potential, the concentration of $LutH^+$ is found decreasing much rapidly.

6.4 Conclusions

The thermodynamic relationships among **nH-1^x** (n = 0, 1, 2, and 3; x = 2-, 1-, 0, and 1+) shown in Figure 6.6 summarizes the important intermediates and reaction paths involving in the hydrogen production by tetra-iron hexa-sulfur complex, $Fe_4[MeC(CH_2S)_3]_2(CO)_8$ (**1**). At the first applied reduction potential that can reduce **1** to **1**$^-$ at -1.22 V (vs. Fc/Fc^+), **1**$^-$ can be protonated by $LutH^+$ acid at the inner-outer Fe-Fe bond to form **H-1(d)**, the structure with a bridging hydride and all terminal CO ligands. At this potential the reduction of **H-1(d)** can then occur; the structures with all terminal CO ligands, **H-1(d)**$^-$ and **H-1(a)**$^-$, are transition states whereas the structures with bridging CO ligands, **H-1(b)**$^-$ and **H-1(c)**$^-$, are minimum structures. The equilibrium structure, **H-1(b)**$^-$, with a bridging hydride, is slightly more stable (-2.73 kcal/mol) than **H-1(c)**$^-$, with a terminal hydride. Now, $LutH^+$ can protonate **H-1(b)**$^-$ and the equilibrium form, **2H-1(e)** with a bridging hydride on both inner-outer iron pairs. At this potential **2H-1(e)** cannot be reduced further. To produce H_2 and regenerate **1** from **2H-1(e)**, one of the bridging hydrides transfers to be solely on the inner iron to get close to the other bridging hydride through the higher energy intermediate **2H-1(h)** and possibly through even higher energy transition state. Therefore, the rate of $LutH^+$ consumption at the first applied potential is quite low as observed from the spectroelectrochemical experiment.

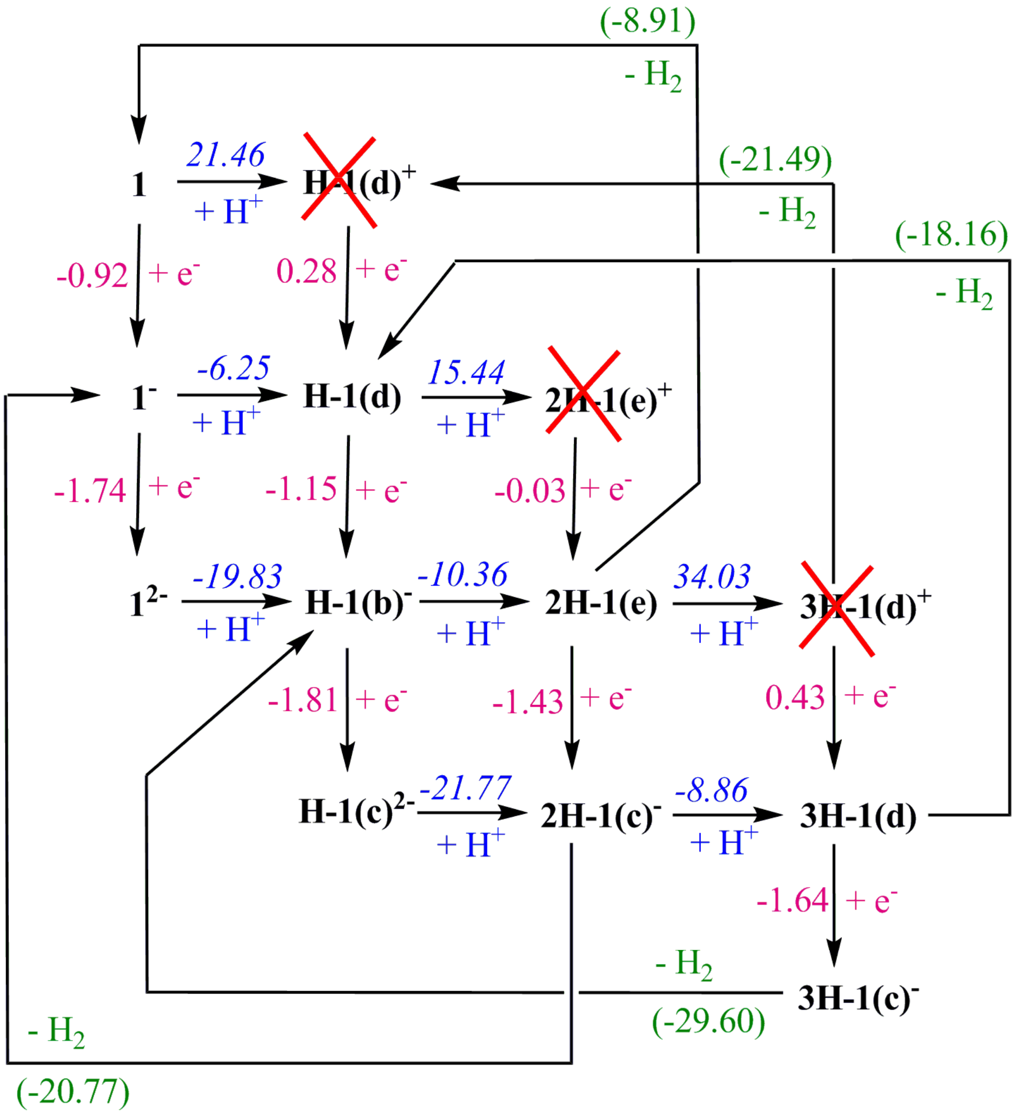

Figure 6.6 Thermodynamic relationships among $\mathbf{nH\text{-}1^x}$ (n = 0, 1, 2, and 3; x = 2-, 1-, 0, and 1+). The electron addition and calculated reduction potentials in V (vs. Fc/Fc^+) are shown on vertical arrow pointing down. The proton-transfer free energies in kcal/mol are shown on the horizontal arrow. The free energies for the H_2 releasing are shown in parenthesis in kcal/mol.

At the lower applied reduction potential that can reduce **1**$^-$ further to **1**$^{2-}$ at -1.58 V (vs. Fc/Fc$^+$), **1**$^{2-}$ is protonated to form **H-1(b)**$^-$, the species that can also be formed at the first applied potential but through the electron reduction of **H-1(d)**. Now, **H-1(b)**$^-$ can be reduced further to form **H-1(c)**$^{2-}$. Note that, for the dianion, **H-1(b)**$^{2-}$ with a bridging hydride is less stable (5.20 kcal/mol) than **H-1(c)**$^{2-}$ with a terminal hydride. Then, **2H-1(c)**$^-$ can be formed easily by protonation of **H-1(c)**$^{2-}$ and also by reduction of **2H-1(e)**. Unlike neutral species **2H-1(e)**, the anion **2H-1(c)**$^-$, with two hydrogen binding terminally on the same outer iron, can generates directly H_2 and **1**$^-$, exergonic by -20.77 kcal/mol. Importantly, **2H-1(c)**$^-$ can also be protonated to form **3H-1(d)**, in which two hydrogen atoms are also terminally bound to the same outer iron, Fe_{ao}, and the third hydrogen is bridging between Fe_{bi}-Fe_{bo} bond. The H_2 elimination and recovery of **H-1(d)** from **3H-1(d)** is exergonic by -18.16 kcal/mol. In addition, **3H-1(d)** can be reduced to **3H-1(c)**$^-$, in which two hydrogen atoms form hydrogen molecule at the inner-outer Fe-Fe bond. The hydrogen production and regeneration of **H-1(b)**$^-$ by **3H-1(c)**$^-$ is also exergonic. These results are consistent with the fact that the concentration of LutH$^+$ is decreased rapidly at this lower reduction potential.

Generally, it appears that a terminal hydride structure is more favorable than a bridging hydride structure in more highly reduced species and that the hydrogen production from **1** is mainly through the proton reduction on a single iron at the terminal position rather than on the Fe-Fe bond at the bridging position. Upon the two-electron reduction of **1**, the hydrogen production can occur spontaneously.

CHAPTER VII

SUMMARY AND CONCLUSIONS

The reaction mechanisms and electronic structures for palladium complexes that catalyzed the Heck reaction and iron enzyme models are studied by density functional theory. The solvent correction by continuum solvation model is applied as needed.

The theoretical study of the Heck reaction catalyzed by palladium with phosphine ligands showed that the reaction proceeds through monophosphinopalladium rather than diphosphinopalladium and olefin-bound monophosphinopalladium at the oxidative addition step of phenyl bromide. In the migratory insertion of phenyl group to the ethylene, β-hydride transfer/olefin elimination, and the catalyst recovery, the neutral pathway with bromide ion attached to palladium is more favorable than the cationic pathway with bromide ion dissociated from palladium, especially when the more bulky phosphines such as triphenylphosphine are involved.

The further study of the Heck reaction presented the pathways through dipalladium and "ligand-free" palladium intermediates. In the presence of phosphine, the Heck reaction proceeds through monopalladium monophosphine for the sterically demanding ligand, such as P^tBu_3, but preferably through dipalladium diphosphine for the less bulky ligand, such as PMe_3. In the absence of phosphine ligands, ethylene acts as a ligand to support palladium center through oxidative addition of phenyl bromide and migratory insertion steps; then the additional ligand, the second bromide, ligates to the open site to stabilize the low-coordinated palladium complex before releasing the styrene product and recovering the active palladium catalyst.

One of the factors that lead SOR and P450 into different reaction pathways is the different ground spin states of ferric hydroperoxo (Fe^{III}-OOH) intermediate for SOR and P450 models, which correspond to the difference in geometry parameters and electronic structures that assist protonation at different sites, (i) the protonation on proximal oxygen for SOR, leading to the formation of ferric hydrogen peroxide (Fe^{III}-HOOH) product, and (ii) the protonation on proximal oxygen for P450, leading to the O-O cleavage and the formation of oxo-ferryl (Fe^{IV}=O) and H_2O products. The other significant factor is the active site location in the enzyme. The solvent-exposed position of the active site in SOR gives a chance for the proximal and distal oxygen in Fe^{III}-HOOH model complex to form hydrogen bond with explicit water molecules, which stabilize the ground state of Fe^{III}-HOOH over the ground state of Fe^{IV}=O model complex.

The hydrogen production by di-iron hydrogenase model $Fe_4[MeC(CH_2S)_3]_2(CO)_8$ (**1**) is calculated. Reduced, doubly protonated complex, **2H-1(e)**, the first intermediate that can produce H_2 is formed in the lower applied potential. In the process of H_2 production, one of the bridging hydrides in **2H-1(e)** necessarily transfers to be solely on the inner iron to get close to the other bridging hydride through the higher energy intermediate, **2H-1(h)** (12.71 kcal/mol). Therefore, the rate of $LutH^+$ consumption in the lower applied potential is quite slow as observed from the spectroelectrochemical experiment. On the other hand, the intermediates formed in the second, more highly reductive, applied potential, the more highly reduced, doubly protonated anion, **2H-1(c)**$^-$, and the more highly reduced, triply protonated complexes, **3H-1(d)**, and **3H-1(c)**$^-$, can produce H_2 more easily than **2H-1(e)** in accordance with the more rapid decrease in concentration of LutH$^+$ observed when the higher reduction potential is applied.

7.1 Future study

a) The calculations predict the active species in the Heck reaction is Pd(0) complex. However, some starting catalysts used in the reaction are Pd(II) complexes. The precatalytic reaction mechanism to convert Pd(II) to Pd(0) complex still needs investigation.

b) The models of the active sites used in the study of SOR and P450 enzymes are truncated from the real enzyme structures. The effect from the protein backbone can also cause the different reactions in SOR and P450 enzymes. To include such the effect, the QM/MM calculation will be necessary.

c) Although Mulliken population analysis can be used to determine charge density and spin density of atoms in the molecule, its basic assumption may cause some errors. The more sophisticated methods for the population analysis should be used in the calculation of charge density and spin density for the iron active site models of SOR and P450 to compare with the results from the Mulliken population analysis.

d) There is a difficulty to determine the oxidation states of each iron centers in $Fe_4[MeC(CH_2S)_3]_2(CO)_8$. It would be useful to develop the method that can indicate the oxidation state for each metal in metal cluster accurately.

e) The calculation study of the proton dissociation constant (pK_a) for metal-hydride complexes in non-polar solvent (such as CH_2Cl_2 in Chapter VI) is quite rare compared to the study in polar solvent. It would be worthwhile to perform benchmarking calculation of pK_a for metal-hydride complexes and possibly organic molecules in non-polar solvent.

REFERENCES

(1) Crabtree, R. H. *The Organometallic Chemistry of the Transition Metals*; 4th ed.; John Wiley & Sons, Inc.: Hoboken, 2005.

(2) Spessard, G. O.; Miessler, G. L. *Organometallic Chemistry*; Prentice-Hall, Inc.: Upper Saddle River, NJ, 1996.

(3) Tsuji, J. *Palladium Reagents and Catalysts: New Perspectives for the 21st Century*; 2nd ed.; John Wiley & Sons Ltd: West Sussex, 2004.

(4) Li, J. J.; Gribble, G. W. *Palladium in Heterocyclic Chemistry: A Guide for the Synthetic Chemist*; 2nd ed.; Elsevier, 2006.

(5) Jaouen, G. *Bioorganometallics*; Wiley-VCH Verlag GmbH & Co.: Weinheim, 2002.

(6) Roat-Malone, R. M. *Bioinorganic Chemistry: A Short Course*; John Wiley & Sons, Inc.: Hoboken, 2002.

(7) Crichton, R. R. *Inorganic Biochemistry of Iron Metabolism*; Ellis Horwood Limited: West Sussex, 1991.

(8) Cundari, T. R. *Computational Organometallic Chemistry*; Marcel Dekker, Inc: New York, 2001.

(9) Diederich, F.; Stang, P. J. *Metal-catalyzed Cross-coupling Reactions*; Wiley-VCH Verlag GmbH: Weinheim, 1998.

(10) Heck, R. F.; Nolley, J. P. *Org. Chem.* **1972**, *37*, 2320-2322.

(11) Mizoroki, T.; Mori, K.; Ozaki, A. *Bull. Chem. Soc. Jpn.* **1971**, *44*, 581.

(12) Beletskaya, I. P.; Cheprakov, A. V. *Chem. Rev.* **2000**, *100*, 3009-3066.

(13) Witcombe, N. J.; Hii, K. K.; Gibson, S. E. *Tetrahedron* **2001**, *57*, 7449-7476.

(14) Ziegler Jr., C. B.; Heck, R. F. *J. Org. Chem.* **1978**, *43*, 2941-2946.

(15) Grushin, V. V. *Organometallics* **2000**, *19*, 1888-1900.

(16) Littke, A. F.; Fu, G. C. *Angew. Chem. Int. Ed.* **2002**, *41*, 4126-4211.

(17) Yin, L.; Liebscher, J. *Chem. Rev.* **2007**, *107*, 133-173.

(18) Phan, N. T. S.; Sluys, M. V. D.; Jones, C. W. *Adv. Synth. Catal.* **2006**, *348*, 609-679.

(19) Buchwald, S. L.; Mauger, C.; Mignani, G.; Scholz, U. *Adv. Synth. Catal.* **2006**, *348*, 23-39.

(20) Farina, V. *Adv. Synth. Catal.* **2004**, *346*, 1553-1582.

(21) Stambuli, J. P.; Buhl, M.; Hartwig, J. F. *J. Am. Chem. Soc.* **2002**, *124*, 9346-9347.

(22) Böhm, V. P. W.; Herrmann, W. A. *Chem. Eur. J.* **2001**, *7*, 4191-4197.

(23) Reetz, M. T.; Westermann, E. *Angew. Chem. Int. Ed.* **2000**, *39*, 165-168.

(24) Vries, A. H. M. d.; Parlevliet, F. J.; Vondervoort, L. S.-v. d.; Mommers, J. H. M.; Henderickx, H. J. W.; Walet, M. A. M.; Vries, J. G. d. *Adv. Synth. Catal.* **2002**, *344*, 996-1002.

(25) Vries, A. H. M. d.; Mulders, J. M. C. A.; Mommers, J. H. M.; Henderickx, H. J. W.; Vries, J. G. d. *Org. Lett.* **2003**, *5*, 3285-3288.

(26) Vries, J. G. d. *Dalton Trans.* **2006**, 421-429.

(27) Kohler, K.; Kleist, W.; Prockl, S. S. *Inorg Chem* **2007**, *46*, 1876-83.

(28) Reetz, M. T.; Vries, J. G. d. *Chem. Commun.* **2004**, 1559-1563.

(29) Schmidt, A. F.; Smirnov, V. V. *J. Mol. Catal. A: Chem.* **2003**, *203*, 75–78.

(30) Jenney, Jr., F. E.; Verhagen, M. F. J. M.; Cui, X.; Adams, M. W. W. *Science* **1999**, *286*, 306-309.

(31) Lombard, M.; Fontecave, M.; Touati, D.; Nivière, V. *J. Biol. Chem.* **2000**, *275*, 115-121.

(32) Yeh, A. P.; Hu, Y.; Francis E. Jenney, J.; Adams, M. W. W.; Rees, D. C. *Biochemistry* **2000**, *39*, 2499-2508.

(33) Kurtz, Jr., D. M. *Acc. Chem. Res.* **2004**, *37*, 902-908.

(34) Montellano, P. R. O. d. *Cytochrome P450: Structure, Mechanism, and Biochemistry*; 3 ed.; Plenum Press: New York, 2005.

(35) Schlichting, I.; Berendzen, J.; Chu, K.; Stock, A. M.; Maves, S. A.; Benson, D. E.; Sweet, R. M.; Ringe, D.; Petsko, G. A.; Sligar, S. G. *Science* **2000**, *287*, 1615-1622.

(36) Denisov, I. G.; Makris, T. M.; Sligar, S. G.; Schlichting, I. *Chem. Rev.* **2005**, *105*, 2253-2277.

(37) Shaik, S.; Kumar, D.; Visser, S. l. P. d.; Altun, A.; Thiel, W. *Chem. Rev.* **2005**, *105*, 2279-2328.

(38) Lubitz, W.; Reijerse, E.; Gastel, M. v. *Chem. Rev.* **2007**, *107*, 4331-4365.

(39) Siegbahn, P. E. M.; Tye, J. W.; Hall, M. B. *Chem. Rev.* **2007**, *107*, 4414-4435.

(40) Lacey, A. L. D.; Ferna´ndez, V. c. M.; Rousset, M.; Cammack, R. *Chem. Rev.* **2007**, *107*, 4304-4330.

(41) Peters, J. W.; Lanzilotta, W. N.; Lemon, B. J.; Seefeldt, L. C. *Science* **1998**, *282*, 1853-1858.

(42) Nicolet, Y.; Lacey, A. L. d.; Verne`de, X.; Fernandez, V. M.; Hatchikian, E. C.; Fontecilla-Camps, J. C. *J. Am. Chem. Soc.* **2001**, *123*, 1596-1601.

(43) Capon, J.-F. o.; Gloaguen, F. e. e.; Schollhammer, P.; Talarmin, J. *Coord. Chem. Rev.* **2005**, *249*, 1664–1676.

(44) Liu, X.; Ibrahim, S. K.; Tard, C. e.; Pickett, C. J. *Coord. Chem. Rev.* **2005**, *249*, 1641–1652.

(45) Schmidt, M.; Contakes, S. M.; Rauchfuss, T. B. *J. Am. Chem. Soc.* **1999**, *121*, 9736-9737.

(46) Zhao, X.; Georgakaki, I. P.; Miller, M. L.; Yarbrough, J. C.; Darensbourg, M. Y. *J. Am. Chem. Soc.* **2001**, *123*, 9710-9711.

(47) Barton, B. E.; Rauchfuss, T. B. *Inorg. Chem.* **2008**, *47*, 2261-2263.

(48) Justice, A. K.; Zampella, G.; Gioia, L. D.; Rauchfuss, T. B.; Vlugt, J. I. v. d.; Wilson, S. R. *Inorg. Chem.* **2007**, *46*, 1655-1664.

(49) Gloaguen, F. d. r.; Lawrence, J. D.; Rauchfuss, T. B. *J. Am. Chem. Soc.* **2001**, *123*, 9476-9477.

(50) Tard, C. d.; Liu, X.; Hughes, D. L.; Pickett, C. J. *Chem. Commun.* **2005**, 133-135.

(51) Cheah, M. H.; Tard, C. d.; Borg, S. J.; Liu, X.; Ibrahim, S. K.; Pickett, C. J.; Best, S. P. *J. Am. Chem. Soc.* **2007**, *129*, 11085-11092.

(52) Szabo, A.; Ostlund, N. S. *Modern Quantum Chemistry: Introduction to Advanced Electronic Structure Theory*; Dover Publications: Mineola, 1996.

(53) Jensen, F. *Introduction to Computational Chemistry*; John Wiley and Sons, Ltd.: West Sussex, 1999.

(54) Mulliken, R. S. *J. Chem. Phys.* **1962**, *36*, 3428.

(55) Slater, J. C. *Phys. Rev.* **1930**, *36*, 57.

(56) Boys, S. F. *Proc. R. Soc. A* **1950**, *200*, 540.

(57) Hehre, W. J.; Ditchfield, R.; Pople, J. A. *J. Chem. Phys.* **1972**, *56*, 2257.

(58) Frenking, G.; Antes, I.; Bohme, M.; Dapprioh, S.; Ehlers, A. W.; Jonas, V.; Nauhaus, A.; Otto, M.; Stegmann, R.; Veldkamp, A.; Vyboishchikov, S. F. *Rev. Comput. Chem.* **1996**, *8*, 63.

(59) Krauss, M.; Stevens, W. J. *Ann. Rev. Phys. Chem* **1984**, *35*, 357-385.

(60) Kahn, L. R.; Baybutt, P.; Truhlar, D. G. *J. Chem. Phys.* **1976**, *65*, 3826-3853.

(61) Christiansen, P. A.; Lee, Y. S.; Pitzer, K. S. *J. Chem. Phys.* **1979**, *71*, 4445-4450.

(62) Hay, P. J.; Wadt, W. R. *J. Chem. Phys.* **1985**, *82*, 270-283.

(63) Bergner, A.; Dolg, M.; Kuchle, W.; Stoll, H.; Preuβ, H. *Mol. Phys.* **1993**, *80*, 1431-1441.

(64) Hohenberg, P.; Kohn, W. *Phys. Rev.* **1964**, *136*, B864.

(65) Koch, W.; Holthausen, M. C. *A Chemist's Guide to Density Functional Theory*; WILEY-VCH Verlag GmbH: Weinheim, 2001.

(66) Kohn, W.; Sham, L. J. *Phys. Rev.* **1965**, *140*, A1133.

(67) Slater, J. C. *Phys. Rev.* **1951**, *81*, 385.

(68) Vosko, S. J.; Wilk, L.; Nusair, M. *Can. J. Phys.* **1980**, *58*, 1200.

(69) Becke, A. D. *Phys. Rev. A* **1988**, *38*, 3098.

(70) Perdew, J. P. *Phys. Rev. B* **1986**, *33*, 8822

(71) Perdew, J. P.; Chevary, J. A.; Vosko, S. H.; Jackson, K. A.; Pederson, M. R.; Singh, D. J.; Fiolhais, C. *Phys. Rev. B* **1992**, *46*, 6671.

(72) Lee, C.; Yang, W.; Parr, R. G. *Phys. Rev. B* **1988**, *37*, 785.

(73) Perdew, J. P.; Burke, K.; Ernzerhof, M. *Phys. Rev. Lett.* **1996**, *77*, 3865-3868.

(74) Tao, J. M.; Perdew, J. P.; Staroverov, V. N.; Scuseria, G. E. *Phys. Rev. Lett.* **2003**, *91*, 146401

(75) Becke, A. D. *J. Chem. Phys.* **1993**, *98*, 5648.

(76) Stephens, P. J.; Devlin, F. J.; Chabalowski, C. F.; Frisch, M. J. *J. Phys. Chem.* **1994**, *98*, 11623.

(77) Perdew, J. P.; Burke, K.; Ernzerhof, M. *Phys. Rev. Lett.* **1998**, *77*, 3865.

(78) Leach, A. R. *Molecular Modelling Principles and Applications*; 2nd ed.; Pearson Education Limited: Essex, 2001.

(79) Polak, E.; Ribiere, G. *Rev. Fr. Inf. Rech. Oper.* **1969**, *16-R1*, 35-43.

(80) Arrhenius, S. *Z. Physik. Chem.* **1889**, *4*, 226.

(81) Steinfeld, J. I.; Francisco, J. S.; Hase, W. L. *Chemical Kinetics and Dynamics*; 2 ed.; Prentice Hall: Upper Saddle River, NJ, 1999.

(82) Cramer, C. J. *Essentials of Computational Chemistry*; John Wiley & Sons, Ltd: West Sussex, 2002.

(83) Tomasi, J.; Mennucci, B.; Cammi, R. *Chem. Rev.* **2005**, *105*, 2999-3093.

(84) Miertus, S.; Scrocco, E.; Tomasi, J. *Chem. Phys.* **1981**, *55*, 117-129.

(85) Klamt, A.; Schuurmann, G. *J. Chem. Soc., Perkin Trans. 2* **1993**, 799 - 805.

(86) Barone, V.; Cossi, M. *J. Phys. Chem. A* **1998**, *102*, 1995.

(87) Pierotti, R. A. *J. Phys. Chem.* **1963**, *67*, 1840.

(88) Langlet, J.; Claverie, P.; Caillet, J.; Pullman, A. *J. Phys. Chem.* **1988**, *92*, 1617–1631.

(89) Sakoda, K.; Mihara, J.; Ichikawa, J. *Chem. Commun.* **2005**, 4684–4686.

(90) Arnold, L. A.; Luo, W.; Guy, R. K. *Org. Lett.* **2004**, *6*, 3005-3007.

(91) Dounay, A. B.; Overman, L. E.; Wrobleski, A. D. *J. Am. Chem. Soc.* **2005**, *127*, 10186-10187.

(92) Mo, J.; Xu, L.; Ruan, J.; Liu, S.; Xiao, J. *Chem. Commun.* **2006**, 3591–3593.

(93) Tu, T.; Hou, X.-L.; Dai, L.-X. *Org. Lett.* **2003**, *5*, 3651-3653.

(94) Mariampillai, B.; Herse, C.; Lautens, M. *Org. Lett.* **2005**, *7*, 4745-4747.

(95) Schmidt, B. *Chem. Commun.* **2003**, 1656–1657.

(96) Meijere, A. d.; Meyer, F. E. *Angew. Chem. Int. Ed.* **2004**, *33*, 2379-2411.

(97) Trzeciak, A. M.; Ziołkowski, J. J. *Coord. Chem. Rev.* **2007**, *251*, 1281-1293.

(98) Bedford, R. B.; Cazin, C. S. J.; Holder, D. *Coord. Chem. Rev.* **2004**, *248*, 2283-2321.

(99) Trzeciak, A. M.; Ziołkowski, J. J. *Coord. Chem. Rev.* **2005**, *249*, 2308-2322.

(100) Christmann, U.; Vilar, R. *Angew. Chem. Int. Ed.* **2005**, *44*, 366-374.

(101) Knowles, J. P.; Whiting, A. *Org. Biomol. Chem.* **2007**, *5*, 31–44.

(102) Cabri, W.; Candiani, I. *Acc. Chem. Res.* **1995**, *28*, 2-7.

(103) Littke, A. F.; Fu, G. C. *J. Org. Chem.* **1999**, *64*, 10-11.

(104) Shaughnessy, K. H.; Kim, P.; Hartwig, J. F. *J. Am. Chem. Soc.* **1999**, *121*, 2123-2132.

(105) Ehrentraut, A.; Zapf, A.; Beller, M. *Synlett* **2000**, 1589-1592.

(106) Portnoy, M.; Ben-David, Y.; Rousso, I.; Milstein, D. *Organometallics* **1994**, *13*, 3465-3479.

(107) Ohff, M.; Ohff, A.; van der Boom, M. E.; Milstein, D. *J. Am. Chem. Soc.* **1997**, *119*, 11687-11688.

(108) Morales-Morales, D.; Redón, R.; Yung, C.; Jensen, C. M. *Chem. Commun.* **2000**, 1619-1620.

(109) Herrmann, W. A.; Elison, M.; Fischer, J.; Köcher, C.; Artus, G. R. J. *Angew. Chem. Int. Ed.* **1995**, *34*, 2371-2374.

(110) Weskamp, T.; Böhm, V. P. W.; Herrmann, W. A. *J. Organomet. Chem.* **2001**, *585*, 348-352.

(111) Bedford, R. B. *Chem. Commun.* **2003**, 1787-1796.

(112) Bergbreiter, D. E.; Osburn, P. L.; Liu, Y.-S. *J. Am. Chem. Soc.* **1999**, *121*, 9531-9538.

(113) Blackmond, D. G.; Schultz, T.; Mathew, J. S.; Loew, C.; Rosner, T.; Pfaltz, A. *Synlett* **2006**, *18*, 3135–3139.

(114) Amatore, C.; Pfluger, F. *Organometallics* **1990**, *9*, 2276-2282.

(115) Fauvarque, J.-F.; Pfluger, F.; Troupel, M. *J. Organomet. Chem.* **1981**, *208*, 419-427.

(116) Littke, A. F.; Dai, C. Y.; Fu, G. C. *J. Am. Chem. Soc.* **2000**, *122*, 4020.

(117) Stumbuli, J. P.; Incarvito, C. D.; Buehl, M.; Hartwig, J. F. *J. Am. Chem. Soc.* **2004**, *126* 1184-1194.

(118) Kiewel, K.; Liu, Y.; Bergbreiter, D. E.; Sulikowski, G. A. *Tetrahedron Letters* **1999**, *40*, 8945-8948.

(119) Amatore, C.; Carre´, E.; Jutand, A.; Medjour, Y. *Organometallics* **2002**, *21*, 4540-4545.

(120) Samsel, E. G.; Norton, J. R. *J. Am. Chem. Soc.* **1984**, *106*, 5505-5512.

(121) Cavell, K. J. *Coord. Chem. Rev.* **1996**, *155*, 209-243.

(122) Thorn, D. L.; Hoffmann, R. *J. Am. Chem. Soc.* **1978**, *100*, 2079-2090.

(123) Lin, B.-L.; Liu, L.; Fu, Y.; Luo, S.-W.; Chen, Q.; Guo, Q.-X. *Organometallics* **2004**, *23*, 2114-2123.

(124) Cabri, W.; Candiani, I.; Bedeschi, A.; Penco, S. *J. Org. Chem.* **1992**, *57*, 1481-1486.

(125) Albert, K.; Gisdakis, P.; Rösch, N. *Organometallics* **1998**, *17*, 1608-1616.

(126) Sundermann, A.; Uzan, O.; Martin, J. M. L. *Chem. Eur. J.* **2001**, *7*, 1703-1711.

(127) Senn, H. M.; Ziegler, T. *Organometallics* **2004**, *23*, 2980-2988.

(128) Goossen, L. J.; Koley, D.; Hermann, H.; Thiel, W. *Chem. Commun.* **2004**, 2141-2143.

(129) Goossen, L. J.; Koley, D.; Hermann, H. L.; Thiel, W. *Organometallics* **2005**, *24*, 2398-2410.

(130) Ahlquist, M.; Norrby, P.-O. *Organometallics* **2007**, *26*, 550-553.

(131) Ahlquist, M.; Fristrup, P.; Tanner, D.; Norrby, P.-O. *Organometallics* **2006**, *25*, 2066-2073.

(132) Frisch, M. J.; Trucks, G. W.; Schlegel, H. B.; Scuseria, G. E.; Robb, M. A.; Cheeseman, J. R.; Montgomery, J. A., Jr.; Vreven, T.; Kudin, K. N.; Burant, J. C.; Millam, J. M.; Iyengar, S. S.; Tomasi, J.; Barone, V.; Mennucci, B.; Cossi, M.; Scalmani, G.; Rega, N.; Petersson, G. A.; Nakatsuji, H.; Hada, M.; Ehara, M.; Toyota, K.; Fukuda, R.; Hasegawa, J.; Ishida, M.; Nakajima, T.; Honda, Y.; Kitao, O.; Nakai, H.; Klene, M.; Li, X.; Knox, J. E.; Hratchian, H. P.; Cross, J. B.; Adamo, C.; Jaramillo, J.; Gomperts, R.; Stratmann, R. E.; Yazyev, O.; Austin, A. J.; Cammi, R.; Pomelli, C.; Ochterski, J. W.; Ayala, P. Y.; Morokuma, K.; Voth, G. A.; Salvador, P.; Dannenberg, J. J.; Zakrzewski, V. G.; Dapprich, S.; Daniels, A. D.; Strain, M. C.; Farkas, O.; Malick, D. K.; Rabuck, A. D.; Raghavachari, K.; Foresman, J. B.; Ortiz, J. V.; Cui, Q.; Baboul, A. G.; Clifford, S.; Cioslowski, J.; Stefanov, B. B.; Liu, G.; Liashenko, A.; Piskorz, P.;

Komaromi, I.; Martin, R. L.; Fox, D. J.; Keith, T.; Al-Laham, M. A.; Peng, C. Y.; Nanayakkara, A.; Challacombe, M.; Gill, P. M. W.; Johnson, B.; Chen, W.; Wong, M. W.; Gonzalez, C.; Pople, J. A. *Gaussian 03, Revision B.4, B.5, and C.1*; Gaussian, Inc.: Pittsburgh, PA, 2003.

(133) Hay, P. J.; Wadt, W. R. *J. Chem. Phys.* **1985**, *82*, 270-283.

(134) Hay, P. J.; Wadt, W. R. *J. Chem. Phys.* **1985**, *82*, 299-310.

(135) Couty, M.; Hall, M. B. *J. Comput. Chem.* **1996**, *17*, 1359-1370.

(136) Hariharan, P. C.; Pople, J. A. *Theor. Chim. Acta* **1973**, *28*, 213-222.

(137) Petersson, G. A.; Al-Laham, M. A. *J. Chem. Phys.* **1991** *94*, 6081-6090.

(138) Petersson, G. A.; Bennett, A.; Tensfeldt, T. G.; Al-Laham, M. A.; Shirley, W. A.; Mantzaris, J. *J. Chem. Phys.* **1988**, *89*, 2193-2218.

(139) Jong, G. T. d.; Geerke, D. P.; Diefenbach, A.; Bickelhaupt, F. M. *Chem. Phys.* **2005**, *313*, 261–270.

(140) Becke, A. D. *J. Chem. Phys.* **1993**, *98*, 5648.

(141) Lee, C.; Yang, W.; Parr, R. G. *Phys. Rev. B* **1988**, *37*, 785.

(142) Cossi, M.; Rega, N.; Scalmani, G.; Barone, V. *J. Comp. Chem.* **2003**, *24*, 669-681.

(143) Wan, S.; Stote, R. H.; Karplus, M. *J. Chem. Phys.* **2004**, *121*, 9539.

(144) When we optimize $Pd(PH_3)_2$ without density fitting function and tighten the cutoffs in the convergence criteria, the P-Pd-P angle is 179.5^o.

(145) Brown, J. M.; Cooley, N. A. *Organometallics* **1990**, *9*, 353.

(146) Rincon, E.; Toro-Labbe, A. *Chem. Phys. Lett.* **2007**, *438*, 93.

(147) Casado, A. L.; Espinet, P. *Organometallics* **1998**, *17*, 954-959.

(148) Jeffery, T. *Tetrahedron Lett.* **1985**, *26*, 2667-2670.

(149) Reetz, M. T.; Westermann, E.; Lohmer, R.; Lohmer, G. *Tetrahedron Lett.* **1998**, *39*, 8449-8452.

(150) Ariafard, A.; Lin, Z. *Organometallics* **2006**, *25*, 4030-4033.

(151) Lam, K. C.; Marder, T. B.; Lin, Z. *Organometallics* **2007**, *26*, 758-760.

(152) Surawatanawong, P.; Fan, Y.; Hall, M. B. *J. Organomet. Chem.* **2008**, *693*, 1552-1563.

(153) Ahlquist, M.; Fabrizi, G.; Cacchi, S.; Norrby, P.-O. *J. Am. Chem. Soc.* **2006**, *128*, 12785-12793.

(154) Ahlquist, M. r.; Fabrizi, G.; Cacchi, S.; Norrby, P.-O. *Chem. Commun.* **2005**, 4196–4198.

(155) Jain, V. K.; Jain, L. *Coord. Chem. Rev.* **2005**, *249*, 3075–3197.

(156) Murahashi, T.; Kanehisa, N.; Kai, Y.; Otani, T.; Kurosawa, H. *Chem. Commun.* **1996**, 825.

(157) Ogoshi, S.; Tsutsumi, K.; Ooi, M.; Kurosawa, H. *J. Am. Chem. Soc.* **1995**, *117*, 10415-10416.

(158) Dura-Vila, V.; Mingos, D. M. P.; Vilar, R.; White, A. J. P.; Williams, D. J. *J. Organo. Chem.* **2000**, *600*, 198-205.

(159) Vilar, R.; Mingos, D. M. P.; Cardin, C. J. *J. Chem. Soc., Dalton Trans.* **1996**, 4313-4314.

(160) Budzelaar, P. H. M.; van Leeuwen, P. W. V. M.; Robeek, C. F.; Orpen, A. G. *Organometallics* **1992**, *11*, 23-25.

(161) Kovacs, J. A. *Chem. Rev.* **2004**, *104*, 825-848.

(162) Kovacs, J. A.; Brines, L. M. *Acc. Chem. Res.* **2007**, *40*, 501-509.

(163) Kovacs, J. A. *Science* **2003**, *299*, 1024-1025.

(164) Francis E. Jenney, J.; Verhagen, M. F. J. M.; Cui, X.; Adams, M. W. W. *Science* **1999**, *286*, 306-309.

(165) Lombard, M.; Fontecave, M.; Touati, D.; Nivière, V. *J. Biol. Chem.* **2000**, *275*, 115-121.

(166) Imlay, J. A. *J Biol Inorg Chem* **2002**, *7*, 659–663.

(167) Sono, M.; Roach, M. P.; Coulter, E. D.; Dawson, J. H. *Chem. Rev.* **1996**, *96*, 2841-2887.

(168) Adams, M. W. W.; Jr., F. E. J.; Clay, M. D.; Johnson, M. K. *J Biol Inorg Chem* **2002**, *7*, 647-652.

(169) Kurtz Jr., D. M. *Acc. Chem. Res.* **2004**, *37*, 902-908.

(170) Kurtz Jr., D. M.; Coulter, E. D. *J Biol Inorg Chem* **2002**, *7*, 653–658.

(171) Imai, M.; Shimada, H.; Watanabe, Y.; Matsushima-Hibaya, Y.; Makino, R.; Koga, H.; Horiuchi, T.; Ishimura, Y. *Proc. Natl. Acad. Sci.* **1989**, *86*, 7823-7827.

(172) Harris, D. L.; Loew, G. H. *J. Am. Chem. Soc.* **1998**, *120*, 8941-8948.

(173) Hata, M.; Hirano, Y.; Hoshino, T.; Nishida, R.; Tsuda, M. *J. Phys. Chem. B* **2004**, *108*, 11189-11195.

(174) Bach, R. D.; Dmitrenko, O. *J. Am. Chem. Soc.* **2006**, *128*, 1474-1488.

(175) Guallar, V.; Friesner, R. A. *J. Am. Chem. Soc.* **2004**, *126*, 8501-8508.

(176) Kumar, D.; Hirao, H.; Visser, S. P. d.; Zheng, J.; Wang, D.; Thiel, W.; Shaik, S. *J. Phys. Chem. B* **2005**, *109*, 19946-19951.

(177) Zheng, J.; Wang, D.; Thiel, W.; Shaik, S. *J. Am. Chem. Soc.* **2006**, *128*, 13204-13215.

(178) Kamachi, T.; Yoshizawa, K. *J. Am. Chem. Soc.* **2003**, *125*, 4652-4661.

(179) Silaghi-Dumitrescu, R.; Silaghi-Dumitrescu, I.; Coulter, E. D.; Donald M. Kurtz, J. *Inorg. Chem.* **2003**, *42*, 446-456.

(180) Yang, T.-C.; McNaughton, R. L.; Clay, M. D.; Francis E. Jenney, J.; Krishnan, R.; Donald M. Kurtz, J.; Adams, M. W. W.; Johnson, M. K.; Hoffman, B. M. *J. Am. Chem. Soc.* **2006**, *128*, 16566-16578.

(181) Dey, A.; Francis E. Jenney, J.; Adams, M. W. W.; Johnson, M. K.; Hodgson, K. O.; Hedman, B.; Solomon, E. I. *J. Am. Chem. Soc.* **2007**, *129*, 12418-12431.

(182) Clay, M. D.; Francis E. Jenney, J.; Hagedoorn, P. L.; George, G. N.; Adams, M. W. W.; Johnson, M. K. *J. Am. Chem. Soc.* **2002**, *124*, 788-805.

(183) Coelho, A. V.; Matias, P.; Fülöp, V.; Thompson, A.; Gonzalez, A.; Carrondo, M. A. *J. Biol. Inorg. Chem.* **1997**, *2*, 680–689

(184) Santos-Silva, T.; Trincao, J.; Carvalho, A. L.; Bonifacio, C.; Auchere, F.; Raleiras, P.; Moura, I.; Moura, J. J.; Romao, M. J. *J Biol Inorg Chem* **2006**, *11*, 548-558.

(185) Katona, G.; Carpentier, P.; Nivière, V.; Amara, P.; Adam, V.; Ohana, J.; Tsanov, N.; Bourgeois, D. *Science* **2007**, *316*, 449-453.

(186) Ghosh, A. *J. Biol. Inorg. Chem.* **2006**, *11*, 712–724.

(187) Swart, M.; Groenhof, A. R.; Ehlers, A. W.; Lammertsma, K. *J. Phys. Chem. A* **2004**, *108*, 5479-5483.

(188) Mathe´, C.; Mattioli, T. A.; Horner, O.; Lombard, M.; Latour, J.-M.; Fontecave, M.; re, V. N. *J. Am. Chem. Soc.* **2002**, *124*, 4966-4967.

(189) Davydov, R.; Makris, T. M.; Kofman, V.; Werst, D. E.; Sligar, S. G.; Hoffman, B. M. *J. Am. Chem. Soc.* **2001**, *123*, 1403-1415.

(190) Ogliaro, F.; Cohen, S.; Visser, S. P. d.; Shaik, S. *J. Am. Chem. Soc.* **2000**, *122*, 12892-12893.

(191) Schoneboom, J. C.; Lin, H.; Reuter, N.; Thiel, W.; Cohen, S.; Ogliaro, F. o.; Shaik, S. *J. Am. Chem. Soc.* **2002**, *124*, 8142-8151.

(192) Altun, A.; Shaik, S.; Thiel, W. *J. Am. Chem. Soc.* **2007**, *129*, 8978-8987.

(193) Ogliaro, F. o.; Filatov, M.; Shaik, S. *Eur. J. Inorg. Chem.* **2000**, 2455-2458.

(194) Liu, X.; Wang, Y.; Han, K. *J. Biol. Inorg. Chem.* **2007**, *12*, 1073-1081.

(195) Pereira, A. S.; Tavares, P.; Moura, I.; Moura, J. J. G.; Huynh, B. H. *J. Am. Chem. Soc.* **2001**, *123*, 2771-2782.

(196) Popescu, C. V.; Mu1nck, E. *J. Am. Chem. Soc.* **1999**, *121*, 7877-7884.

(197) Yaropolov, A. I.; Karyakin, A. A.; Varfolomeev, S. D.; Berezin, I. V. *Bioelectrochem. Bioenerg.* **1984**, *12*, 267-277.

(198) Tye, J. W.; Hall, M. B.; Darensbourg, M. Y. *Proc. Nat. Acad. Sci.* **2005**, *102*, 16911–16912.

(199) Karyakin, A. A.; Morozov, S. V.; Karyakina, E. E.; Varfolomeyev, S. D.; Zorin, N. A.; Cosnier, S. *Electrochem. Commun.* **2002**, *4*, 417-420.

(200) Tye, J. W.; Darensbourg, M. Y.; Hall, M. B. *Inorg. Chem.* **2008**, *47*, 2380-2388.

(201) Tye, J. W.; Lee, J.; Wang, H.-W.; Mejia-Rodriguez, R.; Reibenspies, J. H.; Hall, M. B.; Darensbourg, M. Y. *Inorg. Chem.* **2005**, *44*, 5550-5552.

(202) Liu, T.; Darensbourg, M. Y. *J. Am. Chem. Soc.* **2007**, *129*, 7008-7009.

(203) Thomas, C. M.; Liu, T.; Hall, M. B.; Darensbourg, M. Y. *Inorg. Chem.* **2008**, *47*, 7009.

(204) Tye, J. W.; Darensbourg, M. Y.; Hall, M. B. *Inorg. Chem.* **2006**, *45*, 1552-1559.

(205) Justice, A. K.; Nilges, M. J.; Rauchfuss, T. B.; Wilson, S. R.; Gioia, L. D.; Zampella, G. *J. Am. Chem. Soc.* **2008**, *130*, 5293-5301.

(206) Vlugt, J. I. v. d.; Rauchfuss, T. B.; Whaley, C. M.; Wilson, S. R. *J. Am. Chem. Soc.* **2005**, *127*, 16012-16013.

(207) Olsen, M. T.; Bruschi, M.; Gioia, L. D.; Rauchfuss, T. B.; Wilson, S. R. *J. Am. Chem. Soc.* **2008**, *130*, 12021–12030.

(208) Justice, A. K.; Rauchfuss, T. B.; Wilson, S. R. *Angew. Chem. Int. Ed.* **2007**, *46*, 6152 –6154.

(209) Chong, D.; Georgakaki, I. P.; Mejia-Rodriguez, R.; Sanabria-Chinchilla, J.; Soriaga, M. P.; Darensbourg, M. Y. *Dalton Trans.* **2003**, 4158-4163.

(210) Boyke, C. A.; Vlugt, J. I. v. d.; Rauchfuss, T. B.; Wilson, S. R.; Zampella, G.; Gioia, L. D. *J. Am. Chem. Soc.* **2005**, *127*, 11010-11018.

(211) Capon, J.-F.; Ezzaher, S.; Gloaguen, F.; Francois Y. Petillon; Schollhammer, P.; Talarmin, J. *Chem. Euro. J.* **2008**, *14*, 1954-1964.

(212) Ezzaher, S.; Capon, J.-F.; Gloaguen, F. d. r.; Pe´tillon, F. Y.; Schollhammer, P.; Talarmin, J. *Inorg. Chem.* **2007**, *46*, 9863-9872.

(213) Song, L.-C.; Wang, L.-X.; Yin, B.-S.; Li, Y.-L.; Zhang, X.-G.; Zhang, Y.-W.; Luo, X.; Hu, Q.-M. *Eur. J. Inorg. Chem.* **2008**, 291-297.

(214) Cheah, M. H.; Borg, S. J.; Bondin, M. I.; Best, S. P. *Inorg. Chem.* **2004**, *43*, 5635-5644.

(215) Cheah, M. H.; Borg, S. J.; Best, S. P. *Inorg. Chem.* **2007**, *46*, 1741-1750.

(216) Borg, S. J.; Behrsing, T.; Best, S. P.; Razavet, M.; Liu, X.; Pickett, C. J. *J. Am. Chem. Soc.* **2004**, *126*, 16988-16999.

(217) Song, L.-C.; Wang, H.-T.; Ge, J.-H.; Mei, S.-Z.; Gao, J.; Wang, L.-X.; Gai, B.; Zhao, L.-Q.; Yan, J.; Wang, Y.-Z. *Organometallics* **2008**, *27*, 1409-1416.

(218) Thomas, C. M.; Darensbourg, M. Y.; Hall, M. B. *J. Inorg. Biochem.* **2007**, *101*, 1752-1757.

(219) Greco, C.; Zampella, G.; Bertini, L.; Bruschi, M.; Fantucci, P.; Gioia, L. D. *Inorg. Chem.* **2007**, *46*, 108-116.

(220) Zhou, T.; Mo, Y.; Zhou, Z.; Tsai, K. *Inorg. Chem.* **2005**, *44*, 4941-4946.

(221) Cao, Z.; Hall, M. B. *J. Am. Chem. Soc.* **2001**, *123*, 3734-3742.

(222) Fan, H.-J.; Hall, M. B. *J. Am. Chem. Soc.* **2001**, *123*, 3828-3829.

(223) Zampella, G.; Greco, C.; Fantucci, P.; Gioia, L. D. *Inorg. Chem.* **2006**, *45*, 4109-4118.

(224) Liu, Z.-P.; Hu, P. *J. Am. Chem. Soc.* **2002**, *124*, 5175-5182.

(225) Tao, J.; Perdew, J. P.; Staroverov, V. N.; Scuseria, G. E. *Phys. Rev. Lett.* **2003**, *91*, 146401.

(226) Bergner, A.; Dolg, M.; Kuumlchle, W.; Stoll, H.; Preuszlig, H. *Mol. Phys.* **1993**, *80*, 1431.

(227) Wadt, W. R.; Hay, P. J. *J. Chem. Phys.* **1985**, *82*, 284.

VITA

Panida Surawatanawong
Email:panidasu@mail.chem.tamu.edu
Work: (979) 845-7222
Mobile: (979) 846-3495

Department of Chemistry
Texas A&M University
P.O. Box 30012
College Station, TX 77842-3012

EDUCATION

Ph.D. / Chemistry Texas A&M University, College Station, TX, May 2009. Dissertation: Theoretical studies of structures and mechanisms in organometallic and bioinorganic chemistry: Heck reaction with palladium phosphines, active sites of superoxide reductase and cytochrome P450 monooxygenase, and tetrairon hexathiolate hydrogenase model. (Advisor: Prof. Michael B. Hall)

B.S. / Chemistry with first-class honors Mahidol University, Bangkok, Thailand, May 2004. (Advisor: Prof. Yuthana Tantirungrotechai)

HIGHLIGHTS

- Five years of research experience in theoretical investigations of electronic structures and reaction mechanisms for transition metal complexes
- Five years experience in Gaussian and Cerius^2 for quantum mechanical calculation
- Knowledge in Unix/Linux and programming languages (FORTRAN and C)
- Strong communication skill

RESEARCH EXPERIENCE

2009-Present	Postdoctoral Research Associate, Department of Chemistry, Texas A&M University, College Station, Texas
2004–2008	Graduate Research Assistant, Department of Chemistry, Texas A&M University, College Station, Texas (Advisor: Prof. Michael B. Hall)
2003–2004	Undergraduate Research Assistant, Department of Chemistry, Mahidol University, Bangkok, Thailand (Advisor: Prof. Yuthana Tantirungrotechai)

TEACHING EXPERIENCE

2006-2008	Graduate Teaching Assistant for Structural Inorganic Chemistry
2005	Graduate Teaching Assistant for General Chemistry Laboratory

HONORS AND AWARDS

1997 – 2008	Development and Promotion of Science and Technology Project (DPST) Scholarship, Thailand